



Fragmentation from inertial detachment of a sessile droplet: implications for pathogen transport

N. Shen¹, Y. Kulkarni², T. Jamin¹, S. Popinet², S. Zaleski^{2,3} and L. Bourouiba^{1,†}

¹The Fluid Dynamics of Disease Transmission Laboratory, Massachusetts Institute of Technology, Cambridge, MA 02139, USA

²Sorbonne Université and CNRS UMR 7190, Institut Jean le Rond d'Alembert, 75005 Paris, France

³Institut Universitaire de France, 75231 Paris, France

(Received 30 December 2023; revised 15 July 2024; accepted 12 August 2024)

Fragmentation of a fluid body into droplets underlies many contamination and disease transmission processes where pathogens are transported in a liquid phase. An important class of such processes involves formation of a fluid ligament and its destabilization into droplets. Inertial detachment (Gilet & Bourouiba, *J. R. Soc. Interface*, vol. 12, 2015, 20141092) is one of these modes: upon impact on a sufficiently compliant substrate, the substrate's motion can transfer its impulse to a contaminated sessile drop residing on it. The fragmentation of the sessile drop is efficient at producing contaminated ejected droplets with little dilution. Inertial detachment, particularly from substrates of intermediate wetting, is also interesting as a fundamental fragmentation process on its own merit, involving the asymmetric stretching of the sessile drop under impulsive axial forcing with one-sided pinning due to the substrate's intermediate wetting. Our experiments show that the radius, R_{tip} , of the tip drop ejected become insensitive to the Bond number value for $Bo > 1$. Here, Bo quantifies the inertial effects via the relative axial impulsive acceleration compared with capillarity. The time, t_{tip} , of tip-drop breakup is also insensitive to Bo . Combining experiments, theory and validated numerics, we decipher the selection of R_{tip} and its sensitivity to the surface-wetting and substrate foot dynamics. Using asymptotic theory in the large Bo limit for which the thin-film/slender-jet approximations hold, we derive a reduced physical model that predicts R_{tip} consistent with our experiments. Finally, we discuss how pathogen physical properties (e.g. wetting and buoyancy) within the sessile drop determine their distribution in the tip and secondary fragmentation droplets.

Key words: aerosols/atomization, multiphase and particle-laden flows, interfacial flows (free surface)

† Email address for correspondence: lbouro@mit.edu

1. Introduction

Various modes of fluid fragmentation inherent to foliar disease transmission have been linked to the average wetting dominating most crop leaves (Gilet & Bourouiba 2014, 2015, 2017). One such mode is the inertial detachment: upon impact from rain, irrigation or dew drops, the motion of a compliant leaf locally transfers its impulse to a sessile contaminated drop residing on it. The contaminated drop forms a ligament that detaches from the leaf, ejecting secondary droplets through end-pinching. Such resulting fragmentation of the sessile contaminated drop is particularly interesting in this application domain for its ability to produce highly contaminated ejected droplets that do not undergo any dilution and typically produce a distinct primary tip drop. Indeed, little to no mixing between the impacting and the contaminated drop occurs from this process. Figure 1, adapted from Gilet & Bourouiba (2015), shows an image sequence of drop inertial detachment driven by the flexural motion of a compliant leaf, upon raindrop-like impact.

Fragmentation from liquid column disintegration is also relevant for a wide range of engineering, physical and biological systems and applications involving impacts of drops on surfaces or films/pools, with end-pinching of ligaments, or their merger shaping, in part or fully, the distribution of ejected droplets of varying sizes and speeds (Qian & Law 1997; Villermaux & Bossa 2011; Wang & Bourouiba 2018, 2021; Lejeune, Gilet & Bourouiba 2018). Such applications include spray coating, agricultural irrigation, fuel combustion (Yarin 2006; Villermaux 2007), microfluidic and electronic systems (Sarobol *et al.* 2016), functional materials printing (Derby 2010), bioinks for 3D printing (Gopinathan & Noh 2018) and more generally disease transmission, from mucosalivary fluid fragmentation relevant for respiratory disease transmission to bursting bubbles for waterborne pathogens in addition to the fragmentation of sessile pathogen-laden drops on leaves relevant for foliar disease transmission between plants outlined above (Poulain & Bourouiba 2018, 2019; Bourouiba 2021a,b).

Inertial detachment is also interesting as a fundamental fragmentation process on its own merit, as the asymmetric stretching under impulsive axial forcing shapes the fragmentation of the initially sessile drop. It is well known that elongated and slender liquid ligaments undergo fragmentation due to surface-tension-induced instability. The normal mode related growth of interface perturbation is typically attributed to a Rayleigh–Plateau (R–P) type instability (Plateau 1873; Rayleigh 1878; Eggers 1993, 1995). The R–P instability assumes an infinitely long cylindrical fluid column. On the other hand, Stone, Bentley & Leal (1986) and Stone & Leal (1989) showed that end-pinching prior to the manifestation of the R–P instability can be the driver of fragmentation for contracting viscous filaments of finite length. Such unsteady, non-modal fragmentation motivated experimental and numerical studies on recoiling filaments and end-pinching of symmetrical ligament breakup (Schulkes 1996; Notz & Basaran 2004; Castrejón-Pita, Castrejón-Pita & Hutchings 2012). Moreover, the effect of axial stretching on the stability of an inertial jet was also first discussed analytically by Frankel & Weihs (1985), and later extended by Henderson *et al.* (2000). The breakup of liquid bridges formed in extensional flows was also further investigated (Slobozhanin & Perales 1993; Gaudet, McKinley & Stone 1996; Marmottant & Villermaux 2004; Vincent, Duchemin & Villermaux 2014). These studies established that the strength of inertial acceleration, e.g. gravity, relative to surface tension, as measured by the Bond number, Bo , and the liquid–solid contact dynamics determine the stability regimes of an inviscid bridge. However, the findings of this large body of work is not directly applicable to the end-pinching of elongated drops we are concerned about herein, where the asymmetry of the stretching imposed by axial

Fragmentation from inertial detachment of a sessile droplet

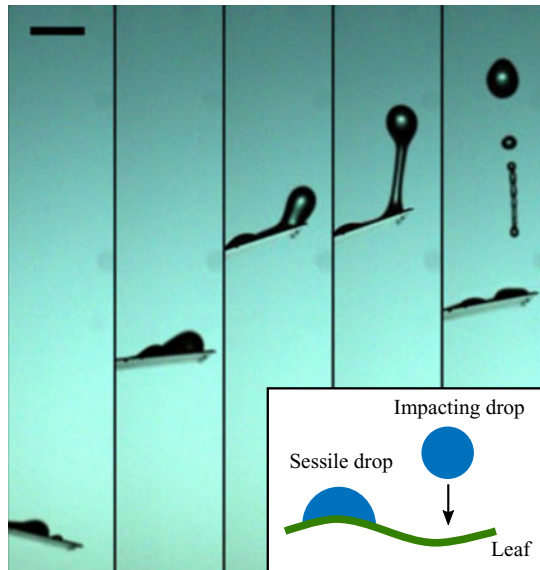


Figure 1. Inertial detachment from a compliant leaf induced by raindrop impact. Images recorded 62.5 to 122.5 ms after drop impact. A scale bar of 5 mm is given. Here, the associated Bond number according to (2.8a,b) is estimated as $Bo \approx 8$. The inset shows a schematic. Images adapted with permission from Gilet & Bourouiba (2015).

forcing and contact dynamics at the fluid–structure interface are major distinctions from prior work on ligament breakup.

End pinching was also treated in detail for pendant drops, for example via equilibrium analysis (e.g. Padday, Pitt & Tabor 1973; Boucher & Kent 1978). Although unsteady evolution of pendent drops was captured subsequently (e.g. via high-speed imaging, Peregrine, Shoker & Symon 1990) catalysing numerous non-equilibrium theoretical and numerical investigations (e.g. Eggers & Dupont 1994; Schulkes 1994; Brenner *et al.* 1997; Wilkes, Phillips & Basaran 1999; Ambravaneswaran, Wilkes & Basaran 2002), dripping flows exiting nozzles remained generally the focus of these studies. Such flows differ from the end-pinching from inertial detachment of a sessile drop we are concerned about here where contact-line wetting and limited mass constraint are essential ingredients of the fragmentation and secondary ejected daughter drop formation.

In this article, we address the following questions:

- (i) When does a sessile drop first detach/fragment from its supporting substrate under inertial forcing? And after fragmentation, what is the amount of the liquid content released?
- (ii) What are the roles of the imposed inertial force, surface tension and surface wetting in the selection of the fragments? And as the drop deforms, what are the dominant physical mechanisms that cause primary fragmentation?
- (iii) How do these mechanisms determine the detachment time and the size of primary daughter fragment/droplet release?
- (iv) What is the role of the solid–liquid contact line in shaping the fragmentation of the primary drop?
- (v) Finally, returning to our original application of interest, and having validated our modelling of the inertial detachment end-pinching against experiments, what can we learn about the distribution of organisms of various wetting properties (e.g.

hydrophobic spores vs wetting neutrally buoyant bacteria) in the primary ejected drop vs secondary droplets?

To address these questions, we combine experimental and theoretical approaches also with direct numerical simulations (DNS) of the liquid–gas two-phase Navier–Stokes equations incorporating two different dynamic models for the liquid–solid contact. We begin in § 2 with a reduced experimental set-up that mimics the drop detachment flow observed on plant leaves. This involves first depositing a sessile drop on stationary plate substrates of different affinities for water, and then impulsively imposing a constant acceleration to the plate–drop system in the direction of gravity, while monitoring the consequent drop deformation and fragmentation and controlling for lateral vibration.

In response to (i) we find that the original sessile drop elongates into a ligament and subsequently breaks under inertial acceleration; surprisingly, however, the breakup time and size of the first ejected drop at the ligament tip become insensitive to both the Bond number and the equilibrium liquid–solid contact angle as the Bond number increases. In response to (ii) and (iii) using the DNS (introduced in § 2.3), we examine the role of capillarity and inertia in isolation, revealing the dominant factors that control the chain of fragmentation (§ 3). We develop asymptotic theories in the large Bond number limit (§ 3), leveraging the extreme aspect ratios of the drop/ligament during different stages of the deformation, i.e. thin film vs slender jet. In particular, we capture the effect of surface tension via geometrical arguments and propose a ‘lollipop’ structure for the ligament at its pinch-off time. The ‘lollipop’ reduced theoretical model captures the experimental and DNS results well. In response to (iii) and (iv), we identify (§ 3.5) that the error in prediction on the primary drop size and breakup time is caused by the contact dynamics, which has weak, but lasting effects on the end-pinching dynamics. Moreover, correction to the leading-order theory can be achieved by modifying the simple contact model used in the DNS and asymptotic theory. Having validated the numerical and theoretical model against experiments, in response to (v) (§ 4) we examine how reduced analogue pathogens/contaminants of different wetting properties distribute in the fragments, i.e. primary drop and satellite droplets. We conclude in § 5.

2. Inertial detachment analogue experiments and physical picture

In its original discovery by Gilet & Bourouiba (2014, 2015, 2017), inertial detachment fragmentation (e.g. figure 1) was associated with average wetting surfaces leading to retention of drops on the surface via hysteresis. The initially sessile drops were observed to be accelerated via the impact of other drops (e.g. rain or dew), imparting inertia to the leaf that, in turn, accelerates the sessile drops. To simplify the study of this fragmentation process, we adopt an analogue experimental set-up with a sessile drop on a plate (figure 2) and imparting axial extension in the same direction as gravity. Our simplification enables us to derive insights into the fundamental mechanisms driving this fragmentation process. We first introduce the details of that experimental analogue system, and then discuss the key results of the inertial detachment.

2.1. Experimental method

The experimental set-up is shown schematically in figure 2(a) where a sessile water drop of volume V is deposited on a locked, stationary horizontal plate. From below, the substrate is attached to a spring system in extension. At time $t = 0^+$, the spring is released, imposing a normal (downward) acceleration a on the plate. The acceleration a is

Fragmentation from inertial detachment of a sessile droplet

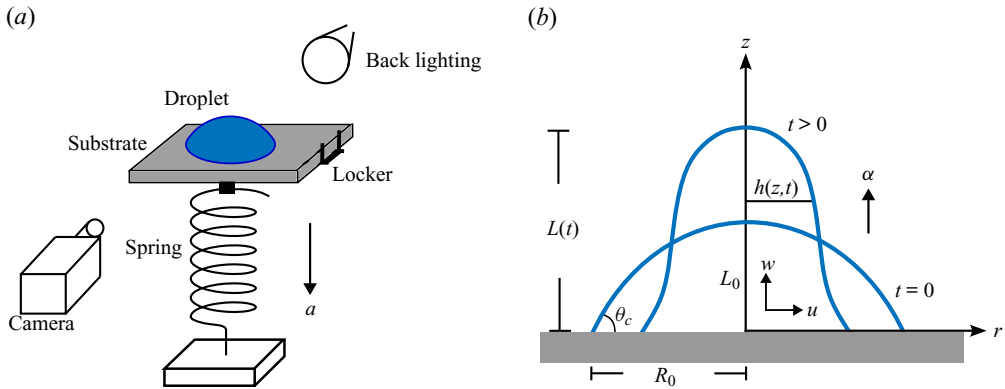


Figure 2. (a) Experimental schematic. The substrate is impulsively accelerated at $t = 0^+$ by the spring at constant accelerating a in the same direction as gravity. (b) Axisymmetric drop geometry under two-dimensional (2-D) cylindrical coordinate system. Here, u, w are the flow velocity components in the plate-stationary frame; α is the magnitude of inertial acceleration.

Substrate	θ_c	a	V	Bo	Re	Oh
PMMA	$60^\circ \pm 5\%$	$29\text{--}107 \text{ m s}^{-2}$	$4\text{--}200 \mu\text{l}$	1–11	300–1500	0.002–0.004
Microslide	$19^\circ \pm 5\%$	$72\text{--}119 \text{ m s}^{-2}$	$10\text{--}100 \mu\text{l}$	1.5–12	300–1500	0.002–0.004

Table 1. Experimental parameters. Here, θ_c is drop equilibrium contact angle, a is the plate acceleration, V is the drop initial volume (in microlitres) with measurement error of 1%–5% for the pipettes and volumes used, Bo and Re are, respectively, the inertial Bond and the Reynolds numbers defined in (2.8a,b) and $Oh = \sqrt{Bo}/Re$ is the Ohnesorge number. Given the large values of Re (and small values of Oh), viscous effects are negligible.

maintained close to constant in each experiment with a sufficiently long extension of the spring. Its value is calculated and monitored for each experiment through image processing of the high-speed recordings. The impulsive translation motion of the substrate results in unsteady, axisymmetric deformation of the drop that is also recorded via high-speed imaging in side view at 2000 frames per second. The distance between the fixed camera and the moving drop is $O(100)$ larger than the drop's observed vertical displacement, ensuring negligible perspective distortion in imaging.

Focusing on the intermediate wetting conditions described in Gilet & Bourouiba (2015), this study uses polymethyl methacrylate (PMMA) as a substrate as it is comparatively hydrophobic. As a comparison and for reference we also add double-frosted microscope slides (microslides) that are comparatively more hydrophilic. The static contact angle between the drop and substrate given by PMMA and microslides are $\theta_c = 60^\circ$ and $\theta_c = 19^\circ$, respectively (illustrated in figure 2b at $t = 0$). For each substrate, a series of experiments is conducted with varying plate acceleration a and sessile drop volume V in ranges listed in table 1. Standard properties of water under room temperature and atmospheric pressure are taken for density ρ , surface tension σ and dynamic viscosity μ .

2.2. Physical picture and non-dimensional characterization

Given the axisymmetric nature of the inertial detachment about the vertical axis parallel to the acceleration, we consider a two-dimensional cylindrical coordinate system of unit

vectors \hat{r} and \hat{z} co-moving with the substrate. The origin is taken to be at the centre of the sessile drop–substrate contact circle, as shown in [figure 2\(b\)](#).

2.2.1. Initial shape of the sessile drop

By choosing the length scale

$$R_{eq} = \left(\frac{3V}{4\pi} \right)^{1/3}, \quad (2.1)$$

that gives the radius of an equivalent sphere of the same volume V , the initial shape of the drop can be characterized by the dimensionless Young–Laplace equation (Lubarda & Talke 2011)

$$\frac{1}{h_0(1+h_0'^2)^{1/2}} - \frac{h_0''}{(1+h_0'^2)^{3/2}} = -2h_0''(L_0) + G(L_0 - z), \quad (2.2)$$

where $h_0(z) \equiv h(z, t = 0^-)$ is the initial profile of the drop radius, h_0' and h_0'' are its first and second derivatives with respect to z , L_0 is the initial height with $h_0(L_0) = 0$ and

$$G = \frac{\rho g R_{eq}^2}{\sigma} \quad (2.3)$$

is the Bond number based on gravitational acceleration g . The associated boundary condition

$$h_0'(0) = -\cot \theta_c, \quad (2.4)$$

involves the equilibrium contact angle θ_c that is a property of the substrate ([table 1](#)). Note that, in the $G \rightarrow 0$ limit, solution to (2.2) for $h_0(z)$ yields a spherical cap, as expected.

2.2.2. Drop evolution upon substrate acceleration

For $t > 0$, in the plate's reference frame, the drop is subject to both gravity and an inertial force due to the plate's acceleration, giving a net body force $\rho\alpha\hat{z}$ where

$$\alpha = a - g, \quad (2.5)$$

is the effective acceleration. We subsequently default to the inertial velocity and time references

$$U_\alpha = \sqrt{\alpha R_{eq}}, \quad T_\alpha = \sqrt{\frac{R_{eq}}{\alpha}}, \quad (2.6a,b)$$

so the drop's flow through quiescent ambient air of negligible density and viscosity is governed by the non-dimensional Navier–Stokes equations, with pressure non-dimensionalized by σ/R_{eq} , the capillary pressure

$$\begin{cases} \nabla \cdot \mathbf{u} = 0, & (2.7a) \\ \frac{\partial \mathbf{u}}{\partial t} + \mathbf{u} \cdot \nabla \mathbf{u} = -\frac{1}{Bo} (\nabla p - \kappa \hat{n} \delta_s) + \frac{1}{Re} \nabla^2 \mathbf{u} + \hat{z}, & (2.7b) \end{cases}$$

where $\mathbf{u} = u\hat{r} + w\hat{z}$ is the velocity vector, p is pressure, κ is surface curvature, \hat{n} is the unit normal, δ_s is the surface Dirac δ -distribution concentrated on the interface (Popinet 2018)

and

$$Bo \equiv \frac{\rho\alpha R_{eq}^2}{\sigma} = \frac{\alpha}{g}G, \quad Re = \frac{\rho\alpha^{1/2}R_{eq}^{3/2}}{\mu}, \quad (2.8a,b)$$

are the acceleration-based Bond number and Reynolds number, respectively. It is also convenient here to define the Ohnesorge number $Oh \equiv \mu/\sqrt{\rho\sigma R_{eq}} = \sqrt{Bo}/Re$ that directly compares viscous and surface tension effects. Finally, evolution of the profile $h(z, t)$ of the drop radius follows the kinematic condition

$$\left[\frac{\partial h}{\partial t} + w \frac{\partial h}{\partial z} \right]_{r=h} = u|_{r=h}. \quad (2.9)$$

2.2.3. Characteristic scales: inertial vs capillary scales

With an appropriate model for the contact dynamics prescribed at $z = 0$ (discussed in § 2.3), we have obtained a closed description for the drop under inertial acceleration for all $t \geq 0$. This system is governed by four dimensionless parameters: the contact angle θ_c , gravitational Bond number G (or equivalently, the acceleration ratio α/g), the inertial Bond number Bo and the Reynolds number Re . Ranges of Bo used in the experiments are given in table 1, whereas typical values of Re are of $O(10^{2-4})$. Therefore, the inviscid flow assumption is reasonable, until ligament pinch-off is approached (Lister & Stone 1998). We will also focus on results obtained for small G where gravitational effects on the initial drop shape and thus early-stage motion are small.

The competition between inertial acceleration and capillarity due to surface tension is a key mechanism that drives the drop deformation, therefore it is instructive to also introduce the dimensional capillary wavelength Λ , time T_σ and velocity U_σ units

$$\Lambda = \sqrt{\frac{\sigma}{\rho\alpha}}, \quad T_\sigma = \sqrt{\frac{\rho R_{eq}^3}{\sigma}}, \quad U_\sigma = \alpha \sqrt{\frac{\rho R_{eq}^3}{\sigma}}. \quad (2.10a-c)$$

Particularly, U_σ measures the change of speed generated by the imposed acceleration α over the capillary time scale T_σ . Under the inertial references (2.1) and (2.6a,b), these become

$$\lambda \equiv \frac{\Lambda}{R_{eq}} = \frac{1}{\sqrt{Bo}}, \quad t_\sigma \equiv \frac{T_\sigma}{T_\alpha} = \sqrt{Bo}, \quad u_\sigma \equiv \frac{U_\sigma}{U_\alpha} = \sqrt{Bo}. \quad (2.11a-c)$$

We henceforth denote $\tau = t/\sqrt{Bo}$ for rescaled physical dimensional time in capillary units, while t is our default time non-dimensionalized by the inertial time scale T_α from (2.6a,b).

2.3. Methods for direct numerical simulations

2.3.1. Numerical framework and additional non-dimensional parameters

According to the framework given in § 2.2, the drop detachment experiments are also simulated numerically to further our understanding of the fragmentation mechanism that is critical for disease transmission applications. The key numerical methods are explained next.

We adopt *Basilisk* (Popinet 2009, 2015, 2018) and solve the axisymmetric incompressible two-phase Navier–Stokes equations with surface tension for the air–liquid system. Simulations of high density ratios like air–water and non-negligible inertia are

numerically challenging, hence we employ the momentum-conserving volume-of-fluid (VoF) scheme (Arrufat *et al.* 2021). This is particularly necessary for high Bo . Therein, the equations of motion for air, a counterpart of (2.7), are coupled and introduce ratios for density and dynamic viscosity: ρ_a/ρ and μ_a/μ , between air (subscript a) and water. These add to existing list of control parameters of the numerical system: θ_c , Bo , G and Oh .

2.3.2. Numerical model with constant contact-angle model

One challenge on the numerical modelling is the appropriate capture of the liquid–solid contact line dynamics. This turns out to be important, as discussed hereafter, to capture the tip and foot breakups. We start with a no-slip boundary condition at the wall along with a constant grid-scale contact angle as a first-order approximation. We subsequently develop a different numerical model in Appendix G where the constant angle approximation is relaxed. Unless otherwise stated, DNS results presented in the rest of this manuscript are obtained using the constant contact-angle model.

Regarding the first no-slip model, it has a force singularity at the contact line (Huh & Scriven 1971), which is handled in the VoF formulation using an implicit numerical slip (Afkhami, Zaleski & Bussmann 2009). Specifically, we consider the standard water and air conditions, and simulate sessile drops of fixed initial volume $56.5 \mu\text{l}$ and therefore constant $G = 0.755$ and $Oh = 2.18 \times 10^{-3}$ (comparable to the experimental values reported in table 1). The value of Bo is subsequently varied by changing α/g . The case corresponding to $\theta_c = 60^\circ$ is extensively studied. The range of Bo in simulation is varied from 1.5 to 12. For $\theta_c = 60^\circ$, below the value of $Bo = 1.5$, fragmentation is suppressed.

2.4. Elongation and fragmentation of the sessile drop

2.4.1. The unstable breakup regime

Upon plate release, the initial sessile drop elongates vertically forming a ligament while its foot remains in contact with the substrate. For sufficiently large drop volume V and effective acceleration α , necking occurs near the ligament tip as well as its foot, which ultimately leads to breakup and partial ejection of the sessile drop volume. A typical sequence of drop deformation is shown in figure 3(a i–a v), where (a i) gives the initial shape; (a ii) shows ligament formation; (a iii) and (a iv) respectively depict tip and foot pinch-off when the ligament breaks, ejecting secondary drops/ligaments from the original sessile drop; and finally (a v) illustrates that, after the foot pinch-off, the detached ligament further fragments into multiple satellite droplets. We will show in Appendix A that the order of tip and foot breakup depends on the Bond number Bo .

As aforementioned, unstable inertial detachment of the drop (figure 3a) occurs only if Bo exceeds a critical value with a very weak dependence of this value on the substrate equilibrium contact angle θ_c . The analogous stability analysis for a pendant drop was performed by Boucher *et al.* (1976), and the corresponding stability diagram, adapted to our (Bo, θ_c) phase space, is shown in figure 3(b). Here, the ‘stable’ region according to Boucher *et al.* (1976) was determined by quasi-static increase of the volume of a pendent drop until its detachment from a substrate of a given wetting, showing again the very weak dependence on contact angle. We highlight the (Bo, θ_c) parameters that yield detachment in our experiments in figure 3(b). The critical Bo required for our sessile drops to become unstable matches well with the analysis of Boucher *et al.* (1976).

Fragmentation from inertial detachment of a sessile droplet

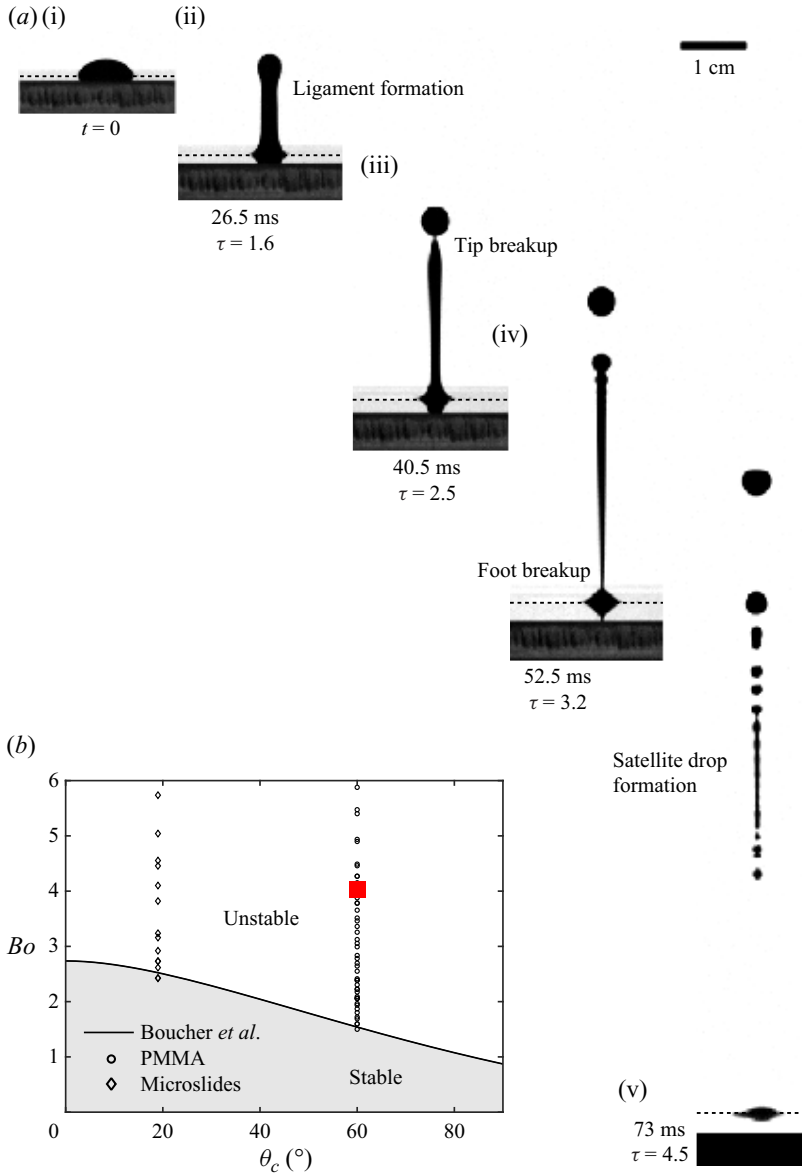


Figure 3. (a) Successive temporal sequence of a drop undergoing inertial detachment and fragmentation. Experiment conducted with a PMMA substrate ($\theta_c = 60^\circ$), and with acceleration ratio $\alpha/g = 4.2$ and drop initial volume $V = 80 \mu\text{l}$. A dashed line is drawn for each frame to separate the drop and its optical reflection on the substrate. A scale bar is given in (a v). (b) Stability diagram in (Bo, θ_c) -space that distinguishes unstable drops that partially detach from the substrate. The equilibrium theory of Boucher, Evans & Kent (1976) for pendant drops is compared with our experiments where only unstable cases are plotted. The red square corresponds to the example sequence given in (a) where $\theta_c = 60^\circ$, $Bo = 4$.

2.4.2. Evolution simulation

Analogous to the image sequence shown in figure 3(a), the simulated evolution of the drop for $Bo = 4$ at various stages is shown in figure 4. Following the constant angle model discussed in § 2.3.2, we capture the experimental features well: tip pinch-off,

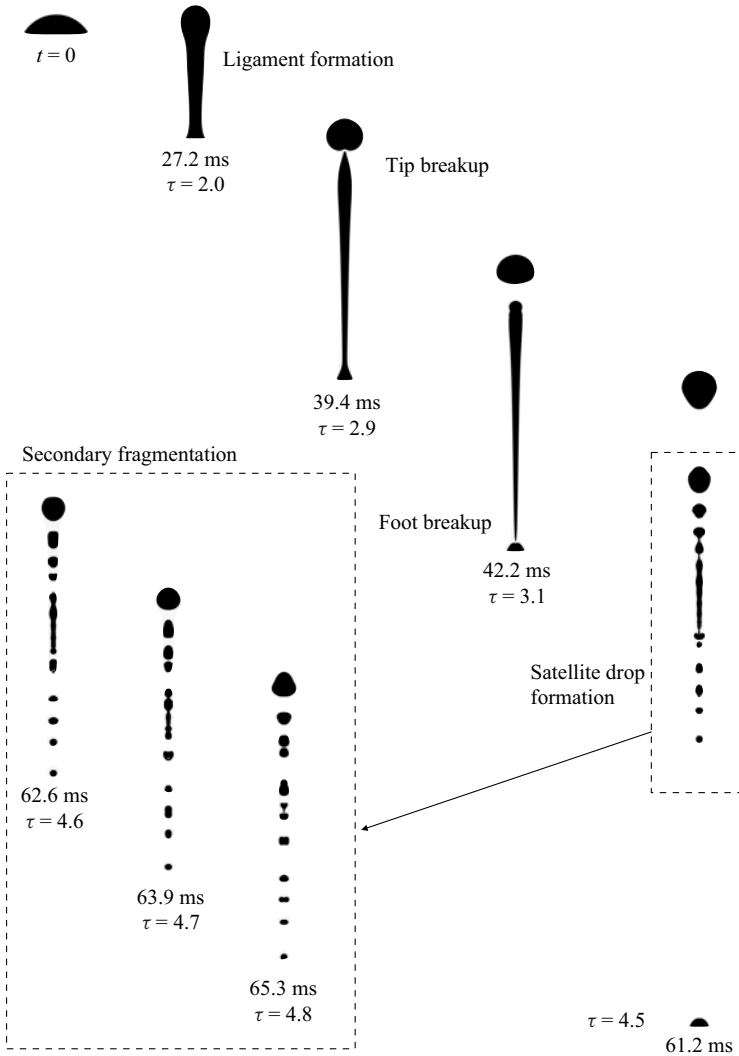


Figure 4. Direct numerical simulation rendering of evolution of the drop for $Bo = 4.0$ and $\theta_c = 60^\circ$. The numerical values indicate time with capillary time unit $T_\sigma = 13.6$ ms (see (2.10a-c)). A total time span up to 61.2 ms is shown, roughly covering the same range as the experimental results of figure 3 and hence depicting tip pinch-off, foot pinch-off and formation of satellite drops from secondary fragmentation. The axis ratio in each image is unity and the scale is the same for all images.

foot pinch-off, secondary fragmentation of the elongated middle fluid mass. Zooming in on the secondary fragmentation of the elongated structure reveals that the numerics do capture secondary daughter droplet formation as well. We further discuss the evaluation of convergence for the tip pinch-off time and volume of the ejected primary tip daughter droplet in Appendix E.

2.4.3. Primary drop (tip) ejection

We focus primarily here on ejection of a tip drop from the ligament tip undergoing inertial acceleration, as shown in figure 3(a iii-a v). We characterize the tip drop with its equivalent radius, $R_{tip} = [3V_{tip}/(4\pi)]^{1/3}$, where V_{tip} is the ejected volume and the time

Fragmentation from inertial detachment of a sessile droplet

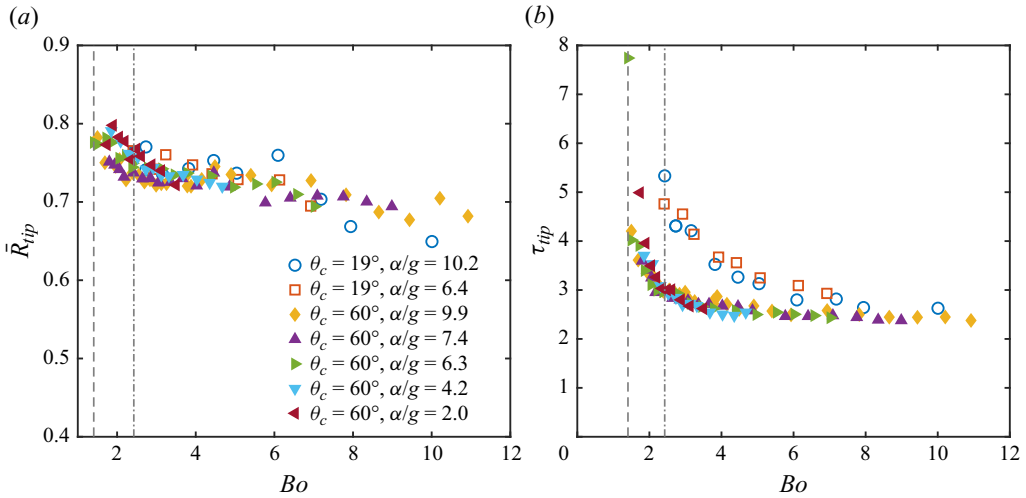


Figure 5. (a) Dimensionless radius \bar{R}_{tip} of ejected tip drop as a function of Bond number Bo , contact angle θ_c and acceleration ratio α/g . The dashed lines label the critical Bo over which detachment occurs for the two given θ_c . (b) The corresponding tip breakup time τ_{tip} is non-dimensionalized using the capillary time scale. Both \bar{R}_{tip} and τ_{tip} converge rapidly to a constant as Bo increases for all parameters used, suggesting a universal end-pinching process controlled by capillary effects and negligible contact-line dynamics effects on the tip dynamics. Note that in (b) at $Bo = 2.7$ two open circles overlap, within measurement error (see table 1).

of its neck pinch-off, τ_{tip} , namely its tip breaking time, is non-dimensionalized using the capillary time scale. Figure 5(a,b) shows first that both R_{tip} and τ_{tip} converge rapidly to values independent of Bo with sufficiently high Bo , and also close to independent from θ_c and acceleration ratio α/g . Second, the figures show that the dependence of R_{tip} and τ_{tip} on Bo collapse on a master curve for different α/g (or equivalently gravitational Bond number G).

More specifically, as Bo increases, the dimensionless $\bar{R}_{tip} = R_{tip}/R_{eq}$ rapidly approaches $R_{tip} \approx 0.7$ (with the over-bar henceforth dropped) for our range of α/g and θ_c values explored herein. Further, in figure 5(b) τ_{tip} is also nearly independent of Bo as it converges to $\tau_{tip} \approx 2.5$. Note that it does so less rapidly with Bo than R_{tip} . Indeed, contrary to R_{tip} , where substrate effects are negligible, τ_{tip} converges to $\tau_{tip} \approx 2.5$ slightly slower for smaller θ_c than it does for larger θ_c . This suggests that the substrate local contact-line dynamics can affect both ends of the breakup, not just the foot pinch-off. However, this local contact dynamics effect is rapidly negligible as Bo increases, as R_{tip} and τ_{tip} become blind to substrate local wetting.

Given the inviscid nature of this system, the tip detachment mode is closely related to end-pinching, which can occur for long ligaments as well as unsteady short protuberances (Stone 1994; Wang & Bourouiba 2021). It was observed both in multiple systems, for example in numerical studies of contracting liquid filaments (Schulkes 1996), and experimental studies of unsteady short rim emerging ligaments (Wang & Bourouiba 2021) that end-pinching releases a tip drop of radius proportional to the average radius of the filament, in fixed capillary time units. We further discuss the end-pinching dynamics in § 3.2.

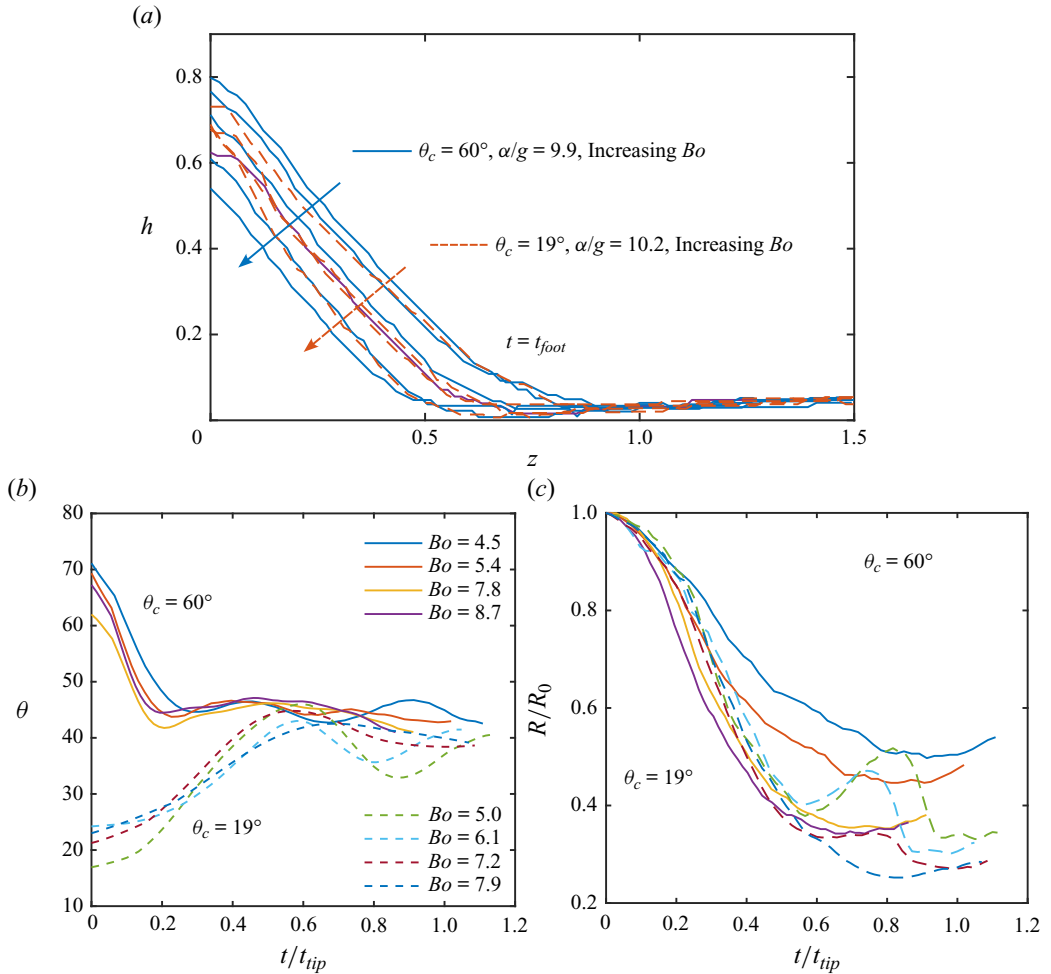


Figure 6. (a) Drop foot profiles, $h(z)$, at foot breakup times $t = t_{foot}$ experimentally measured on the substrates of distinct wetting. Results from $Bo = 4.2, 4.5, 5.4, 6.9, 7.8, 9.4$ are shown for $\theta_c = 60^\circ$ (solid), and $Bo = 5, 6, 7.9, 10$ for $\theta_c = 19^\circ$ (dashed). (b) Temporal evolution of the foot angle, $\theta(t)$, approximated by a fitted cone located in the range $0 \leq z \leq 0.2$ as shown in (a) for $0 \leq t/t_{tip} \leq t_{foot}/t_{tip}$. Clearly, θ from different Bo and θ_c converge to a common mean receding angle value around 40° rapidly before tip breakup. This value is, at first order, independent of the initial static contact angle. (c) Evolution of the normalized contact radius $R(t)/R_0$ that corresponds to the same drops measured in (b). It shows that, for the more wetting surface, i.e. smaller initial static contact angle, the Bond number has little effect on the evolution of the contact line. In other words, the de-pinning dynamics is more independent of Bo than for the less wetting surface.

2.4.4. Evolving contact angle and de-pinning

The apparent contact angle formed between the ligament foot and the substrate does not maintain its constant equilibrium value over time as elongation occurs. Figure 6 shows this variation in contact angle over time: figure 6(a) first shows two series of ligament diameter profiles at foot breakup time $t = t_{foot}$ but different initial static contact angles $\theta_c = 60^\circ$ and 19° , and for a range of Bo . The two series converge to a conical shape of comparable final receding angles at the substrate. To characterize these conical feet, we estimate a dynamic contact angle at the foot $\theta(t)$, obtained from $h(z, t)$ measurements in the range $z \in [0, 0.2]$ for each t up to $t = t_{foot}$. This yields again two time series of $\theta(t)$

plotted in figure 6(b) for the two different initial θ_c . We clearly see that both series for the estimated θ approach a mean value $\bar{\theta}$ around 40° as $t \rightarrow t_{tip}$ rather quickly, before tip pinch-off occurs, which occurs, roughly, around $t \approx 0.2t_{tip}$ for $\theta_c = 60^\circ$ and $t \approx 0.4t_{tip}$ for $\theta_c = 19^\circ$. We show in Appendix C that a constant foot angle is indeed expected if the flow is dominated by inertial acceleration. Note that we observe mild $\theta(t)$ oscillations after the convergence to the final receding angle with approximately $0.5t_{tip}$ period around the mean $\bar{\theta}$ that occurs in all experiments.

In parallel, figure 6(c) gives direct measurements of the receding contact radius $R(t)/R_0$, with $R(t) = h(0, t)$ and $R_0 = R(0)$, as a function of time. First, for both wettings, we see a decrease of $R(t)/R_0$ with a contact line at time of foot breakup, $t = t_{foot}$, reaching essentially less than half of the initial wetting extent. Second, for smaller initial static contact angle, the Bond number has little effect on the evolution of the contact line and its de-pinning. In other words the de-pinning dynamics is less dependent on Bo for more wetting substrates. In fact, for the largest Bo examined, both surfaces show close to identical and superposable receding contact radius dynamics. Note, that we see more variation of the evolution of $R(t)/R_0$ with Bo for the larger initial static contact angle, with faster de-pinning with higher Bo . Third, when the contact-angle value reaches its final receding angle, further displacement of the contact point becomes negligible. Finally, recall that fluctuations of the contact angle were seen to be more important for the more wetting surface. We also see more fluctuation of $R(t)/R_0$ for the more wetting surface. However, these fluctuations decrease in amplitude with increasing Bo .

2.4.5. Curvature change, necking onset and early-time selection of the volume of tip drop

Here, we link the tip-drop volume selection to the early dynamics of the deforming sessile drop. In fact, we find that the volume of the tip drop is essentially already determined, for the most part, at the very early stage of curvature inflection of the drop contour and preceding the development of a clear elongated ligament. As we shall show quantitatively next, in figure 7, plotting $h(z, t)$, that the tip-drop volume is already selected, to $\pm 15\%$, by the time the final receding angle of the foot, $\bar{\theta} \approx 40^\circ$, is reached at the contact line (figure 6). These times are $t/t_{tip} = 0.2$ for $\theta_c = 60^\circ$ and $t/t_{tip} = 0.4$ for $\theta_c = 19^\circ$. In fact, by these times, a sign switch of $\partial_z^2 h$ and κ along z -axis occurs, i.e. a curvature inflection of h develops. At the time of clear curvature sign change, the volume enclosed between the point of curvature inflection and the top of the deforming contour can be converted into an equivalent spherical drop radius of

$$R_{equi}(\xi, t) = \left(\frac{3 \int_{\xi}^{L(t)} h(z, t)^2 dz}{4} \right)^{1/3}, \quad (2.12)$$

where $0 \leq \xi \leq L(t)$ specifies the volume domain and $L(t)$ is the ligament height at time t . In figure 7, the locations ξ that respectively yield $R_{equi}/R_{tip} = 0.85, 1, 1.15$ are labelled for all instants. When a clear curvature inflection of the sessile drop contour appears, R_{equi} at $z = \xi$, near such an inflection point, recovers the size of the ejected tip drop, R_{tip} (shown in figure 5), within $\pm 15\%$ error of the actual *a posteriori* post-pinch-off direct R_{tip} measurement. In sum, for all Bo and wetting substrates, the convergence of the contact angle to its final value $\bar{\theta}$, at the contact line, associated with little variation of apparent contact-line radius or contact angle subsequently, also coincides with the clear appearance of a curvature inflection of the drop contour profile. Such conditions impose the geometric

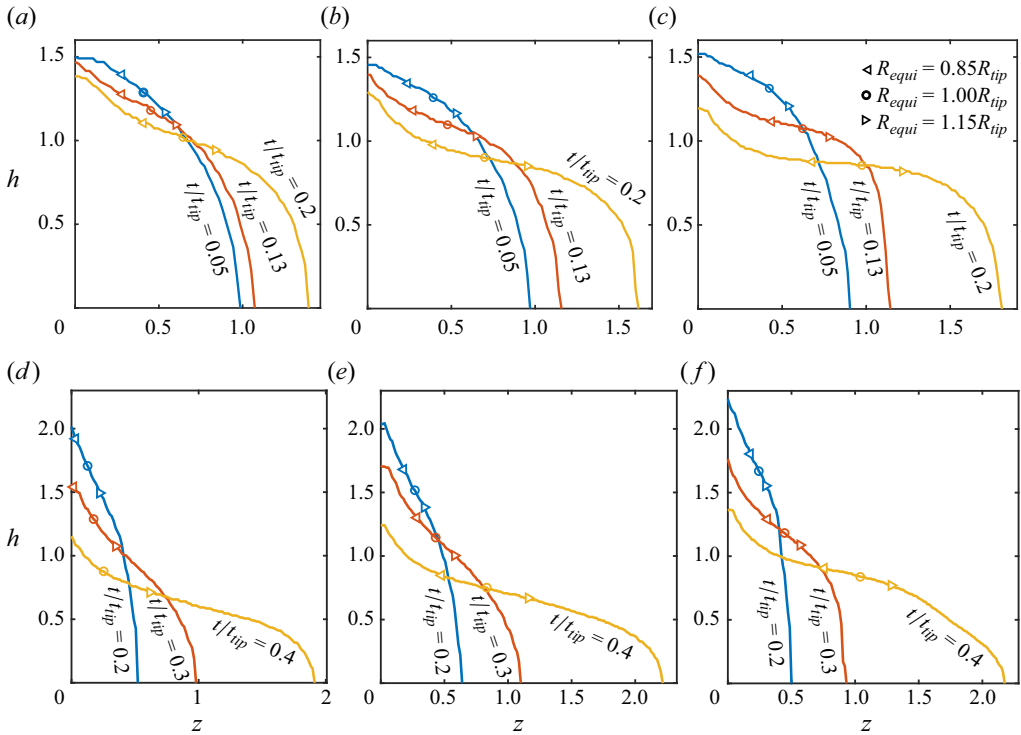


Figure 7. Evolution of the drop radius contour profile $h(z, t)$ measured for different wettings and for increasing Bo . Here, the axial z -axis of symmetry is in the horizontal direction. In (a–c), $\theta_c = 60^\circ$ and $Bo = 3.8, 5.9, 8.7$. Results are shown at three instants $t/t_{tip} = 0.05, 0.13, 0.2$ for each Bo . In (d–f), $\theta_c = 19^\circ$, $Bo = 7.2, 7.9, 10$, and for each panel $t/t_{tip} = 0.2, 0.3, 0.4$. Along each contour, the portion of the deformed drop whose volume generates an equivalent radius of $R_{equi}/R_{tip} = 0.85, 1, 1.15$ is marked by solving (2.12). We show that the first time of appearance of a clear inflection point of the curvature coincides, at first order, with the selection of the final receding contact angle at the foot (figure 6), i.e. $\approx 0.2t_{tip}$ and $\approx 0.4t_{tip}$, for $\theta_c = 60^\circ$ and $\theta_c = 19^\circ$, respectively. And that at this early time of appearance of the inflection the volume between the z -plane of this first inflection region and the tip of the deforming sessile drop, the final size of the tip drop ejected, R_{tip} , is already selected for the most part to within 15% error.

constraint that selects already, at this early time, for the most part, the tip-drop volume; that is even prior to development of a clear ligament. Moreover, we can also conclude that the end-pinch-off ultimately leading to the ejection of the primary tip drop is only weakly influenced by the substrate dynamics/wetting. In § 3 we will further examine this insight analytically and numerically.

3. Asymptotic theory: large Bond number limit

Given the robust collapse of the data regarding tip-drop size and pinch-off time for all Bond numbers ($Bo \gtrsim 4$) (recall § 2.4), in this section, we develop analytical asymptotic models in the $Bo \rightarrow \infty$ limit for different stages of the drop evolution when approximate solutions to the governing equations can be facilitated by extreme aspect ratios of the drop geometry. We validate such theoretical predictions with experiments and further compare them with numerical results, to further validate the numerical scheme against both experiments and asymptotic mathematical models.

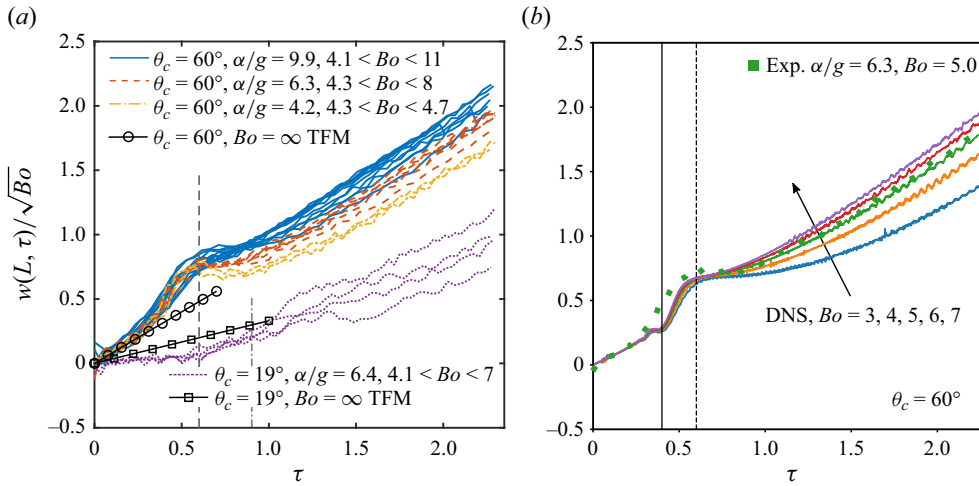


Figure 8. Drop tip velocity $w(L, \tau)$ (given in capillary units according to (2.11a–c)) as a function of capillary time τ , up to tip breaking. (a) Experimental measurements for two different θ_c , a range of α/g and Bo . Specifically, $Bo = 4.1, 4.5, 4.9, 5.4, 5.9, 6.9, 7.8, 8.7, 9.4, 10.2, 11$ for $\alpha/g = 9.9$; $Bo = 4.4, 5.0, 5.5, 6, 6.6, 7$ for $\alpha/g = 6.3$; $Bo = 4.4, 4.7$ for $\alpha/g = 4.2$; and $Bo = 4.4, 5.1, 6.1, 6.9$ for $\alpha/g = 6.4$. A vertical dashed line at $\tau = 0.6$ visually separates results into a Bo -independent region ($\tau \lesssim 0.6$) and Bo -dependent region ($\tau \gtrsim 0.6$) for $\theta_c = 60^\circ$. Similarly a dash-dotted line at $\tau = 0.9$ is drawn for $\theta_c = 19^\circ$. (Note that the transition times roughly translate to $\tau/\tau_{tip} \approx 0.2$ for $\theta_c = 60^\circ$ and $\tau/\tau_{tip} \approx 0.3$ for $\theta_c = 19^\circ$, with the tip breakup time τ_{tip} associated with both substrates only weakly depending on Bo .) The initial linear growth predicted by TFM (see (B1a,b)) is also given for comparison. The TFM results after the peak of $|F|$ are inconsistent with the model and so invalid. As a result they are not shown here. (b) Drop tip velocity obtained by DNS (constant contact angle) with increasing Bo (and simultaneously increasing $\alpha/g = 4.0, 5.3, 6.6, 7.9, 9.3$). A comparison with the experiments is made for $Bo \approx 5$. Again, an excellent collapse is seen in the Bo independent region for $\tau < 0.4$, and a clear shift in regime occurs for $\tau > 0.6$ when the curves start to fan out.

3.1. Early drop deformation dynamics

We first consider the early stage of drop deformation, where an axisymmetric flow field $\mathbf{u} = (u, w)$ is required to form a ligament from the initial sessile drop. For small time $t \ll 1$, we expect \mathbf{u} to be irrotational, and thus in Appendix B we derive an analytical theory for the velocity components, $u = u(r, t)$ and $w = w(z, t)$, that assumes a one-dimensional (1-D) spatial dependency. We term this theory the thin-film model (TFM) based on its required thin aspect-ratio condition, $L \ll R$, with R being the contact radius.

Next, we examine the early stage of drop deformation, combining experimental, DNS and TFM results. Figure 8 shows the time evolution of the drop tip velocity $w(L, \tau)$, re-normalized by the capillary speed u_σ defined in (2.11a–c), in both (a) experiments and (b) DNS of constant angle model for a range of Bo . In the comparison between $w(L, t)$ given by TFM and experimental measurements, we see that the slopes of the predicted w match well with the measured initial accelerations at early times when results collapse for all Bo in figure 8(a). Such a Bo -independent inertial regime is also clearly established by DNS in figure 8(b) for $\theta_c = 60^\circ$. The numerical results obtained for increasing Bo are compared with the measurement sequence of $\alpha/g = 6.3$ and $Bo = 5.0$. In DNS, a second transition regime with faster linear growth of $w(L, \tau)$ is also resolved in the range $0.4 \lesssim \tau \lesssim 0.6$. Beyond this point, the collapse of the w curves is lost. This is induced by surface tension effects captured by the finite Bo . The significance of these changes of regime is further discussed in § 3.2. Also, the observation in figure 8(a) that TFM performs better for the originally flatter drops of $\theta_c = 19^\circ$ than for the elongated drops of $\theta_c = 60^\circ$

is consistent with the thin-film assumption, which deteriorates faster over time for larger θ_c . Note that the linear growth given by TFM, although not far off, does not fully capture $w(L, \tau)$ in the entire inertial regime before end-pinching.

Importantly, the satisfactory performance of TFM developed in the large Bo and thin-film limits, i.e. $Bo \rightarrow \infty$, $L \rightarrow 0$, suggests that the early deformation of sessile drops with small contact angles is dominated by inertial acceleration. With its validity further discussed in [Appendix B.3](#), the TFM generates predictions for drop shapes merely based on the initial conditions. In § 3.3, we will use this initial shape deformation model for further development of the asymptotic theory for the opposite aspect-ratio limit (jet limit) to further gain insights into the tip ejection.

3.2. Regime change and the role of inertia

[Figure 8](#) shows the evolution of tip velocity $w(L, \tau)$. The initial growth of $w(L, \tau)$ appears universal for all Bo up to $\tau \approx 0.6$. Beyond this time, we observe a regime change. Specifically, the drop elongation process up to detachment can be separated into at least two regimes: first, an inertia-dominated regime; and second a capillarity-dominated regime. When comparing the time scales with the contact-angle evolution shown in [figure 6\(b\)](#), we see that the estimated regime change of drop tip velocity coincides with the convergence to the final receding angle value at the foot. The observed regime change signals a shift in the competition between inertia and surface tension governing the drop motion. To further confirm this and isolate the inertial effects, we here transition to examine this aspect via a numerical experiment as follows.

We initialize a numerical simulation of the drop elongation with a given imposed acceleration, here, $Bo = 5$. At time $\tau = 0.4$ the evolution is paused. Acceleration is removed and the system is left to evolve again. The drop thereby continues to deform under capillary effects and the inherited, already developed flow field established prior to $\tau = 0.4$. The subsequent evolution of the interface shape is shown in [figure 9\(a\)](#): the drop continues to slightly elongate up to approximately $\tau = 1.4$ and then retracts back to the substrate, without fragmenting, indicating that the capillary restoring forces overcome the inertial flow field inherited already by $\tau = 0.4$. [Figure 9\(b\)](#) shows the results from the same numerical experiment, but now taking the shape and flow field established at time $\tau = 0.6$ to restart the evolution without acceleration. The drop contour evolution under the developed velocity field and surface tension without acceleration shows that the interface continues to elongate and eventually fragments. In other words, by time $\tau = 0.6$, the deformation and flow field is such that capillary forces are no longer sufficient to stabilize the interface against the inherited inertia captured by the flow field. Interestingly, the size of the ejected tip drop in [figure 9\(b\)](#) is $R_{tip}/R_{eq} = 0.85$, which is close to the full DNS $R_{tip}/R_{eq} = 0.84$. This suggests that the inertial effects beyond $\tau = 0.6$ do not affect the drop size selection in this constant contact-angle physical picture. Instead, inertial effects mostly contribute to elongating the fluid mass of the emerging ligament to which the tip drop is attached. Indeed, an explicit comparison of the elongation is shown in the inset of [figure 9\(c\)](#), where acceleration contributes to the ligament elongation. Since $w(L, \tau) \sim \tau\sqrt{Bo}$, and therefore $L(\tau) \sim \tau^2\sqrt{Bo}$, is valid in the high Bo limit as shown in (B12), we observe in the inset of [figure 9\(c\)](#) that acceleration effects contribute to elongation of the ligament to which the tip drop is attached, while the size of the tip drop determined as early as $\tau = 0.6$, is not affected. Indeed, we will show in § 3.3.2 that the elongation process is captured well by a free-fall model, i.e. under constant acceleration, obtained in the $Bo \rightarrow \infty$ limit. There, effects of the end-pinching process dominated by

Fragmentation from inertial detachment of a sessile droplet

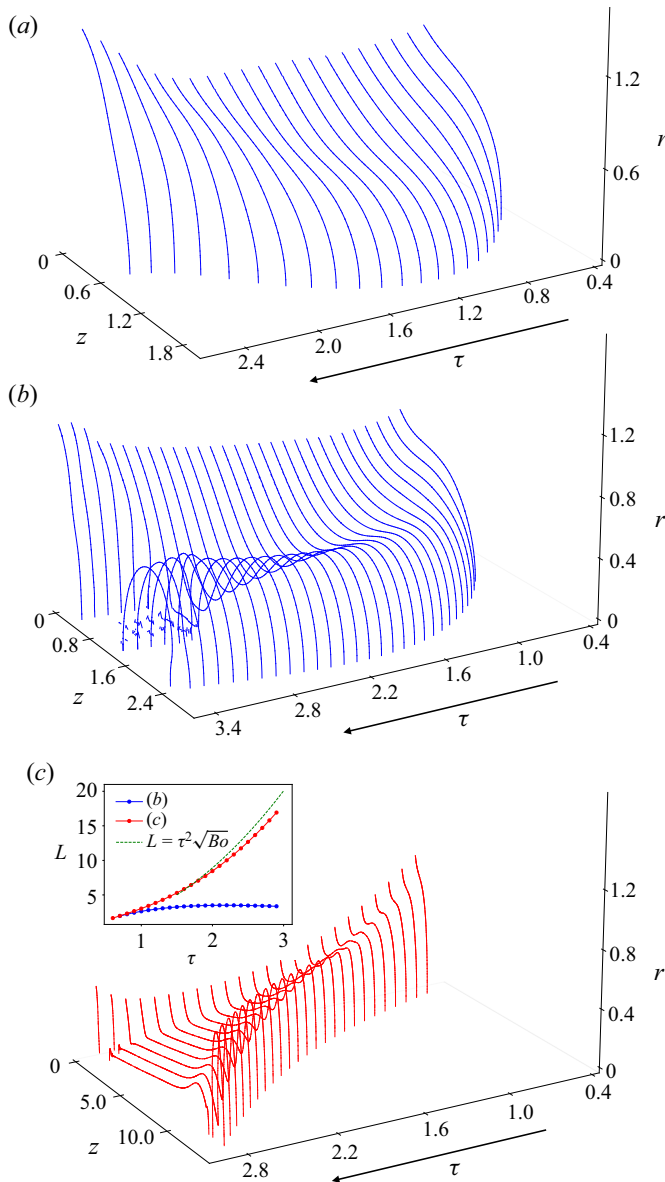


Figure 9. To confirm the shift in regime discussed in § 3.2 and suggested by figure 8 from an inertia-dominated phase to a capillarity-dominated phase, we proceed with a numerical experiment using DNS: we let the droplet deform under a particular acceleration, for $Bo = 5$ here. We interrupt the evolution at a transition time at which we remove acceleration. Thereafter, we restart the evolution from the interface shape and the inherited established flow field. (a) Evolution of the deforming interface upon initialization from the shape and flow field established by $\tau = 0.4$. At this time, capillary effects overcome the inertia imparted to the drop by acceleration. The drop retracts back to the substrate after a brief elongation up to $\tau \approx 1.4$ and failure to fragment. (b) Evolution of the interface shape when restarted from the inherited interface shape and flow field established by $\tau = 0.6$, the time of transition from a Bo -independent to a Bo -dependent regime (figure 8). At this transition, the drop continues to elongate and fragments. (c) Interface evolution under constant acceleration, i.e. no interruption/restart. The inset shows the ligament length L as a function of time τ , consistent with our prediction (B12). The sizes of tip drop R_{tip}/R_{eq} in (b,c) are essentially the same, ≈ 0.84 – 0.85 , consistent with a primary drop size selection early in the ligament evolution, i.e. as early as $\tau = 0.6$.

capillarity are incorporated via geometric constraint: attaching a spherical tip drop to the free-falling ligament when tip breaking occurs.

3.2.1. Estimating the tip-drop pinch-off time

Building on the insights of the preceding section where the drop detachment process is two staged with a shift in regime from inertia to capillary dominated, we discuss here an estimation of the tip breakup time τ_{tip} . As seen in [figures 8](#) and [24](#) already and discussed, the duration of the inertial regime, $\tau_{inertia}$, has a weak dependence on the wetting of the substrate, a function of equilibrium contact angle θ_c , i.e. $\tau_{inertia} = \tau_{inertia}(\theta_c)$. For example, from [figure 8\(a\)](#), $\tau_{inertia}(60^\circ) \approx 0.6$ and $\tau_{inertia}(19^\circ) \approx 0.9$. Once the system transitions into the second regime, surface tension dominates the local dynamics of necking, ultimately leading to the pinch off of the tip drop. This pinch-off dynamics is analogous to end-pinchng for inviscid filaments (e.g. Schulkes [1996](#)), shown numerically to have a dimensional tip-drop pinch-off time $5T_\sigma$, where T_σ is defined as in [\(2.10a-c\)](#) taking dimensional \tilde{R}_{eq} to be a uniform filament radius \tilde{R}_f proportional to the dimensional tip-drop size, with $\tilde{R}_f \approx \tilde{R}_{tip}/1.55$. Therefore, combining the insights gained from the two regimes and using the capillary time scale [\(2.10a-c\)](#) for non-dimensionalization, we obtain

$$\tau_{tip}(\theta_c) \approx \tau_{inertia}(\theta_c) + 5 \left(\frac{R_{tip}}{1.55} \right)^{3/2}. \quad (3.1)$$

Approximating $R_{tip} = \tilde{R}_{tip}/R_{eq} = 0.8$, [\(3.1\)](#) evaluates to $\tau_{tip}(60^\circ) \approx 2.5$ and $\tau_{tip}(19^\circ) \approx 2.8$. These estimations capture the experimental measurements shown in [figure 5\(b\)](#) very well. Notably, the drop radius-to-ligament width ratio of ≈ 1.5 was also observed experimentally to be robust and independent of the impact Weber number for the continuous end-pinchng of ligaments along the rim of canonical unsteady sheet fragmentation upon drop impact on a substrate of comparable size to that of the drop (Wang & Bourouiba [2018](#)), reflecting, also there, a robust local capillary-dominated dynamics.

3.3. Slender-jet model

As the drop deforms into a ligament under inertial acceleration, its length over width aspect ratio, characterized by L/R , increases, approaching a geometry that may be best captured by a slender-jet dynamics, hereafter referred to as the slender-jet model (SJM). As introduced by Eggers & Dupont ([1994](#)), the SJM is based on lubrication theory that simplifies, at a given time, the 2-D flow field of a fluid column into a 1-D extensional flow field with small radial velocity compared with the axial component such that $u \ll w = w(z, t)$. This model has been widely used for analysing jet breakup (Eggers & Villermaux [2008](#); Contò *et al.* [2019](#); Pierson *et al.* [2020](#)). Here, we develop an approximate solution to the SJM, again for large Bo , where the surface tension effects at both the ligament tip and foot are modelled accounting for the robust geometrical constraints observed in the experiments. In particular, such modelling enables us to gain key insights into the physical picture leading to the robust experimental observations discussed in [§ 2.4](#) pertaining to tip-drop ejection.

3.3.1. The slender-jet model governing equations

Formally derived as the $(L/R)^{-1} \rightarrow 0$ asymptotic limit of the system [\(2.7\)](#) and [\(2.9\)](#), the inviscid slender-jet equations (Papageorgiou & Orellana [1998](#)) under our default inertial

scaling (2.10a–c) read

$$\partial_t h = -w\partial_z h - \frac{h}{2}\partial_z w, \tag{3.2a}$$

$$\partial_t w = -w\partial_z w - \frac{1}{Bo}\partial_z \kappa + 1, \tag{3.2b}$$

where ∂_t and ∂_z denote partial derivatives with respect to t and z , respectively, and the curvature κ is

$$\kappa = \kappa(z, t) = \frac{1}{h(1 + (\partial_z h)^2)^{1/2}} - \frac{\partial_z^2 h}{(1 + (\partial_z h)^2)^{3/2}}. \tag{3.3}$$

Equivalently, the slender-jet system (3.2) with boundary condition $h(L, t) = 0$ ensures conservation of volume, momentum and energy, respectively, as follows (Eggers & Dupont 1994; Contò *et al.* 2019):

$$\frac{d}{dt} \int_{z_b}^{L(t)} h^2 dz = \frac{d}{dt} \left(\frac{V_{jet}}{\pi} \right) = \left[h^2 w \right]_{z=z_b}, \tag{3.4a}$$

$$\frac{d}{dt} \int_{z_b}^{L(t)} wh^2 dz = \frac{V_{jet}}{\pi} + \left[h^2 w^2 - \frac{1}{Bo} K_1(z, t) \right]_{z=z_b}, \tag{3.4b}$$

$$\frac{d}{dt} \int_{z_b}^{L(t)} \left\{ \left(\frac{w^2}{2} - z \right) h^2 + \frac{2h}{Bo} (1 + (\partial_z h)^2)^{1/2} \right\} dz = \left[\frac{w^3 h^2}{2} - wh^2 z + \frac{1}{Bo} K_2(z, t) \right]_{z=z_b}, \tag{3.4c}$$

where

$$\left. \begin{aligned} K_1(z, t) &= \frac{h}{(1 + (\partial_z h)^2)^{1/2}} + \frac{h^2 \partial_z^2 h}{(1 + (\partial_z h)^2)^{3/2}}, \\ K_2(z, t) &= \kappa h^2 w - \frac{2(\partial_z h)(\partial_t h)h}{(1 + (\partial_z h)^2)^{1/2}}. \end{aligned} \right\} \tag{3.5}$$

Here, the integral terminal $z_b \in (0, L)$ is a constant parameter that defines a jet’s lower boundary. Accordingly, V_{jet} is the jet volume. Note that $z_b \neq 0$ because (3.2) does not account for any solid–liquid stress at the contact plane $z = 0$. If we choose $z_b \ll 1$, a thin capillary boundary layer is then expected for $z \in [0, z_b)$, where surface tension and boundary stresses would govern the drop foot region.

Notably, it is possible to identify the kinetic, potential and surface energies of the jet domain as $E_k = \int_{z_b}^L w^2 h^2 / 2 dz$, $E_p = \int_{z_b}^L -zh^2 dz$ and $E_s = \int_{z_b}^L 2h\sqrt{1 + h_z^2}/Bo dz$, respectively, in the energy conservation law (3.4c). In general, this energy equation is auxiliary to the already closed system (3.2) for an incompressible jet. However, as we will see, we utilize this additional equation to enable closure for the jet’s breaking topology without having to solve the evolution equations over time.

3.3.2. Slender-jet free-fall regime

Having introduced the slender-jet equations (3.2), we now develop an analytical solution starting with a steady velocity ansatz w for the force balance (3.2b) that also satisfies the

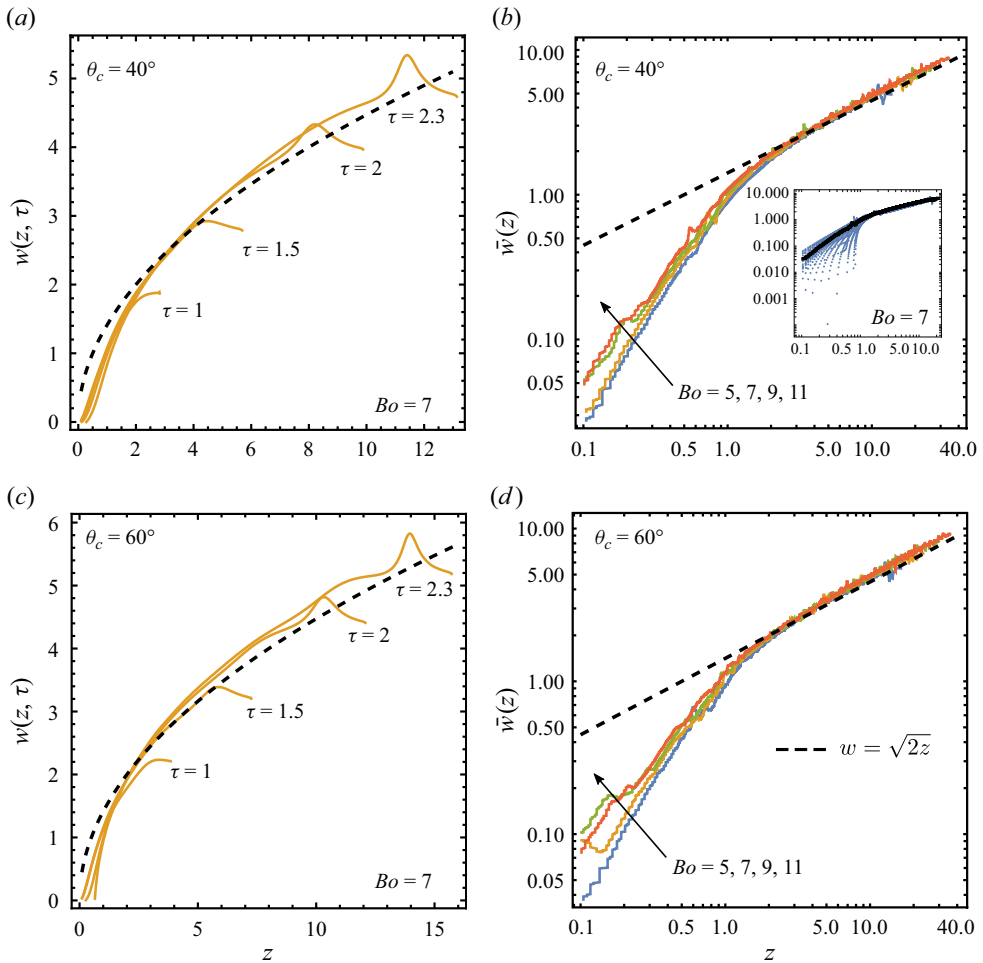


Figure 10. (a) Central axial velocity $w(r = 0, z, t)$ as a function of z , for $Bo = 7$, from DNS of constant $\theta_c = 40^\circ$ at different times (solid), compared with the steady profile $w = \sqrt{2z}$ (3.6) (dashed). (b) Time-averaged DNS velocity profiles $\bar{w} = \bar{w}(z)$ for different Bo (solid) shown in log–log form in order to more easily show the range. The inset gives an example of \bar{w} (black solid line) from various temporal profiles of w (blue and dotted) for $Bo = 5$. Panels (c,d) give the corresponding results to (a,b) for $\theta_c = 60^\circ$. This DNS benchmark validates that (3.6) gives the correct universal steady velocity profile for a ligament in its middle region sufficiently far from its two ends, i.e. $z \gtrsim O(1)$ and $L - z \gtrsim O(1)$, at all Bond numbers.

boundary condition $\lim_{z \rightarrow 0} w = 0$. This solution would describe a free-falling ligament in the $Bo \rightarrow \infty$ limit. In this limit and for these conditions, we obtain for all $t > 0$

$$w(z, t) = \sqrt{2z}. \tag{3.6}$$

Accuracy of such a steady velocity profile is directly assessed in figure 10 with DNS of a constant contact-angle model using $\theta_c = 40^\circ$ (10a,b) and $\theta_c = 60^\circ$ (10c,d). For example, for $Bo = 7$, figure 10(a,c) gives the central axial velocity $w(r = 0, z, t)$ as a function z at four different times up to tip-drop pinch off. All the profiles indeed follow the steady profile (3.6) except for the region near the tip as $z \rightarrow L$. Clearly, away from the extremity of the ligament the steady solution does capture a universal velocity profile that is robust for a range of Bo , as seen in figure 10(b,d). Indeed, these figures show an ensemble time average

\bar{w} taken from $w(0, z, t)$ over all simulated times t for a range of Bo . These observations support (3.6) to capture the profile of the ligament region away from its two extremities. Notably, we qualify the success of (3.6) strictly under the conditions that a) the inviscid flow limit applies, and b) the imposed inertial acceleration is constant (see (3.2b)). This is because both viscous effects and variable forcing over time can significantly alter the ligament's stretching dynamics (Villermaux 2012; Vincent *et al.* 2014).

Having established support for (3.6), the continuity equation (3.2a) can be further solved with the general solution $h(z, t) = H(t - \sqrt{2z})z^{-1/4}$, where $H(\cdot) \in C^1$ is arbitrary. To determine H , we first specify the initial condition at time $t = t_s$ when the SJM becomes applicable, by denoting

$$\tilde{h}(z, \tilde{t}) \equiv h(z, t_s + \tilde{t}), \quad \tilde{h}_0(z) \equiv \tilde{h}(z, 0), \quad \tilde{t} \equiv t - t_s \geq 0. \quad (3.7a-c)$$

Further, since we are interested in the jet domain $z \in [z_b, L]$, an additional boundary condition at $z = z_b$ is required. By taking $z_b \rightarrow 0$, so that physically $w|_{z=z_b} \rightarrow 0$ at the substrate, we assume (3.2a) evaluated within the capillary layer for $z \in [0, z_b]$ follows the dominant balance $|w\partial_z h/\partial_t h| \ll 1$ and $|w\partial_z h/(h\partial_z w)| \ll 1$. As such, we arrive at the following approximate equation:

$$\partial_t h + \frac{h}{2\sqrt{2z}} = 0, \quad (3.8)$$

for h using (3.6), whose solution at $z = z_b$ as a boundary condition is given by

$$\tilde{h}(z_b, \tilde{t}) \equiv \tilde{h}_b(\tilde{t}) = \exp\left(-\frac{\tilde{t}}{2\sqrt{2z_b}}\right)\tilde{h}_0(z_b), \quad (3.9)$$

where the initial value (3.7a-c) is used. Note that the asymptotic conditions that lead to (3.9) as $z_b \rightarrow 0$ may be assessed upon direct substitution into (3.2a), yielding

$$\left|\frac{w\partial_z h}{\partial_t h}\right|_{z=z_b} \sim \frac{w}{z_b}, \quad \left|\frac{w\partial_z h}{h\partial_z w}\right|_{z=z_b} \sim \frac{wz_b^{-3/2}}{\partial_z w}. \quad (3.10)$$

Therefore, an essential singularity of the form $w \sim o(e^{-1/z_b})$ is needed for the second term in (3.10) to vanish, while any algebraic profile, e.g. (3.6) derived in the $Bo \rightarrow \infty$ limit, leads to divergence. Indeed, we observe in figure 10 that, as $z \rightarrow 0$, the simulated w from DNS approaches zero much faster than the steady profile. Presently, we do not explore the capillary boundary layer for $z \in [0, z_b]$ in full detail, but assume that there is a sharp transition of the flow dominance from surface tension to inertia at the critical slice $z = z_b$, hence (3.9) is obtained as an approximation. This hypothesis enables the analytical solution to follow, and is subsequently justified by experiments.

With initial-boundary values specified in (3.7a-c) and (3.9), the 1-D transport equation (3.2a) can be solved for all z, t following a standard method-of-characteristic procedure. As a result

$$\tilde{h}(z, \tilde{t}) = \tilde{h}_{free-fall} \equiv \begin{cases} \sqrt{1 - \frac{\tilde{t}}{\sqrt{2z}}}\tilde{h}_0\left(\frac{1}{2}(\tilde{t} - \sqrt{2z})^2\right), & \zeta(z_b, \tilde{t}) \leq z \leq \zeta(\tilde{L}_0, \tilde{t}), \\ \left(\frac{z_b}{z}\right)^{1/4} \exp\left(-\frac{\tilde{t} - \sqrt{2}(\sqrt{z} - \sqrt{z_b})}{2\sqrt{2z_b}}\right)\tilde{h}_0(z_b), & z_b \leq z \leq \zeta(z_b, \tilde{t}), \end{cases} \quad (3.11)$$

where \tilde{L}_0 is the ligament length at $\tilde{t} = 0$, i.e. $\tilde{h}_0(\tilde{L}_0) = 0$, and

$$\zeta(Z, \tilde{t}) = \frac{1}{2} \left(\tilde{t} + \sqrt{2Z} \right)^2. \quad (3.12)$$

Here, $\zeta(Z, \tilde{t})$ gives the advected position of a Lagrangian slice, parameterized by its original location $z = Z$ at $\tilde{t} = 0$, after time \tilde{t} by the uniform axial velocity w . That is, ζ solves the ordinary differential equation (ODE) system

$$\partial_{\tilde{t}} \zeta = w(\zeta(Z, \tilde{t})), \quad \zeta(Z, 0) = Z \in [z_b, \tilde{L}_0], \quad (3.13a,b)$$

with w given by (3.6).

Figure 11 shows experimental evidence that the free-fall solution (3.11) captures the measurements made for both contact angles well. First, with $\theta_c = 60^\circ$ and $Bo = 7$, figure 11(a) gives the corresponding drop radius h as a function of capillary time τ for an increasing sequence of $z/\lambda = 0.5, 1, \dots, 12$, where λ is the capillary wavelength defined in (2.11a–c). Using a logarithmic scale, we observe that, at each fixed z that is sufficiently large ($z/\lambda \gtrsim 2$), there always exists a transitioning time when h peaks and exponential thinning occurs afterwards. However, at small distances closer to the substrate, e.g. $z/\lambda = 0.5, 1$, the rate of h thinning appears slower than exponential, indicating the effect of the capillary boundary layer. Therefore, we can empirically identify a critical time t_s and location z_b from measurements such that the approximated boundary condition (3.9) is reasonable. For example, by choosing $\tau_s = t_s/\sqrt{Bo} = 0.2$ and $z_b = 2\lambda$ (labelled in figure 11(a)), we compare the h data directly against (3.11) using similarity variables $\xi \equiv [\tilde{t} - \sqrt{2}(\sqrt{z} - \sqrt{z_b})]/(2\sqrt{2z_b})$ and $\eta \equiv (z/z_b)^{1/4} \tilde{h}(z, \tilde{t})/\tilde{h}_0(z_b)$ in figure 11(b). It is shown that the roughly parallel curves in figure 11(a), as well as additional data for larger $z/\lambda = 16, 20, 24$, all collapse onto the theoretical solution $\eta = e^{-\xi}$. The biggest deviation is found for $z/\lambda = 2$ in this case as ξ (or equivalently, t) increases, again exhibiting long term capillary influences. Similarly, figure 11(c,d) reveals the same findings using experimental data for $\theta_c = 19^\circ$ and $Bo = 6$. Compared with the previous case, here, $\tau_s = 1.7$ and $z_b = 4\lambda$ are chosen for (ξ, η) in figure 11(d), indicating a thicker boundary layer with respect to the capillary length for a more wetting surface.

3.3.3. Lollipop model for tip-drop breakage

Although we have successfully modelled the free-falling region of a ligament in § 3.3.2, the surface tension effects that cause necking near the tip and its ultimate pinch-off are still fundamentally missing in the infinite Bo theory. In this section, to recover this critical behaviour, we use the insights gained from the geometrical constraints of the dynamics to develop a first-order ‘lollipop’ model solution to the SJM for a ligament at the exact tip breaking instant. We achieve this by solving the conservation form of the SJM given in (3.4) for infinite Bo over a defined domain that divides a breaking ligament at $t = t_{tip}$ into four parts: (i) a base cone for $0 \leq z \leq z_b$, (ii) a free-falling region described by (3.11) for $z_b < z \leq z_c$, (iii) a connecting cone within $z_c \leq z \leq \mathcal{L} - 2R_{tip}$ where $\mathcal{L} = L(t_{tip})$ is the breaking jet length and (iv) an ejected spherical tip of radius R_{tip} between $\mathcal{L} - 2R_{tip} \leq z \leq \mathcal{L}$. A schematic of the composite geometry that we use to guide the approach, with a lollipop shape, is illustrated in figure 12.

Next, we elucidate specific design of the four parts that contribute to the lollipop model. First, we make the same constant contact-angle assumption as in § 2.3.2 for DNS, and additionally approximate the drop shape in its foot capillary layer to be conical, as

Fragmentation from inertial detachment of a sessile droplet

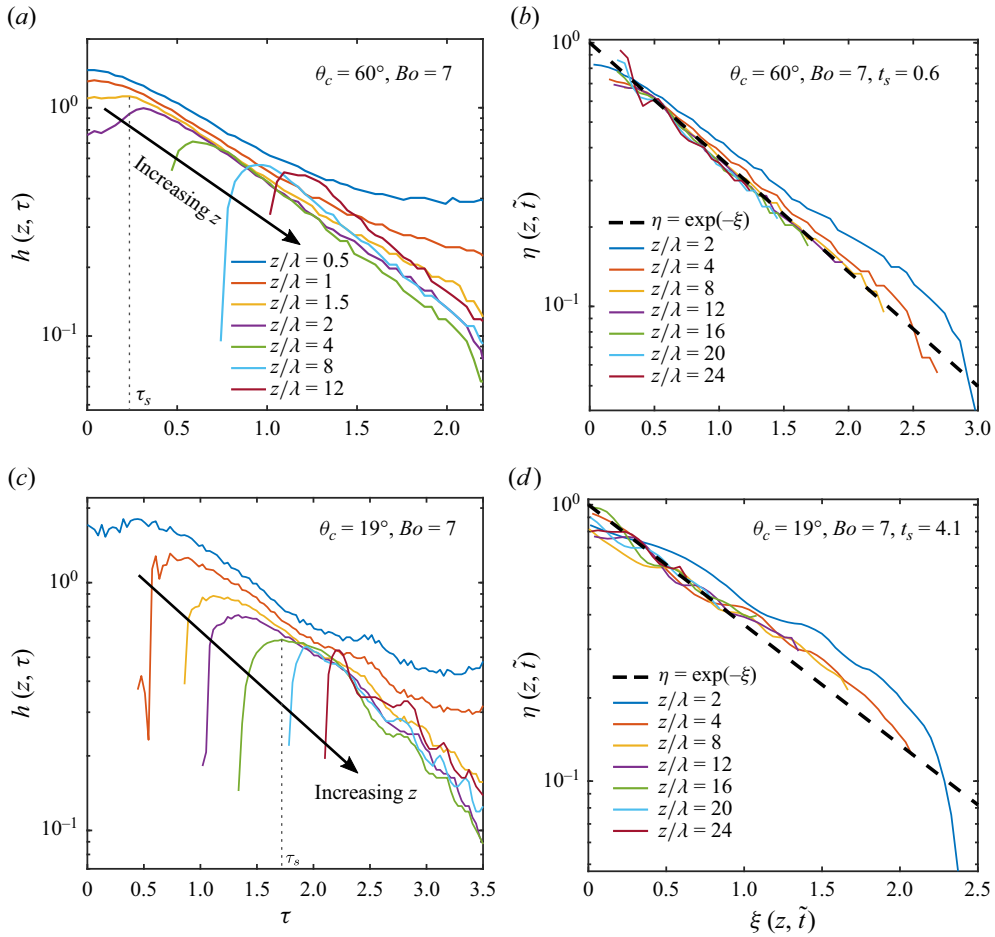


Figure 11. (a) Drop radius $h(z, \tau)$ as a function of capillary time τ measured experimentally at different heights of wavelength $z/\lambda = 0.5, 1, 1.5, 2, 4, 8, 12$, using $\theta_c = 60^\circ$ and $Bo = 7$ ($\alpha/g = 9.9$). (b) Radius measurements at different heights $z/\lambda = 2, 4, 8, 12, 16, 20, 24$ plotted in term of similarity variables $\xi \equiv [\tilde{t} - \sqrt{2}(\sqrt{z} - \sqrt{z_b})]/(2\sqrt{2z_b})$ and $\eta \equiv (z/z_b)^{1/4} \tilde{h}(z, \tilde{t})/\tilde{h}_0(z_b)$, with parameters $\tau_s = 0.2$ ($t_s = 0.6$) and $z_b = 2\lambda$ (labelled by the dashed line in a). The resulting curves collapse onto the free-fall solution $\eta = \exp(-\xi)$ given in (3.11) by the dashed line. (c, d) Same as in (a, b) except $\theta_c = 19^\circ$ and $Bo = 7$ ($\alpha/g = 6.2$). The transition parameters used for (d) are $\tau_s = 1.7$ ($t_s = 4.1$), $z_b = 4\lambda$. Panels (a, c) share the same keys. We demonstrate here that, with an appropriately identified boundary for the capillary layer, the ligament radius in the inertial regime is well predicted by the free-fall solution derived from the $Bo \rightarrow \infty$ limit of the SJM.

generally observed in experiments. This leads to the following shape function \tilde{h}_{base} for $z \in [0, z_b]$:

$$\tilde{h}(z, \tilde{t}) = \tilde{h}_{base}(z, \tilde{t}; z_b, \theta_c) \equiv (z_b - z) \cot \theta_c + \tilde{h}_b(\tilde{t}; z_b), \quad (3.14)$$

where \tilde{h}_b is the boundary condition defined in (3.9) of exponential necking. By conserving the total drop volume, we can then calculate the slender-jet portion of the ligament volume V_{jet} (excluding the base cone) as

$$V_{jet}(\tilde{t}) = \frac{4\pi}{3} - \int_0^{z_b} \pi \tilde{h}_{base}^2 dz = \frac{\pi}{3} \left[4 - z_c \left(3\tilde{h}_b^2 + 3\tilde{h}_b z_b \cot \theta_c + z_b^2 \cot^2 \theta_c \right) \right]. \quad (3.15)$$

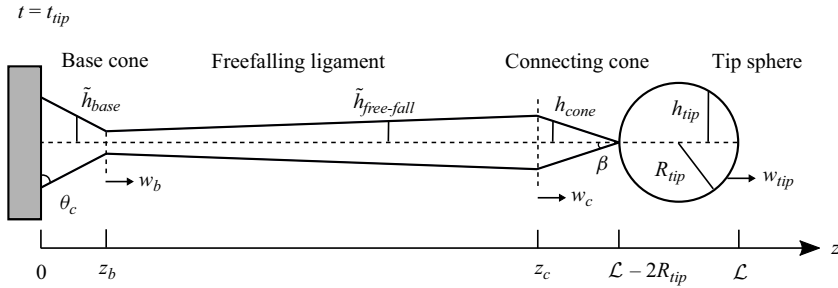


Figure 12. Schematic of the lollipop model for a tip breaking ligament at $t = t_{tip}$, including a base cone ($0 \leq z \leq z_b$), a free-falling ligament ($z_b \leq z \leq z_c$), a connecting cone ($z_c \leq z \leq \mathcal{L} - 2R_{tip}$) and a tip sphere ($\mathcal{L} - 2R_{tip} \leq z \leq \mathcal{L}$). Here, θ_c is the equilibrium contact angle, w_b is the boundary flow velocity for the free-fall solution (3.11), w_c is the steady cone velocity (3.20), $\beta = 18^\circ$ is the fixed pinch-off angle, R_{tip} is the radius of the ejecting spherical tip of uniform velocity w_{tip} . The h -profiles of the jet radius are labelled for each region and given in (3.21a,b).

Substituting \tilde{h}_b and V_{jet} into (3.4a) thus gives the flow velocity across the critical plane $z = z_b$ based on volume flux

$$w_b(\tilde{t}; z_b, \theta_c) = \frac{z_b^{3/2} e^{\tilde{t}/2\sqrt{2z_b}} \cot \theta_c}{2^{3/2} \tilde{h}_0(z_b)} + \left(\frac{z_b}{2}\right)^{1/2}. \quad (3.16)$$

Importantly, the boundary velocity w given by (3.16) differs from the steady profile (3.6) evaluated at $z = z_b$. We demonstrate in Appendix D.1 that the time dependence introduced in w_b necessarily corrects the volumetric flow rate dV_{jet}/dt .

Above $z > z_b$, as discussed in §3.3.2, we proceed with the assumption that a discontinuous transition into the free-fall regime occurs, acquiring for the lollipop model the ligament shape and velocity given by (3.11) and (3.6), respectively. However, to capture breakup in this model, the tip end of the free-fall solution is replaced by an ejecting drop. Informed by the experiments as well as the recent self-similar solution derived by Contò *et al.* (2019), we propose that at breakup time t_{tip} the ejecting drop is spherical in shape and uniform in velocity. This gives for $z \in [\mathcal{L} - 2R_{tip}, \mathcal{L}]$

$$h(z, t_{tip}) = h_{tip}(z; \mathcal{L}, R_{tip}) \equiv \sqrt{R_{tip}^2 - (z + R_{tip} - \mathcal{L})^2}, \quad w(z) = w_{tip}, \quad (3.17)$$

where the tip radius R_{tip} , the total ligament length at breakup $\mathcal{L} = L(t_{tip})$ and the tip velocity w_{tip} are to be determined in the next section. Note that a spatially uniform w_{tip} ensures the tip drop remains spherical after breakup.

To link the free-falling ligament and the ejecting tip, we further devise a connecting cone in between so that the combined lollipop model reasonably emulates an end-pinching filament, e.g. Day, Hinch & Lister (1998). Specifically, Day *et al.* (1998) obtained a self-similar solution to the Euler equations for axisymmetric inviscid drop breakup, and revealed a double-cone structure at breaking point with an inner angle of 18° made by the ligament and an outer angle of 113° by the breaking tip. These angles were numerically confirmed again by Leppinen & Lister (2003). Here, we adopt the inner cone of fixed angle $\beta = 18^\circ$ for $z \in [z_c, \mathcal{L} - 2R_{tip}]$ as follows:

$$h(z, t_{tip}) = h_{cone}(z; \mathcal{L}, R_{tip}) \equiv -(z - \mathcal{L} + 2R_{tip}) \cot \beta + \delta, \quad (3.18)$$

where the matching point $z = z_c$ is determined by requiring

$$\tilde{h}_{free-fall}(z_c, t_{tip} - t_s) = h_{cone}(z_c), \quad (3.19)$$

Fragmentation from inertial detachment of a sessile droplet

with $\tilde{h}_{free-fall}$ given in (3.11). A minimum neck radius $\delta \sim O(10^{-3})$ at $z = \mathcal{L} - 2R_{tip}$ is formally introduced in (3.18) to indicate the end of inviscid pinch off before a viscous solution takes over (Eggers & Villermaux 2008). However, because δ is small, its effect on the cone shape and momentum is negligible. We consider the velocity field within this connecting cone steady for simplicity, hence computed using (3.2a), i.e. $\partial_z(wh^2) = 0$, as

$$w(z) = w_c(z; \mathcal{L}, R_{tip}) \equiv \frac{2z_c h_{cone}(z_c)^2}{h_{cone}(z)^2}. \tag{3.20}$$

Markedly, having $\delta \rightarrow 0$ introduces a singularity of w_c as $z \rightarrow \mathcal{L} - 2R_{tip}$, which is acceptable for calculating momentum because wh^2 remains constant throughout the cone, but is problematic for the energy estimation if $\delta = 0$. We address this point in detail in [Appendix D.2](#).

In summary, using (3.14), (3.11), (3.18), (3.17), (3.16) and (3.20), we have approximated the breaking jet's shape and velocity at $t = t_{tip}$, (equivalently, $\tilde{t} = \tilde{t}_{tip} = t_{tip} - t_s$) by

$$h(z) = \begin{cases} \tilde{h}_{base}(z, \tilde{t}_{tip}), & z \in [0, z_b], \\ \tilde{h}_{free-fall}(z, \tilde{t}_{tip}), & z \in [z_b, z_c], \\ h_{cone}(z), & z \in [z_c, \mathcal{L} - 2R_{tip}], \\ h_{tip}(z), & z \in [\mathcal{L} - 2R_{tip}, \mathcal{L}] \end{cases}, \quad w(z) = \begin{cases} w_b(z, t_{tip}), & z = z_b, \\ \sqrt{2z}, & z \in [z_b, z_c], \\ w_c(z), & z \in [z_c, \mathcal{L} - 2R_{tip}], \\ w_{tip}, & z \in [\mathcal{L} - 2R_{tip}, \mathcal{L}], \end{cases} \tag{3.21a,b}$$

where t_{tip} , R_{tip} , \mathcal{L} and w_{tip} are the four unknown variables to be calculated next. Note that we assumed in the lollipop model that tip ejection always precedes foot breaking, which is not always experimentally observed for large Bo . Nonetheless, we will show in § 3.4 and [Appendix D.1](#) that, if foot breaking should occur first at $t = t_{foot} < t_{tip}$, because w_b decays rapidly in our lollipop model, only negligible mass, momentum or energy can be transported from the foot into the slender jet during $t_{foot} < t < t_{tip}$.

3.3.4. Solution process

Here, we determine the four SJM lollipop parameters, t_{tip} , R_{tip} , \mathcal{L} and w_{tip} , using the weak form equations (3.4). However, without solving the evolution system as a continuous function of time, closure relies on additional access to at least one of the four unknowns. We choose to estimate tip breakup time t_{tip} based on the empirical relation (3.1) and show in the following that the resulting lollipop structure, particularly the tip size R_{tip} , depends weakly on t_{tip} within a reasonable range of its values.

To proceed, the $Bo \rightarrow \infty$ limit of (3.4) is integrated over $0 \leq \tilde{t} \leq \tilde{t}_{tip}$, generating

$$\pi \int_{z_b}^{\mathcal{L}} h^2 dz = V_{jet}(\tilde{t}_{tip}), \tag{3.22a}$$

$$\pi \int_{z_b}^{\mathcal{L}} wh^2 dz = P(\tilde{t}_{tip}) = P(0) + \int_0^{\tilde{t}_{tip}} \left(V_{jet} + \pi \tilde{h}_b^2 w_b^2 \right) d\tilde{t}, \tag{3.22b}$$

$$\pi \int_{z_b}^{\mathcal{L}} \left(\frac{w^2}{2} - z \right) h^2 dz = E(\tilde{t}_{tip}) = E(0) + \pi \int_0^{\tilde{t}_{tip}} \left[\left(\frac{w_b^2}{2} - z \right) \tilde{h}_b^2 w_b \right] d\tilde{t}, \tag{3.22c}$$

where h and w are piecewise and given by the lollipop model (3.21a,b); \tilde{h}_b and w_b are respectively found in (3.9) and (3.16); the slender-jet volume V_{jet} is defined in (3.15), and

its shifted initial momentum P and net mechanical energy E follow as

$$P(0) = \pi \int_{z_b}^{\tilde{L}_0} w(z) \tilde{h}_0(z)^2 dz, \quad E(0) = \pi \int_{z_b}^{\tilde{L}_0} \left(\frac{w(z)^2}{2} - z \right) \tilde{h}_0(z)^2 dz = 0, \quad (3.23a,b)$$

where $w(z) = \sqrt{2z}$ from (3.6) is used, and \tilde{h}_0 is the shifted initial shape (3.7a–c) of length \tilde{L}_0 . All integrals involved in (3.22) can be carried out exactly. The resulting expressions are lengthy and therefore omitted for brevity. Nevertheless, for any given initial drop shape \tilde{h}_0 and estimate of the break time t_{tip} , (3.22) forms an explicit algebraic system from which R_{tip} , \mathcal{L} and w_{tip} can be solved, under the physical constraints that $0 < R_{tip} < 1$, $\tilde{L}_0 < \mathcal{L} < \zeta(\tilde{L}_0, \tilde{t}_{tip})$. With ζ given by (3.12), the latter condition forbids the ligament tip to travel at free fall for all time without capillary retraction. In Appendix D.2 we further simplify the energy equation (3.22c) and establish a reduced expression, shown to be highly accurate, which reads

$$w_{tip}^2 = 2(\mathcal{L} - R_{tip}), \quad (3.24)$$

and expresses that the tip drop is ejected at a speed given by its free-falling centre, as per (3.6). Also, (3.24) eliminates the minimum neck radius δ introduced in (3.20) and its corresponding energy singularity. Hence, we can safely proceed with $\delta = 0$ for mathematical convenience.

3.4. Results of the SJM lollipop

In this section we present solutions to the SJM lollipop system with comparisons with simulations and experiments. Properties of the lollipop theory are discussed.

3.4.1. Comparison with DNS and experiments

The shapes of the ligament at tip breakup time given by DNS of the constant contact-angle model and the SJM lollipop are shown in figure 13(a) for $\theta_c = 60^\circ$ and $Bo = 4, 5, 6, 7$. The shifted initial shapes, \tilde{h}_0 , fed into the lollipop model (see (3.7a–c)) are selected from simulated shapes for each Bo that have clearly developed curvature inflection (see § 2.4.5), ensuring the beginning of the free-fall regime discussed in § 3.3.2. These curves are displayed using dot-dashed lines. The critical boundary plane (dotted vertical line) is empirically chosen as the capillary wavelength, $z_b = \lambda = 1/\sqrt{Bo}$, for the given 60° contact angle as a function of Bo . Effectively, we have estimated the thickness of the foot capillary boundary layer as $z_b = \lambda$. Consistently, we use the same breakup time t_{tip} from DNS in the model for each Bo .

As a result, we find that, for all Bo compared, the free-fall solution $\tilde{h}_{free-fall}$ given in (3.11) and the DNS results are in excellent agreement; the ejecting tip-drop size R_{tip} predicted by the lollipop model also aligns closely with the simulation. As Bo increases, the breaking jet length \mathcal{L} approaches the DNS result, producing an overall jet shape (3.21a,b), including the tip drop and the connecting cone, that matches the simulation well. It is interesting to note that the match continues to be good for large $Bo = 6, 7$ even though foot breaking starts taking place ahead of the tip pinch-off in DNS (figure 22a), hence, we would expect the base-cone assumption made by (3.14) to no longer be strictly correct. However, because the boundary radius $\tilde{h}_b(z_b, \tilde{t})$ found in (3.9) vanishes sufficiently fast, as $\tilde{t} \rightarrow \tilde{t}_{tip}$, the error in the mass and momentum fluxes associated with (3.14) end up not significantly affecting the jet solution above $z \geq z_b$. Further discussion of the error analysis for the base cone is given in Appendix F.

Fragmentation from inertial detachment of a sessile droplet

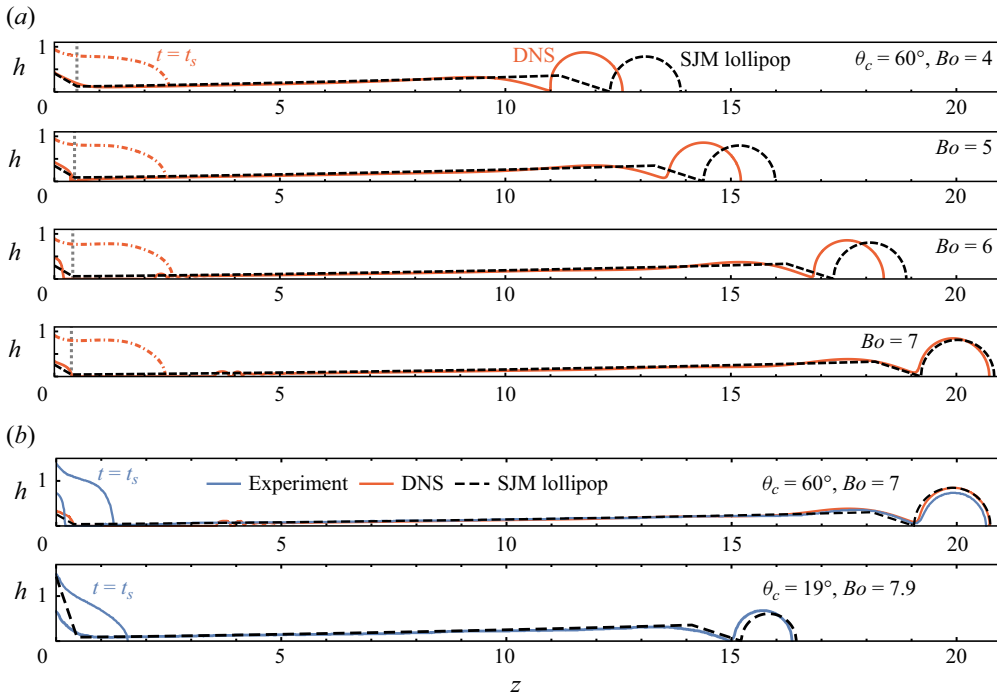


Figure 13. (a) Drop shapes for $\theta_c = 60^\circ$ at tip breaking times given by DNS (solid lines) and SJM lollipop (dashed) for increasing $Bo = 4, 5, 6, 7$. With appropriate shifted initial condition \tilde{h}_0 chosen from the simulation (dot-dashed), when $t_s/t_{tip} = 0.35, 0.31, 0.3, 0.27$, as well as the boundary thickness estimate $z_b = \lambda$ (dotted) for the Bo sequence, the lollipop model shows excellent agreement with DNS as Bo increases, particularly in terms of the tip-drop size. (b) Breaking shape comparison with experiments for both $\theta_c = 60^\circ$ and $\theta_c = 19^\circ$, with $Bo = 7$ and $Bo = 7.9$, respectively. The values of \tilde{h}_0 are chosen from experiments at $t_s/t_{tip} = 0.16$ for $\theta_c = 60^\circ$ and $t_s/t_{tip} = 0.35$ for $\theta_c = 19^\circ$; additionally, $z_b = \lambda$ and 1.3λ are respectively used in these two cases. Again, accuracy of the DNS result and lollipop structure for $z \geq z_b$ is validated by experiments.

Figure 13(b) shows again good agreement between the experimental ligament breaking shape for the different wetting ($\theta_c = 60^\circ$ and $\theta_c = 19^\circ$) and the SJM lollipop. The theoretical solutions are computed similarly using experimental \tilde{h}_0 at $t_s/t_{tip} = 0.16$ and $t_s/t_{tip} = 0.35$ for these two cases. The resulting lollipop solutions once again capture both DNS and experiments, particularly in the slender-jet domain $z \geq z_b$. To achieve such consistency, $z_b = \lambda$ is selected again for $\theta_c = 60^\circ$, while a larger $z_b = 1.3\lambda$ is used for the small angle 19° . Thus, between the two drops of different initial wetting, our choices for \tilde{h}_0 and z_b based on the first development of exponential thinning in an inertial-acceleration-dominated flow regime suggest a variable depth of the foot capillary boundary layer that increases with decreasing θ_c . This is expected: the more hydrophilic surface exerts a longer range of capillarity influence into the liquid. Further details on the differences between experiments, simulation and theory in the foot region $0 \leq z \leq z_b$ are discussed in the next section.

The overall success of SJM lollipop demonstrated in figure 13 shows that the role of surface tension that leads to neck tip pinch-off is adequately captured by a lollipop structure, where the breaking jet geometry satisfies conservation laws. The key insight is that our theory supports that the volume fraction of the deformed drop above the curvature inflection of the neck, at the inflection's very onset, already determines the volume of the

final tip-drop size well. This supports our observation made in § 2.4.5. In other words, the end-pinching tip-drop size selection essentially occurs at the very onset of the necking of the sessile drop and prior to a ligament formation. Indeed, the fact that the lollipop model based on a simple base-cone construction gives R_{tip} predictions of similar error compared with the early-stage volume fractions given in figure 7 shows that the boundary mass flux modelled through $z = z_b$ contributes mostly to the free-falling jet mass, rather than the selection of the size of the ejected tip drop. Further, after an inertial flow regime is established for an elongated jet, a continuous modulation of the foot dynamics that originates from the substrate and propagates through boundary fluxes is responsible for the second-order correction of R_{tip} to its final value. The effects of the flux accumulation on the second-order corrections of the ejected tip drop are examined in Appendix F.

3.4.2. Sensitivity analysis of the SJM lollipop with respect to its R_{tip} prediction

Next, we show robustness of the tip radius R_{tip} predictions given by the SJM lollipop using a sensitivity analysis in response to the control parameters z_b/λ , τ_{tip} (both expressed under capillary scaling) and Bo . Recall that the wavelength λ is a function of Bo as per (2.11a–c).

Unlike § 3.4.1, where we have supplied either simulated or experimental data of the shifted initial condition \tilde{h}_0 for the lollipop system, here, we examine its solutions derived *a priori* based on the TFM developed in Appendix B. Specifically, the TFM drop shape (B3) for $0 \leq t \leq t_s$ is obtained first, using the initial value h_0 given by a single parameter θ_c in (B6a,b). The switchover time from TFM to SJM, t_s , is chosen to be the time at which the TFM fails: when its corresponding numerical solution for $|F(t)|$ (B2), reaches its maximum, i.e. $\dot{F}(t_s) = 0$ (discussed in Appendix B.3). Although performance of the TFM starts deteriorating before such a switchover time, our choice offers a well-defined parametric drop shape $\tilde{h}_0(z; \theta_c)$ that can be calculated *a priori*, without experimental or DNS data. This leads to controllable initial conditions that we use to assess the sensitivity of the SJM. With \tilde{h}_0 determined, we proceed to prescribe, for any given Bo , a range of foot boundary thickness, z_b , and tip breakup time, τ_{tip} , to close the lollipop system (3.22) and assess the effect on R_{tip} prediction accuracy.

Figure 14(a) shows the drop shapes at $t = 0$, $t = t_s = 1.5$ for $\theta_c = 60^\circ$ and $Bo = 6$, and the lollipop structures obtained either using fixed $z_b/\lambda = 1$ but variable $\tau_{tip} = 2, 3$, or using constant $\tau_{tip} = 2.5$ but variable $z_b/\lambda = 0.5, 2$. This figure shows that the lollipop prediction of R_{tip} is consistently $0.8 < R_{tip} < 0.9$ for large Bo and holds for a wide range of system parameters τ_{tip} and z_b . This is true, despite the fact that the breaking jet length \mathcal{L} differs significantly between the applied parameters. Similar results hold for the higher wetting substrate (figure 14b), where again, either $\tau_{tip} = 2.5, 3.5$ is changed while fixing $z_b/\lambda = 1$, or $\tau_{tip} = 3$ is fixed while $z_b/\lambda = 0.5, 1.2$. We combine the above results in figure 14(c,d). Figure 14(c) shows the R_{tip} solutions when varying τ_{tip} and fixing z_b . Figure 14(d) shows the R_{tip} solutions for a fixed τ_{tip} and varying z_b . Clearly, R_{tip} depends weakly on τ_{tip} when Bo is large, and all solutions converge to a narrow band of values around $R_{tip} \approx 0.82$ as Bo increases, for both θ_c or more broadly $0.8 < R_{tip} < 0.9$ when Bo increases. The results show that the prediction of R_{tip} is robust to parameter changes and is approximately 10% higher than experimental measurements in comparison with the foot volume. The foot volume induced error will be explained in the next section.

Note that R_{tip} is more sensitive to increasing Bo when the wetting contact angle is small, especially for small Bo . This is expected as z_b determines the base-cone volume in the lollipop model (see (3.15)), whose effect is amplified when θ_c is small. Indeed, both (3.15) for the jet volume and (3.16) for the boundary velocity depend on θ_c via

Fragmentation from inertial detachment of a sessile droplet

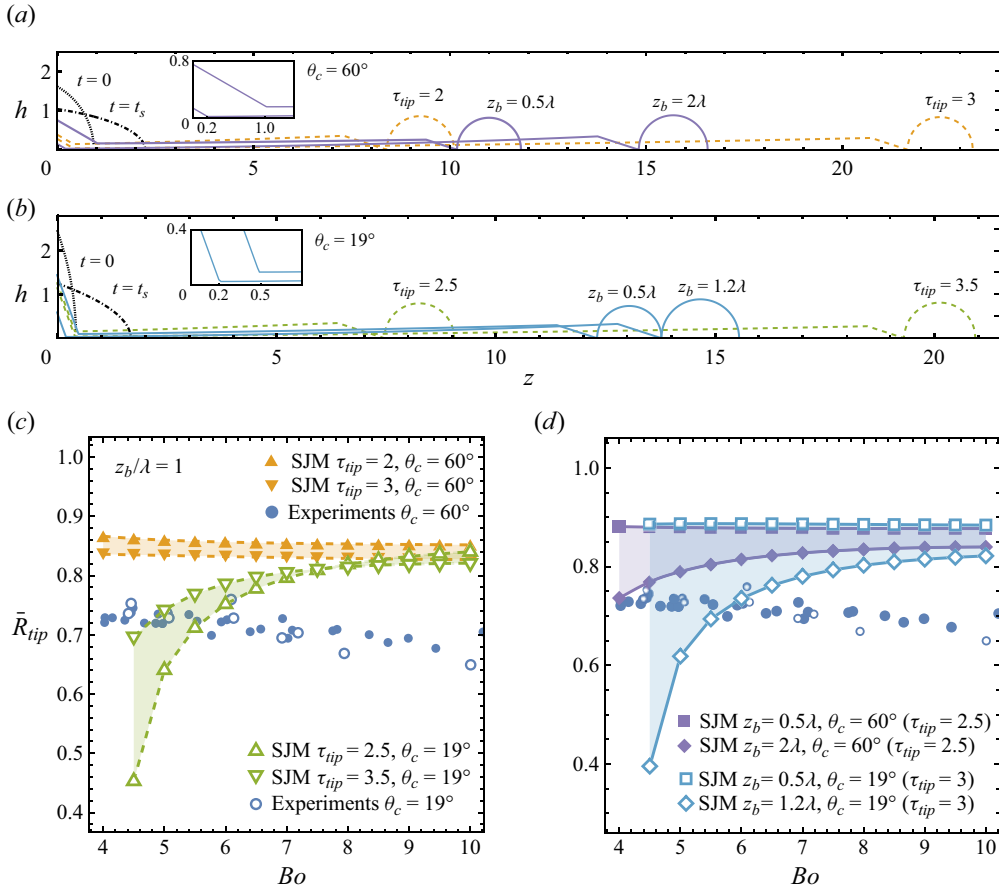


Figure 14. (a) *A priori* SJM lollipop solutions for $\theta_c = 60^\circ$ and $Bo = 6$ obtained using fixed $z_b = \lambda$, variable $\tau_{tip} = 2, 3$ (dashed lines) and fixed $\tau_{tip} = 2.5$, variable $z_b/\lambda = 0.5, 2$ (solid lines). The SJM initial condition \bar{h}_0 at $t = t_s = 1.5$ (dash-dotted) is the TFM solution [figure 24](#) originated from the initial value at $t = 0$ (dotted). The inset highlights the foot shapes due to the variable z_b solutions (solid). (b) Analogous results for $\theta_c = 19^\circ$ and $Bo = 6$: fixed $z_b = \lambda$, variable $\tau_{tip} = 2.5, 3.5$ (dashed lines) and fixed $\tau_{tip} = 3$, variable $z_b/\lambda = 0.5, 1.2$ (solid lines). (c) Range of R_{tip} solution of the lollipop system defined by $2 \leq \tau_{tip} \leq 3$ for $\theta_c = 60^\circ$ (region labelled by solid triangles), and by $2.5 \leq \tau_{tip} \leq 3.5$ for $\theta_c = 19^\circ$ (region labelled by empty triangles) as a function of increasing Bo . Here, $z_b/\lambda = 1$ is used for both θ_c . The τ_{tip} bounds are chosen here to match experimental observations made in [figure 5\(b\)](#). Experimentally measured values are given by filled/empty disks. (d) Similarly, range of R_{tip} due to $0.5 \leq z_b/\lambda \leq 2$ for fixed $\theta_c = 19^\circ$, and $0.5 \leq z_b/\lambda \leq 1.2$ for fixed $\theta_c = 60^\circ$. Also $\tau_{tip} = 2.5$ and 3 are used respectively for these two constant angles. Boundary values of z_b are labelled in the legends. It is established that the lollipop model R_{tip} consistently predicts a tip-drop radius $0.8 < R_{tip} < 0.9$ for large Bo and a wide range of system parameters τ_{tip} and z_b .

$z_b \cot \theta_c$, where we chose z_b to be of the same order as $\lambda = 1/\sqrt{Bo}$. Therefore as $Bo \rightarrow \infty$, $z_b \cot \theta_c$ decreases. However, for a fixed Bo , $z_b \cot \theta_c$ increases with decreasing θ_c . This also explains the apparent increasing trend of SJM results for $\theta_c = 19^\circ$ in [figure 14\(c,d\)](#), where the ratio z_b/λ is fixed while λ decreases with Bo . As a result, the volume of the base cone tends to overestimate the measured foot layer when Bo is small, therefore producing a smaller tip-drop prediction. Note further that the R_{tip} convergence observed in [figure 14](#) can similarly be explained recalling that $V_{jet} \rightarrow 4\pi/3, w_b \rightarrow 0$ as $z_b \rightarrow 0$ in (3.15), (3.16), thus dropping the dependence of the lollipop model on Bo .

3.5. Sensitivity of tip-drop size and pinch-off time on the dynamics of the free contact line

Combining experiments and simulations, we showed that the selection of the tip-drop size occurs essentially at the onset of curvature inflection of the interface prior to formation of the elongated ligament. In the limit of large Bo , our SJM lollipop asymptotic theory for primary tip-drop ejection (see § 3) provides leading-order estimates for the released drop size $R_{tip} \approx 0.8$, with 15 % error as seen in figure 5(a) mostly generated by the base-cone formulation (see (3.14)). We find a similar order of magnitude for the corresponding error, i.e. 15 %, in DNS (see § 2.3.2) and theory when assuming constant contact angle at the foot.

Yet, we have already seen (e.g. figure 6) that the foot angle is not constant over time. In fact, we consistently find (e.g. figure 29a,b) that as $t \rightarrow t_{tip}$, the apparent contact angle $\theta(t) \lesssim 60^\circ$ if $\theta(0) = \theta_c = 60^\circ$ and $\theta(t) > 19^\circ$ if $\theta(0) = \theta_c = 19^\circ$. Hence, maintaining a fixed θ_c as we did in both DNS (constant angle model) and SJM lollipop could induce an increasing error in the foot base-cone volume $V_b = \int_0^{z_b} \pi \tilde{h}_{base}^2 dz$, naturally inducing propagation of error in ligament volume and fluxes via V_{jet} in (3.15), and w_b in (3.16).

In this section and corresponding Appendices F and G, we revisit the experiments, theory and simulations to examine how a more refined contact-line dynamics at the foot may change the prediction error on R_{tip} . We approach this in two ways: (i) leveraging the experimental observations from the base-cone dynamics, we estimate the change in foot contact-line angle and evaluate how it would affect the R_{tip} prediction of the SJM lollipop. This is discussed in Appendix F; and (ii) introducing a DNS with a free angle (Appendix G) that allows us to resolve a time-varying contact line using the flow field extrapolated in the vicinity of the contact line and assessing the shift in R_{tip} and τ_{tip} . In all cases, accounting for the non-constant contact line shows a tendency for improved prediction of R_{tip} (DNS and SJM lollipop) and τ_{tip} (DNS).

First, from Appendix F, we confirm that the error on the foot base-cone volume, introduced by the moving contact line, propagates into the lollipop system through mass and momentum flux balance (3.22a) and (3.22b), respectively. It is interesting to note, however, that an error on the base volume of up to a factor of 4, in some cases, from the constant contact-line angle assumption (e.g. figure 31b), results in a 20 % error in the jet volume V_{jet} above $z > z_b$, and translates into a 10 % error in R_{tip} . This is because, as the tip breaking is approached, the measured volume fraction of the foot only accounts for less than 5 % of the total drop volume.

Second, from Appendix G, we introduce the modified DNS with a free angle which has two parts: (a) an extrapolated angle consistent with the flow at the grid scale and (b) a slip boundary condition. We summarize the implication in figure 15(a,b) which shows the comparison between the predictions of τ_{tip} and drop size R_{tip} , respectively, from various modelling assumptions with experiments. Interestingly, as with the asymptotic theory (see figure 14), although the DNS of constant contact angle captures τ_{tip} well and only over-predicts R_{tip} by $\approx 15\%$ and with a decreasing error as Bo increases, reaching $\approx 10\%$ in the high Bo limit, the DNS with free contact angle improves such predictions with: (i) a vanishing error in τ_{tip} ; and (ii) a decrease in the error on R_{tip} by about $\approx 5\%$ for $Bo \geq 4$.

3.6. Summary

In summary, by taking the infinite Bond number Bo and inviscid flow limit, we developed asymptotic theories for the accelerating drop's geometry of extreme aspect ratios L/R

Fragmentation from inertial detachment of a sessile droplet

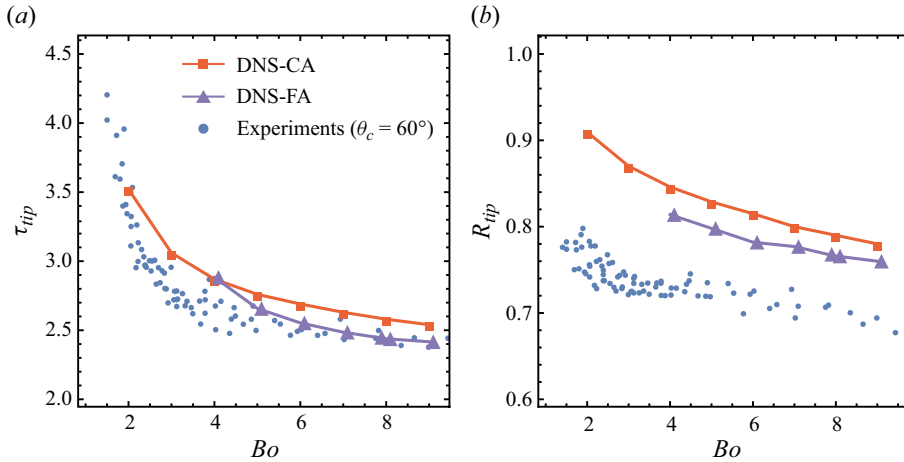


Figure 15. Comparisons of (a) the tip breakup time τ_{tip} and (b) the ejected drop radius R_{tip} between experiments (disks) and DNS results (lines) for $\theta_c = 60^\circ$ as a function of Bo . Both the constant and free-angle models (CA vs FA in the legend) are shown. All data for direct numerical simulation-constant angle (DNS-CA) correspond to the resolved slip length $\epsilon = 29.3 \mu\text{m}$ and $\epsilon/\Delta = 4$. We show that for both τ_{tip} and R_{tip} the simulations with the constant angle model reasonably capture the experimental measurements across all Bo with a slight overestimation of the order of $\approx 10\%$ at high Bo . Using a free contact angle model can reduce this error further down to $\approx 5\%$ for R_{tip} and essentially to zero for τ_{tip} .

that occur at different stages of the drop deformation. For small L/R at early times, the drop motion can be uniformly described by the TFM (with detailed discussion given in [Appendix B](#)), and when L/R becomes large the SJM (§ 3.3) starts to apply. Based on the SJM, we modelled the drop’s tip breakup using a lollipop system that incorporates surface tension effects using geometrical arguments (§ 3.3.3). With this combined modelling, we obtain robust predictions for the size of the ejected tip drop at high Bo , which match the experiments well. Moreover, these predictions are remarkably insensitive to uncertainties in the model parameters. Notably, the prediction is achieved without numerically solving the slender-jet equations. Instead, our treatment of the integrated equations over the lollipop domain allows an isolated approximation of the substrate contact effects. Therefore, we can assess directly the relative importance between the axial stretching due to acceleration and the interfacial effects near both the foot and tip region ends of the ligament, thereby shedding light on impulsive, asymmetric filament fragmentation.

The success of this framework, and its validation against simulations and experiments, establishes the following key novel findings about the drop elongation and fragmentation:

- (i) The initial drop motion is dominated by inertial acceleration (stage one), since it takes time for interfacial effects to manifest. We obtain as a result a universal drop dynamics in the limit $Bo \rightarrow \infty$. This early time drop dynamics is captured by (B11) in [Appendix B](#).
- (ii) As the drop extends axially, capillary effects grow dominant locally near the drop tip and foot, thereby affecting the shape in these regions where interface stress becomes comparable to inertia. At the foot, this necessarily creates a low-speed capillary boundary region immediately above the substrate. The thickness of this boundary region is empirically reflected by interface curvature inflection at the onset of

neck formation. We show that the height of this neck is of the order of the capillary wavelength in experiments (see figures 24 and 11). We also showed analytically that this neck, and its subsequent exponential thinning, are necessary consequences of flow continuity (see the derivation of (3.9)). Upon formation of a such neck that separates the extending drop into foot and top regions, we found that the volume of the eventual tip drop can already be predicted well by the volume of the top region at the time of necking onset, indicating an early onset of pinching dynamics dominated by surface tension that selects the tip-drop size.

- (iii) Above the foot layer, the liquid stretches into a ligament that is still acceleration dominated. Presently, without a detailed flow structure that matches the two asymptotic theories, we assume that the transition into the SJM occurs at time t_s and location z_b where necking begins. A free-fall regime thus follows, producing (3.11) that accurately captures the ligament shape away from its foot and tip. Therefore, we concluded that the liquid mass transported away from the foot layer through boundary flux is mostly absorbed by the free-falling ligament, not affecting its pinching tip. Meanwhile, the inertial acceleration, responsible for the ligament elongation during this time (stage two), plays an insignificant role in determining the tip-drop size.
- (iv) For the tip end, the capillary pinch-off mechanism ultimately leads to the release of a tip drop. We build this geometry into the lollipop structure that we propose, together with conical shapes for the foot layer and a connecting layer between the free-falling ligament and the tip sphere. By conserving mass, momentum and energy across the defined lollipop domains at an estimated breakup time τ_{tip} , we solve (3.22) and obtain an approximation of the breaking jet that predicts the ejecting tip size R_{tip} accurately. This confirms that, once necking initiates at the foot, the tip evolution gradually decouples from the foot contact dynamics, and becomes increasingly dominated by capillary end-pinching.
- (v) We performed a sensitivity analysis on the estimated parameters τ_{tip} and z_b and to the contact-line dynamics. These results are shown in figure 14 and show that our R_{tip} predictions are robust and insensitive to the uncertainty of the parameters when Bo increases. We also introduced a DNS with dynamic contact line to examine the error introduced by the static contact-line assumption, which helps reduce error prediction of the drop size by approximately 5%. We find that the robustness of the lollipop solutions suggests that the effects of the contact dynamics propagating through boundary fluxes entering the foot of the slender jet are in fact buffered by the free-fall regime. Hence, they do not significantly contribute to the local end-pinching process near the tip and do not significantly shift the size of the tip-drop selected, for the most part and within 15%, prior to the formation of the ligament.

4. Applications to pathogen transmission

Pathogens on contaminated surfaces, such as leaves, which motivated this initial investigation (Gilet & Bourouiba 2014, 2015, 2017) are typically responsible for new lesions on infected leaves and are typically trapped in a sticky mucilage. Upon rainfall or condensation, such mucilage is dissolved into sessile droplets on the infected/contaminated leaves/surfaces. Pathogens in such sessile droplets can include viruses, bacteria and spores, in increasing size range from $O(100 \text{ nm})$ (e.g. *Tomato spotted wilt virus*), to $O(1\text{--}10 \text{ }\mu\text{m})$ (e.g. *Xanthomonas citri subsp. citri* causative agent of citrus canker) to $O(10\text{--}100 \text{ }\mu\text{m})$ (e.g. *Septoria nodorum* causative agent of cereal rust). Such organisms by the virtue of

their different characteristic scales and composition differ in their sedimentation times. They also can differ greatly in their typical buoyancy and wetting properties. Spores, for example, are typically more hydrophobic and thus expected to gather at the interface of the sessile contaminated drop (e.g. Faulwetter 1917; Gregory, Guthrie & Bunce 1959; Gregory 1973; Fitt, McCartney & Walklate 1989; Paul *et al.* 2004; Bourouiba 2021*a*).

Having developed a comprehensive understanding of the drop inertial detachment and the validation of the numerical model against data and theoretical asymptotic predictions, we proceed in using the model to answer the following questions regarding contamination and transmission via inertial detachment: What fraction of pathogens would the tip primary daughter drop, and its following secondary smaller droplets, carry away from the contaminated sessile mother drop source? The corollary of that question is: How much initial pathogen remains on the contaminated substrate post-fragmentation? And how would such fraction change depending on the properties, for example wetting and buoyancy, of the pathogens involved?

Next, we discuss two illustrative examples to gain insight into the aforementioned questions: (i) the case of pathogen-mimic tracer that would be hydrophobic, such as spores, and so be concentrated on the interface of the sessile drop; and (ii) the case of pathogen-mimic tracer that would be wetting, with possible variation in the buoyancy or settling speed of the pathogen-mimic tracers, which would lead to possible stratification in their distribution in the sessile drop.

With access to the entire flow field in DNS, here, we examine trajectory of fluid parcels inside the drop from a Lagrangian perspective. We seed tracer particles, denoted as \mathbf{p} in the initial sessile drop according to predefined spatial distributions, and track each particle's movement as inertial detachment progresses by means of the velocity vector $d\mathbf{p}_i/dt = \mathbf{u}_{p_i}$. We first seed hydrophobic particles that would be concentrated on the sessile drop's interface. Figure 16(*a*) shows the evolution of the hydrophobic tracers. Clearly, most pathogens would be transported by the tip drop. Indeed, figure 16(*b*) confirms that, with a quantitative analysis of the fraction of pathogen in the tip drop vs foot vs middle ligament from which secondary droplets form (figure 16*a*), $\approx 5\% - 10\%$ of the original pathogens remaining in the secondary droplets emerge from the stretched middle ligament. This fraction increases as Bo increases. Interestingly, however, almost none remain at the foot. Thus, the inertial detachment can be thought of as a cleaning process for the contaminated surface in the case of these superhydrophobic pathogens. This is interestingly true for the full range of Bond numbers we examined, including the lowest ranges. Figure 17 shows the motion close to the foot and contact line for the example of $Bo = 1.5$ and suggests a lifting of the hydrophobic pathogens reminiscent of the rolling motion interfaces, for example observed in Dussan V. & Davis (1974).

In contrast to hydrophobic pathogens, we examine wetting pathogens and the effect of their distribution in various stratification layers of the sessile drop in figure 18. Note that we chose a layering such that the volume of the bottom blue region corresponds to the volume of the fluid left in the secondary ligament and the foot in the high Bo limit. We find that only the upper two layers of red and green tracers always end up in the ejected tip daughter droplet and that the lower blue tracer layer also enters the ejected tip drop when Bo is low. Another important conclusion from the simulations is that the layers roughly remain stratified throughout the drop deformation, supporting an extensional flow expected in the limit of large Bo , thus serving as further *post hoc* confirmation of our asymptotic 1-D theory in § 3.3. Hence, there is little to no mixing among stratified pathogens seeded in the initial sessile drop. An important implication of our results is that, for particles that are wetting and homogeneously distributed in the initial sessile drop, it is correct to

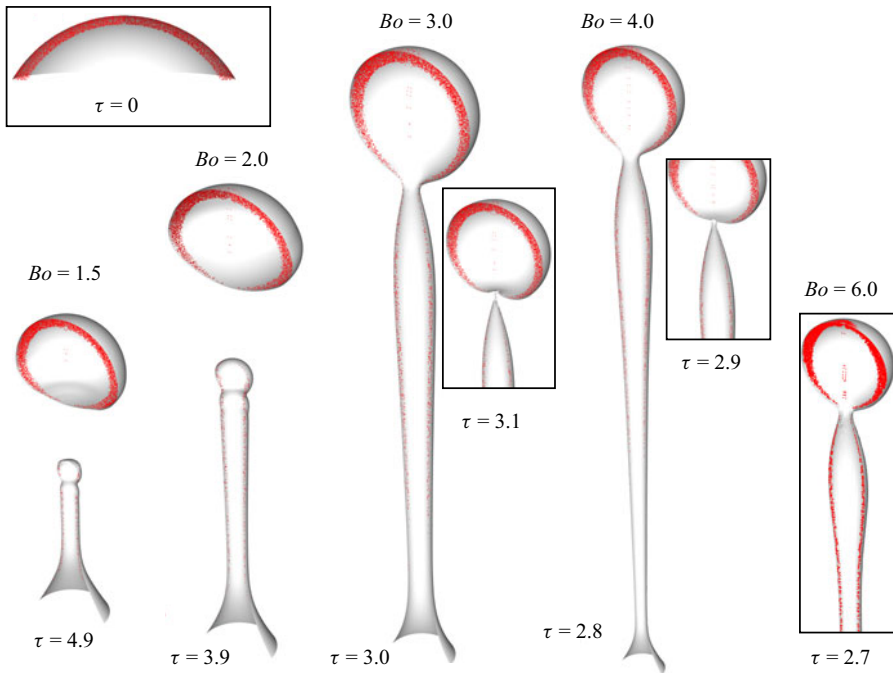


Figure 16. (a) Evolution of the hydrophobic VoF tracer particles for various Bond numbers. The simulations are full three-dimensional with no slip and constant, 60° , contact angle § 2.3.2, leveraging symmetry to compute only a quarter of the drop. The initial distribution of hydrophobic pathogens on the interface of the spherical cap is shown in the $\tau = 0$ image. (b) Corresponding concentration of the hydrophobic tracers in the tip drop, extensional ligament and the foot shown in (a). Interestingly, more than 90% of the tracer is carried in the tip drop and none remains in the foot for $Bo \geq 3$.

assume that the pathogen load ejected in the tip drop is proportional to the tip-drop volume. This insight serves as a good estimation for risk assessment, although it neglects polydispersity of pathogen/spore size and clustering of realistic spores/bacteria that may take place for some pathogen classes. These effects would affect the distribution and stratification of pathogens in the sessile mother drop and are the subject of follow-up investigation.

In conjunction with the tip and foot pinch-off, the extensional middle jet also undergoes fragmentation, resulting in the formation of a range of satellite droplets. Figure 19(a) shows examples of sequences of ligament breakup for a range of Bo . Note that, upon fragmentation of the extended ligament, occasional mergers occur, with a time-varying secondary droplet size distribution that eventually converges. We focus on the final droplet size after such mergers have concluded. Snapshots of fragments at the time of such conclusion are shown for example in figure 19(b). The quantification of the converged secondary droplet size distribution of the fragments with respect to their location is shown in figure 19(c) and their corresponding volume fraction contribution is given in (d). Notably, at higher Bo , for the no-slip DNS with a constant contact angle of 60° , not only does the tip daughter drop size approach a constant value of $R_{tip} = 0.78$, but the second largest daughter drop also converges to $R_2 = 0.6$. In fact, the entire droplet spectrum collapses onto a curve that is independent of Bo , when rescaled by the length of the ligament (and excluding the tip and foot size) (figure 20a). Figure 20(b) gives the corresponding droplet size spectrum.

Fragmentation from inertial detachment of a sessile droplet

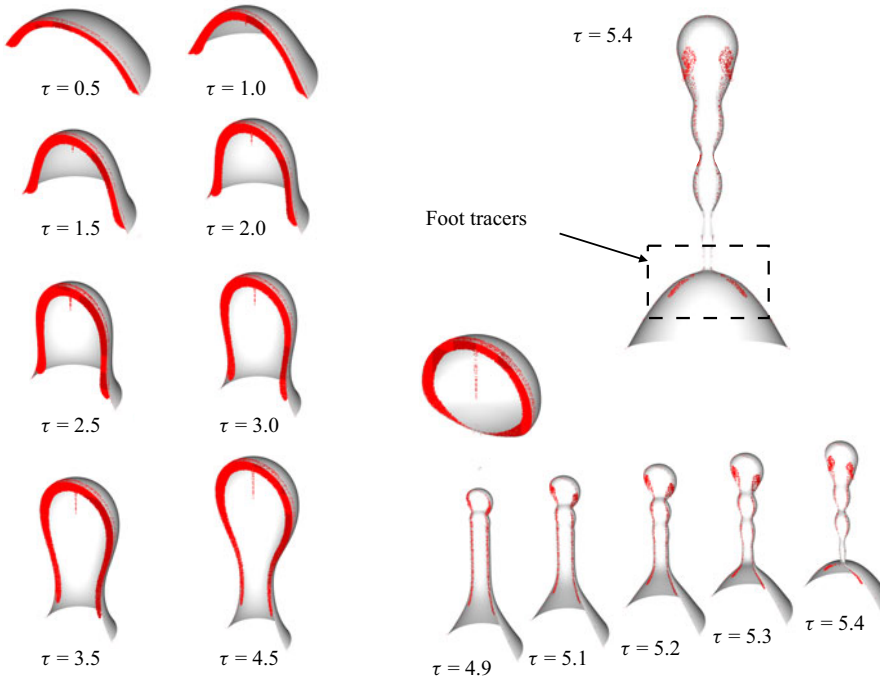


Figure 17. Sequence of images showing the hydrophobic tracer evolution for the low Bo example of $Bo = 1.5$. The hydrophobic pathogen analogue moves away from the contact line as the interface is deformed and the foot tracers end up near the top of the foot drop, with a decreasing fraction remaining in the foot as Bo increases (see figure 16*b*).

Finally, the range of pathogen transmission involves both the speed and size of the carrying pathogen-laden droplet (Bourouiba 2021*a*) and trajectories of ejected droplets are shaped by their initial Weber number. We estimate the Weber number of the primary tip daughter drop next. Informed by (3.6), the satellite droplets also have a distribution of ejection velocities depending on their sizes and pinch-off location. For the primary daughter tip drop, substituting the jet length approximation $\mathcal{L} \approx \tau_{tip}^2 \sqrt{Bo}$ discussed in § 3.2 into (3.24) gives the estimate $w_{tip} \sim \tau_{tip} \sqrt{2Bo}^{1/4}$, which is in agreement with the measurement range of $O(1 \text{ m s}^{-1})$ in our inertial detachment experiments (e.g. figure 8). As the ejected diameter is of the order of millimetres, this implies that the Weber number of the ejected tip daughter droplet is of $O(10^2)$. Figure 21 shows the speed of the ejected daughter tip drop, right at the instant of the pinch-off and the Weber number based on it as obtained in the DNS. The Weber number, We , shown takes into account three effects: the weak decrease of the radius of the ejected tip daughter drop with Bo ; the weak decrease of τ_{tip} with Bo ; and the strong increase of the ejected speed with Bo . From DNS, we see that this combination results in an approximately linear dependence of the speed, and associated We , of the ejected primary tip daughter drop on Bo .

5. Conclusions

We study inertial detachment via experiments where sessile liquid drops resting on substrates of different average wettability are impulsively exposed to a constant axial acceleration. Elongation of the drop follows, ultimately leading to a sequence of

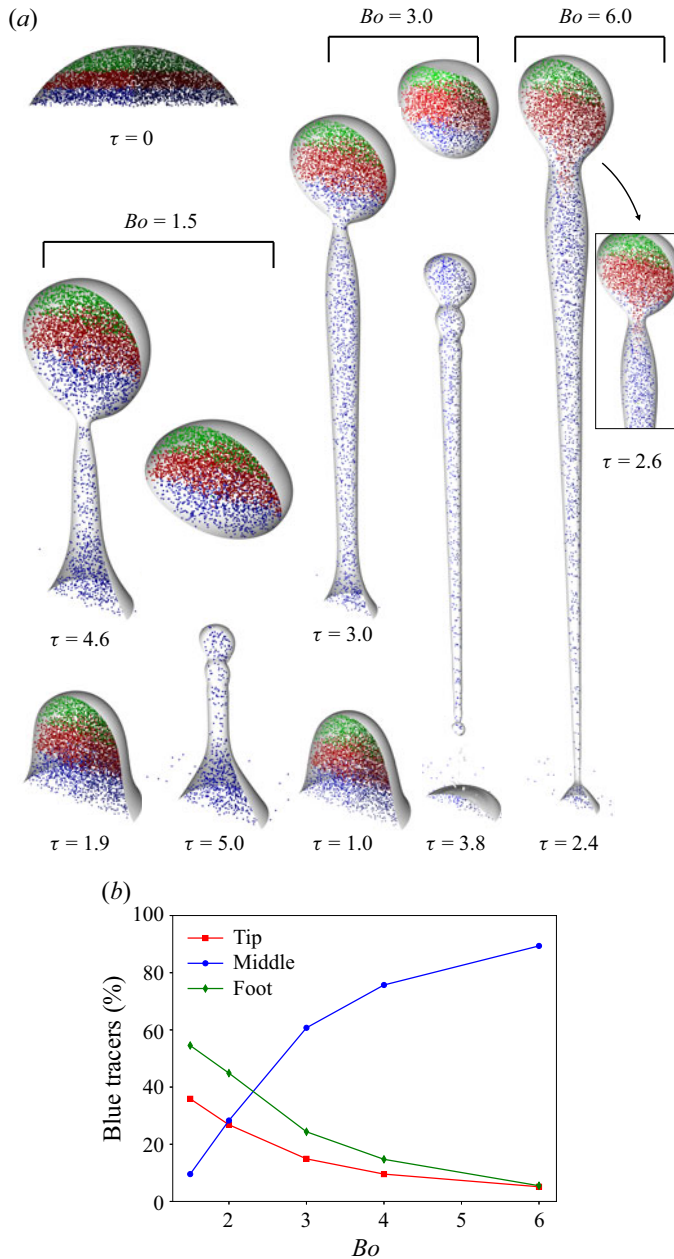


Figure 18. (a) Evolution of the stratified VoF tracked pathogen for various Bo . The simulations are full three-dimensional with no slip and constant, 60° , contact angle § 2.3.2. The initial distribution of the modelled pathogens of stratified wetting is shown in the $\tau = 0$ snapshot. Note that we chose a layering such that the height of the blue region corresponds to the volume of the fluid left in the secondary ligament and the foot in the high Bo limit. Interestingly, and consistent with the SJM, we confirm little mixing across layers. Moreover, as Bo increases, we find that the foot is increasingly depleted in favour of a larger fraction of pathogens in the ligament, consistent with a decrease of relative foot volume examine in figure 19(d). (b) The percentage distribution of the blue tracers corresponding to (a) the tip drop, the middle extensional ligament and the foot. The percentage represents the amount with respect to the initial blue tracer amount in the droplet. Consistent with our observation, we find more blue tracers in the extensional ligament than in the foot region and tip droplet. Remarkably, showing again that the inertial detachment is an effective cleaning mechanism, with little contamination remaining in the foot, i.e. on the surface, as Bo increases.

Fragmentation from inertial detachment of a sessile droplet

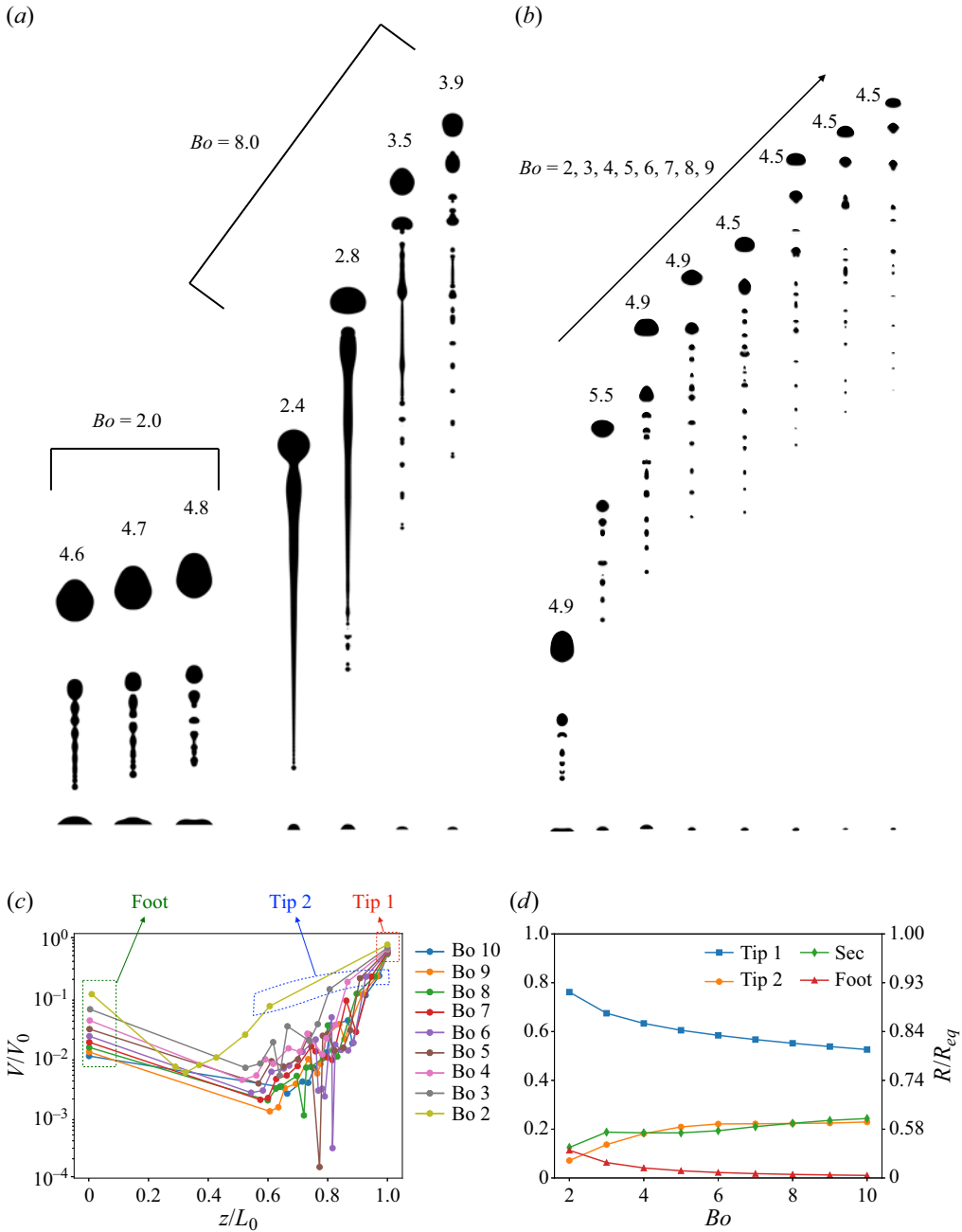


Figure 19. Sequence showing formation of satellite droplets in a range of Bo from axisymmetric simulations with no slip and constant contact angle 60° § 2.3.2 analogous to figures 16 and 18. (a) Evolution of the ligament for $Bo = 2$ and 8 . After the tip and foot pinch off, the extensional ligament fragments selecting a spectrum of droplet sizes. (b) Sequence showing the stage at which the secondary droplets reach their final size distribution for various Bo . Note that all snapshots have isometric scales, and some are scaled to fit the window. (c) Droplet volumes with respect to their position from the substrate, for $Bo = 2$ – 10 at the instant corresponding to (b). (d) Relative volume of the tip drop, second tip drop, secondary droplets excluding the second tip drop and the foot, as a function of Bo . As Bo increases the relative volume of all these fragments approaches constant values. Here, V_0 is the initial sessile drop volume and it is here also compared with the corresponding radius on the right-side twin axis, $R/R_{eq} = (V/V_0)^{1/3}$, revealing that the radius of the second tip daughter drop approaches a constant value of $0.6R_{eq}$.

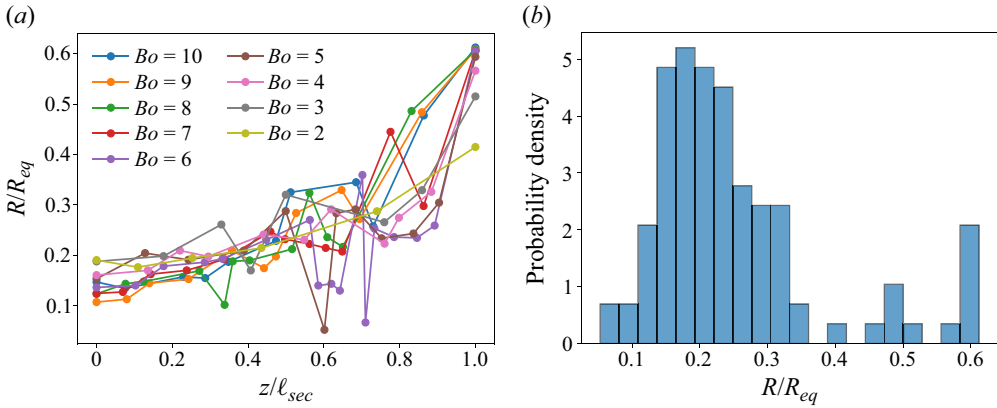


Figure 20. Secondary droplet sizes at the times shown in figure 19(b), upon convergence to a final distribution post-coalescence. These are shown normalized by the ligament equivalent length at breakup, l_{sec} for various Bo , enabling close collapse onto one curve for all Bo , with increase of droplet relative size with proximity to the tip drop. (b) The equivalent discrete probability density function of secondary droplet sizes, corresponding to the sizes shown in (a). Note that this figure focuses on the middle ligament and so excludes the tip-drop and foot regions (shown in volume fractions in figure 19).

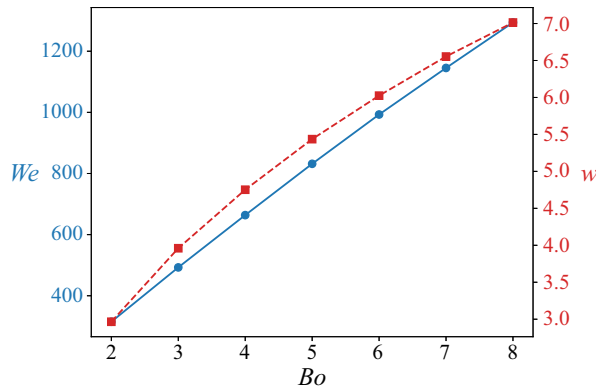


Figure 21. Example of ejected tip daughter drop speed, w , scaled by the inertial velocity (red) and associated Weber number, We , (blue) showing that both scale with Bo (blue). This example is based on the primary daughter droplet of the DNS with constant $\theta_c = 60^\circ$, with speed and size values taken at pinch-off time of the tip drop. Note that, in DNS, the ejected speed is calculated taking the average velocity over all the cells contained inside the droplet.

fragmentation events, as illustrated in figures 1 and 3. This phenomenon can be key in the transmission steps of infectious diseases. Although fragmentation of slender ligaments through Rayleigh-type instabilities or the end-pinching mechanism has been studied extensively in the past, the novelty of our problem lies in its geometrical asymmetry and a response to imposed forcing that is coupled with the solid–liquid contact dynamics at the substrate. This dynamics is particularly relevant for surfaces of intermediate wetting, which are ubiquitous and highly relevant to agricultural plants (Gilet & Bourouiba 2015, 2014; Bourouiba 2021a).

To gain a deeper understanding of end-pinching, we complemented experiments with the modelling of various components of the fragmentation and combining theory (asymptotics and a capillary-induced geometry constrained system) and numerics (multiphase Navier–Stokes DNS, VoF, *Basilisk*). The asymptotic theories in the infinite

Bo limit were based on small and large aspect ratios of the drop/ligament. For sessile drops, the thin-film approximation applies at small times, and consequently we obtained a potential flow solution, termed the TFM, that predicts a receding contact line that only depends on θ_c . The initial drop evolution given by TFM was validated by both DNS and experimental results. After the drop extends sufficiently into a ligament of slender aspect ratio, the 1-D SJM becomes valid while the TFM no longer is. As such, we derived a steady solution for a jet under free fall except in regions away from its two ends where significant capillarity applies. To compensate for the surface tension effects governing tip breakup, we then reformulated the slender-jet equations in weak form over a lollipop domain that approximates the ligament shape at the exact tip breakup time. This structure, shown in [figure 12](#), comprises a base cone, a free-falling jet, a spherical tip and a connecting cone in between. We solved the time-integrated algebraic SJM lollipop system for the breaking jet length \mathcal{L} , tip velocity w_{tip} and radius R_{tip} . The resulting theoretical predictions are robust and consistent with the experimental values, as well as the DNS, with agreement to within 10%–15% error in their R_{tip} predictions, compared with experiments ([figure 13](#)). More specifically, returning to our original motivating questions:

- (i) When does a sessile drop first detach from its supporting substrate under inertial forcing? And after fragmentation, what is the amount of the liquid content released?

For a large range of Bond numbers, the sessile drop fragments first near its tip, releasing a tip drop with radius close to 70% of the equivalent radius of the original mother sessile drop. This detachment occurs at a time that is approximately 2–3 times the capillary time reference. Our focus is on the primary daughter drop released from the extended ligament's free tip. Interestingly, we found that the radius of the ejected primary drop, R_{tip} , is nearly insensitive to the Bond number Bo , as long as $Bo \geq 2$. Moreover, the time of the primary drop ejection, τ_{tip} , is also insensitive to increasing Bo and equilibrium contact angle θ_c on the substrate ([figure 5](#)).

- (ii) What are the roles of the imposed inertial force, surface tension and surface wetting in the detachment process? And as the drop deforms, what are the dominant physical mechanisms that cause primary fragmentation?

The success of the lollipop approximation and DNS enabled a number of insights about the inertial detachment, as detailed in § 3.6. Mainly, we established that the drop elongation up to detachment can be separated into (a) an inertia-dominated initial stage when the sessile drop extends axially and recedes radially, and (b) a capillarity dominated end-pinching stage. The duration of the inertial stage is θ_c -dependent, a result of the substrate wetting property. Specifically, surface tension creates a capillary boundary layer of conical shape above the substrate, at the ligament foot and a spherical drop at the tip. The thickness of the foot layer is of the order of the capillary wavelength. We found that the initial inertia-dominated process selects the drop's shape and flow profiles which are inherited by the second stage. The second, capillarity-dominated stage, governs the end-pinching, ultimately producing the primary fragmentation of the tip drop. During this second stage, the role of inertial acceleration essentially reduces to generating an elongating and free-falling ligament between the foot layer and the tip drop. In this free-falling ligament, we find that a free-falling jet solution given by the infinite Bo limit is valid, where axial stretching leads to exponential thinning of the jet radius over time. Overall, given these imposed geometric constraints, we can leverage 1-D conservation laws (mass, momentum and energy) to predict a unique value of the final tip-drop size.

- (iii) How do these mechanisms determine the detachment time and the size of primary release?

The primary daughter drop selection and ejection is a surface-tension-dominated end-pinching mechanism initiated very early during the flow extension. It is also only weakly influenced by the ligament foot capillarity near the substrate. However, the selection of the size of the tip drop occurs early on in the sessile drop deformation and prior to formation of the slender ligament (second stage). In fact, the selection of the tip-drop size is determined, at leading order, at the end of the first (inertial) stage. Beyond this period, the inertial and substrate contact dynamics effects are absorbed by the elongating ligament and do not penetrate into the tip region where the second stage end-pinching mechanism driven by surface tension acts. Therefore, the total fragmentation time can be estimated by the sum of duration of these two stages.

Furthermore, we find the tip-drop size selection to be essentially concurrent with the very first development of a clear curvature inflection along the drop profile, which takes place in the early stage of the drop deformation, $\tau/\tau_{tip} \approx 0.2$ (see [figure 7](#)). Prior to the formation of a clear slender ligament, a fractional ligament emerges that spans, axially, the region from the inflection point to the free tip. The volume of such a nascent fractional ligament already reflects the equivalent radius of the final tip daughter drop, having a volume equivalent to R_{tip} within $\pm 15\%$. While the exact timing of this size selection can vary, at second order, with the wetting dynamics at the surface θ_c , we show that the variation only influences the prediction of R_{tip} to within 10% – 15% . Coincidentally, this early dynamics at $\tau/\tau_{tip} \approx 0.2$ is concurrent with the convergence of a final locked receding contact angle $\theta(t)$, $\theta \approx 40^\circ$. And this is true whether one starts from a surface with initial contact angles that are larger or smaller than 40° (here $\theta_c = 60^\circ$ and 19° , for example).

- (iv) What is the role of the solid–liquid contact-line dynamics in shaping the fragmentation of the primary drop?

We find that the solid–liquid contact dynamics dictates the development of the foot layer, thereby affecting the mass and momentum fluxes entering the tip. However, due to its relative small volume at moderate to high Bond numbers, the foot capillarity propagating through the elongating ligament has a lasting but very weak influence on the end-pinching dynamics.

We established the above with a sensitivity analysis that demonstrated that the R_{tip} predictions based on initial values provided by TFM are robust against parameter change, including the base-cone height and tip breakup time. Given our observation that the experimental contact angle substantially varies from the start to the end of the inertial fragmentation, we also evaluated the sensitivity of our predictions specifically to the details of the contact-line dynamics modelling. Using DNS validated against theory and experiments, we compared two formulations of the solid–liquid contact: a constant contact-angle model and a novel free-angle model that consists of a flow extrapolated grid-scale angle and a Navier slip length. We showed that the constant angle DNS is already capable of capturing the experimental observations to within 15% , and can be refined by the inclusion of the free-angle model (see [figure 15](#)), with a reduction of error down to 10% . Similarly, by varying the base-cone angle closer to the $\theta(t)$ measurements, we showed improvement in accuracy of the updated theoretical lollipop solutions.

- (v) Finally, returning to our original application of interest, and having validated our modelling of the inertial detachment end-pinching against experiments, what can we learn about the speed of ejection and distribution of organisms of various wetting

properties (e.g. hydrophobic spores vs wetting neutrally buoyant bacteria) in the ejected daughter drops?

Using our validated numerical model we showed the following: first, for hydrophobic pathogens, akin to spores that concentrate along the water–air interface, the majority of the hydrophobic pathogens are transported in the primary tip daughter drop. Second, for wetting pathogens, akin to most bacteria or viruses, which can vary in buoyancy and stratify, we find that the initial stratification of wetting pathogens in the sessile mother drop is mostly conserved. In other words, little mixing between settled wetting pathogens and buoyant ones would be expected for example.

In all wetting cases considered, we find that the inertial detachment is a remarkable cleaning process, with few to no pathogens remaining post-fragmentation on the substrate and the remaining foot liquid, even for small Bo just above one. We also examined how the speed and Weber number of ejection of the primary tip daughter drop vary with local substrate acceleration, via the Bond number, and found a close to linear increase, with ranges of We from 400 to 1200 for the range of Bo considered here from orders 2 to 10. Further examination of the consequence of such inertia transfer in the context of pathogen propagation is warranted.

Finally, we examined secondary atomization of the ligament below the primary tip drop, observing that the size of satellite droplets increases along the axial direction toward the tip drop, independent of Bo . We find that few to no hydrophobic pathogens are transported by these secondary droplets. However, in the case of wetting pathogens, the most negatively buoyant pathogens would be mostly transported by these secondary droplets. Absent cross-flow, and everything else being equal, the primary tip drop would have most inertia, in which case, our findings suggest that hydrophilic/wetting pathogens of various buoyancy values could be segregated in their transport by different drop sizes and speeds, while superhydrophobic pathogens would mostly be transported in the primary tip drop of maximum inertia.

Supplementary movies. Supplementary movies are available at <https://doi.org/10.1017/jfm.2024.874>.





Acknowledgements. We thank John Wang and Tristan Gilet for early conversations and explorations.

Funding. This research was supported, in part, by the USDA-NIFA Specialty Crop Research Initiative Grant Award no. MDW-2016-04938, the Richard and Susan Smith Family Foundation, the National Science Foundation, the Centers for Disease Control and Prevention-National Institute for Occupational Safety and Health and the National Institute of Allergy and Infectious Diseases of the National Institutes of Health under award number 5P01AI159402.

Declaration of interests. The authors report no conflict of interest.

Data availability statement. The data that support the findings of this study are available upon reasonable request.

Author ORCIDs.

-  N. Shen <https://orcid.org/0000-0002-0533-8081>;
-  Y. Kulkarni <https://orcid.org/0000-0001-6228-2865>;
-  S. Zaleski <https://orcid.org/0000-0003-2004-9090>;
-  L. Bourouiba <https://orcid.org/0000-0001-6025-457X>.

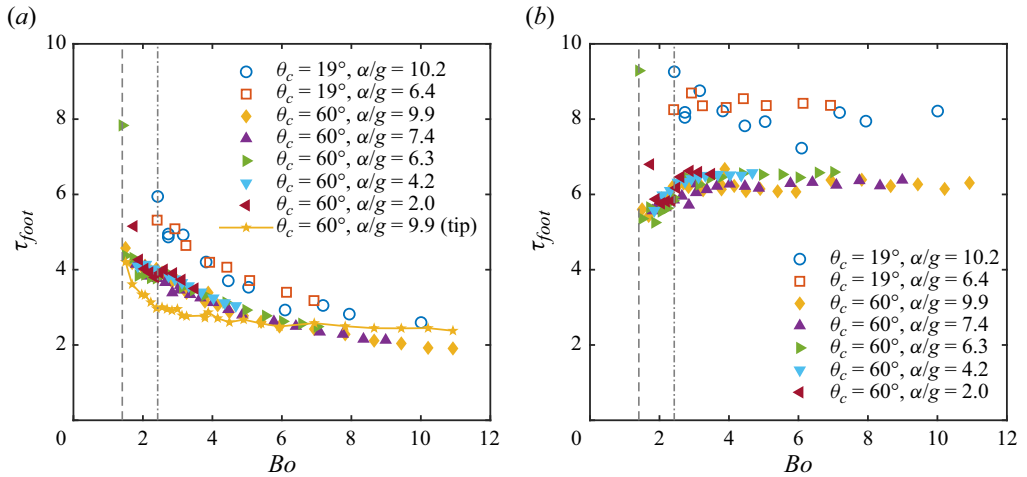


Figure 22. Ligament foot breakup times measured in (a) capillary and (b) inertial scaling. The τ_{foot} and t_{foot} results are given for increasing Bo and different $\theta_c, \alpha/g$ parameters. The legends are the same as figure 5 except that in (a) the τ_{tip} shown with stars is overlaid to demonstrate the switch in order of the tip and foot breaking times. Comparing (a,b), the constant value of τ_{foot} is dependent on the wetting dynamics of the foot, whereas t_{tip} collapses rapidly with Bo increase. This distinction confirms that, for a given wetting, the foot breakup is inertia dominated with second order wetting effect.

Appendix A. Foot breakup measurements

In this section, we present experimental measurements of the drop foot breakup time, in comparison with those given in figure 5 for the drop tip.

Similar to the tip dynamics, the breakup time of the ligament foot near the substrate (e.g. figure 3a iv) is also rapidly independent of Bo . However, here, at second order, the values of the constants toward which the tip breakup time converge have stronger dependence on the wetting dynamics on the substrate. We reveal this in the following manner: figure 22 shows τ_{foot} scaled with the capillary time scale compared with t_{foot} scaled with inertial time scale. Recall that the conversion between these two scales is given in (2.11a–c). This comparison reveals that τ_{foot} decreases weakly with Bo whereas t_{foot} converges rapidly to a θ_c -dependent constant as Bo increases: $t_{foot} \approx 6$ for $\theta_c = 60^\circ$ and $t_{foot} \approx 8$ for $\theta_c = 19^\circ$. Therefore, foot pinch off is an inertial process modulated by a local deformation geometry imposed by the acceleration.

The distinction between tip and foot breakups, governed by capillarity and inertial time scales, respectively, is also demonstrated in figure 22(a), where τ_{foot} is compared with the corresponding τ_{tip} given in figure 5(b) for $\theta_c = 60^\circ$ and $\alpha/g = 9.9$. We also note that the breakup time of the foot and the tip drop switch in order around $Bo = 6$: for $Bo < 6$, the foot neck breaks up earlier than that of the tip, while for $Bo > 6$, it is the tip-drop neck that breaks up earlier than that of the foot.

Appendix B. The thin-film model

In this section we derive the TFM presented in § 3.1 that reasonably captures the early dynamics of the sessile drops. We seek velocity components of 1-D spatial dependency, i.e. $u = u(r, t)$ and $w = w(z, t)$, such that $\nabla \times \mathbf{u} = 0$. The validity of this model when the drop is thin in the z -direction is discussed below.

B.1. Drop kinematics

The continuity equation (2.7a), together with the boundary condition $w(0, t) = 0$, gives the following 1-D velocity components:

$$u(r, t) = rF(t), \quad w(z, t) = -2zF(t), \tag{B1a,b}$$

where $F(t)$ is a function of time that can be identified from applying the kinematic condition (2.9) at $z = 0$. With the contact radius denoted $R(t) \equiv h(0, t)$ as shown in figure 2(b), we obtain

$$F(t) = \frac{\dot{R}(t)}{R(t)} = \frac{\dot{f}(t)}{f(t)}, \tag{B2}$$

where $R, \dot{R} = dR/dt$, and therefore normalized $f(t) \equiv R(t)/R(0), \dot{f} = df/dt$ are generally specified by a dynamic contact model. Substituting (B1a,b) into (2.9) then leads to a 1-D transport equation for the drop radius profile $h(z, t)$, which we solve by

$$h(z, t) = h_0 \left(zf(t)^2 \right) f(t), \tag{B3}$$

over the moving domain $0 \leq z \leq L(t)$. Here, $h_0(z) = h(z, 0^-)$ is the initial drop radius profile and $L(t)$ is the associated drop height, defined through $h(L, t) = 0$. By integrating $L = w(L, t)$ from (B1a,b) and initial length $L_0 = L(0)$, we obtain

$$L(t) = L_0 f(t)^{-2}. \tag{B4}$$

Because the drop is initially at rest ($u = w = 0$), evaluating (B1a,b) and (B2) at $t = 0^-$ gives the following initial values for f :

$$f(0) = 1, \quad \dot{f}(0) = 0. \tag{B5a,b}$$

Also for simplicity, we consider the initial drop radius profile h_0 given by the $G \rightarrow 0$ limit of (2.2), yielding a spherical cap of contact angle θ_c with

$$h_0(z) = R_0 \csc \theta_c \sqrt{1 - \left(\cos \theta_c + \frac{z \sin \theta_c}{R_0} \right)^2}, \quad L_0 = R_0 \tan \frac{\theta_c}{2}, \tag{B6a,b}$$

where $R_0 \equiv R(0)$ and θ_c are linked noting the drop initial non-dimensional volume $4\pi/3$ and

$$R_0 = 2 \left[(2 + \cos \theta_c) \sec^2 \frac{\theta_c}{2} \tan \frac{\theta_c}{2} \right]^{-1/3}. \tag{B7}$$

B.2. Drop dynamics

Next, following the potential flow assumption, the equation of boundary motion in (2.7b) is equivalent to the following unsteady Bernoulli equation for a dynamic boundary (Day et al. 1998):

$$\frac{\partial \phi}{\partial t} + \frac{1}{2} |\nabla \phi|^2 - z + \frac{\kappa}{Bo} = C(t), \tag{B8}$$

where κ is curvature, $C(t)$ is an arbitrary function of t and

$$\phi = \frac{ru(r, t)}{2} + \frac{zw(z, t)}{2}, \tag{B9}$$

such that $\mathbf{u} = \nabla \phi$ and $\nabla^2 \phi = 0$ linking u, w (B1a,b) to a potential ϕ . In the $Bo \rightarrow \infty$ limit, surface tension effects are neglected. Consequently, equating (B8) evaluated at

($z = L, r = 0$) (using (B4) and (B6a,b)) and any other boundary location (z, h) with $0 \leq z < L$ thus requires

$$\ddot{f} = \frac{d^2f}{dt^2} = \frac{6f^2 \left(zf^2 + R_0 \tan \frac{\theta_c}{2} \right) - 2f^4}{f \left[R_0 (f^6 - 2) \cot \theta_c + (f^6 + 2) (zf^2 + R_0 \csc \theta_c) \right]}, \quad (\text{B10})$$

where the substitutions (B9), (B1a,b), (B2) and (B3) are used. It appears in (B10) that \ddot{f} , parameterized by θ_c , depends on the location z where (B8) is enforced, which is a condition inconsistent with the 1-D velocity ansatz (B1a,b). However, for $z < L \ll 1$, we can expand (B10) asymptotically as

$$\ddot{f}(t; \theta_c) = \frac{\sin \theta_c \left[6R_0 \tan \left(\frac{\theta_c}{2} \right) f^2 - 2f^4 \right]}{R_0 \left[(\cos \theta_c + 1)f^6 - 2 \cos \theta_c + 2 \right] f} + O(L), \quad (\text{B11})$$

where $R_0(\theta_c)$ is given by (B7). The leading order of (B11), together with its initial values (B5a,b), yields an ODE for $f(t)$ that can be solved numerically independent of z . With $f(t)$ determined, we obtain the 2-D potential flow field in (B1a,b) and the evolution of the drop shape in (B3) as solutions compatible with the Bernoulli equation (B8) in the large Bo limit. Additionally, a dynamic description for the contact radius R_0 automatically follows from (B2). We note that a more realistic contact-line dynamics dependent on the substrate material properties cannot enter here because all surface tension effects are dropped in the strict limit of $Bo \rightarrow \infty$. We term this theory the TFM because of its root in the small limit L expansion (B11). We expect the TFM to be valid only for early times $t \ll 1$ when the inertia dominated potential flow assumption is expected to be reasonable. In this early-time limit, we predict the initial drop elongation speed given by (B1a,b) and (B4) as follows:

$$w(L, t) \sim -2L_0 \ddot{f}(0)t \sim \frac{8 \sin^2(\theta_c/2)}{3 - \cos \theta_c} t, \quad (\text{B12})$$

where (B4), (B5a,b), (B7) and (B11) are used. Scaling both w and t using capillary reference given by (2.11a–c) shows that $w/\sqrt{Bo} \sim K(\theta_c)\tau$, with $K(\theta_c) = 8 \sin^2(\theta_c/2)/(3 - \cos \theta_c)$ being the same acceleration constant found in (B12).

B.3. Results and validation of TFM

Solutions to (B11), and therefore the flow velocity (B1a,b) and drop shape (B3), for different initial contact angles θ_c are obtained using a variable time-step fourth-order Runge–Kutta scheme. Figure 23(a) shows the normalized contact radius $f(t)$ for increasing $\theta_c = 10^\circ, 20^\circ, 40^\circ, 60^\circ$. Receding contact lines are established since $f(t)$ monotonically decreases in all cases. And the rate of recession appears to converge rapidly as θ_c increases. Correspondingly, the velocity time dependency $F(t)$ is given in figure 23(b), where similar converging curves are found. Importantly, $|F(t)|$ has a non-monotonic evolution: it first increases for a finite period of time and then decays, meaning that, as the drop elongates in the z -direction, its axial velocity w , given by (B1a,b), stops growing and starts decreasing at one point. The transition to a decreasing trend occurs at times that are smaller as θ_c increases (figure 23b). Since TFM is obtained for $Bo \rightarrow \infty$ where the imposed inertial acceleration dominates, a decreasing w is unphysical in this limit, indicating that the TFM solution fails beyond $|F(t)|$ peaks.

Fragmentation from inertial detachment of a sessile droplet

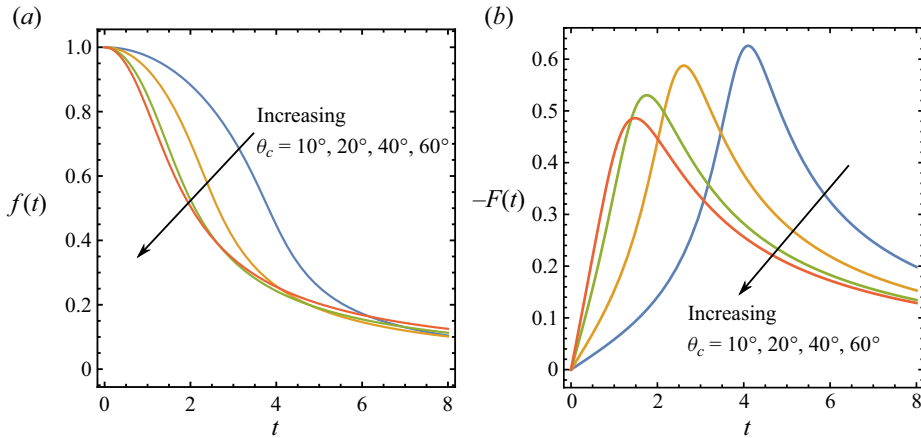


Figure 23. Numerical solutions for $f(t)$ and $F(t)$ obtained from (B11) using $\theta_c = 10^\circ, 20^\circ, 40^\circ, 60^\circ$ in (a,b), respectively. Here, $f(t)$ gives recession of the contact radius and $-F(t)$ shows the velocity temporal profile. Both results appear to converge as the contact angle θ_c increases. The TFM fails for times beyond the peak of $|F(t)|$ because the velocity decay is incompatible with the infinite Bo assumption. The decay occurs at times that are decreasing with increasing θ_c as seen in (b).

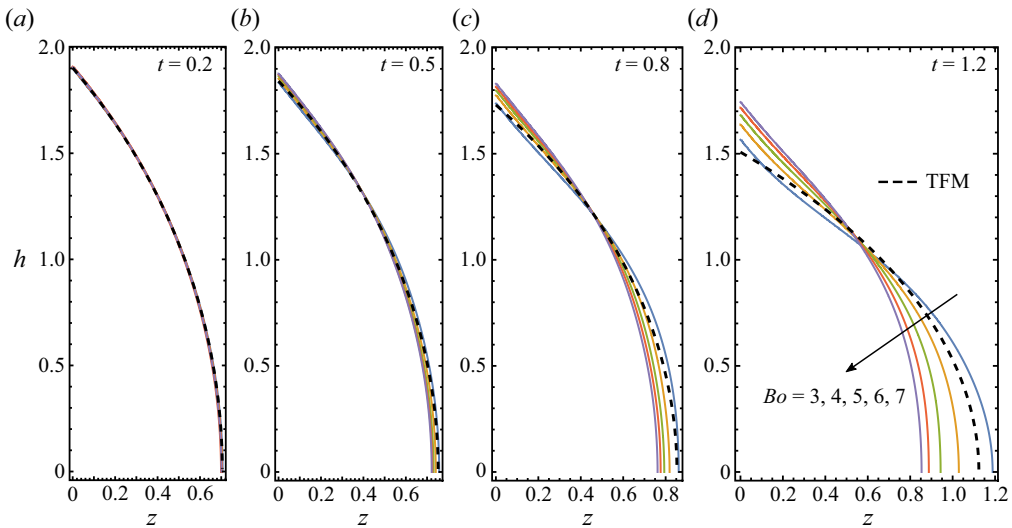


Figure 24. Successive drop radius profiles $h(z, t)$ with axial z -axis plotted horizontally. Time increases from $t = 0.2$ to $t = 1.2$ in (a–d). The DNS results obtained for a moderate $\theta_c = 40^\circ$ with $3 \leq Bo \leq 7$ are given by solid lines, and the TFM predictions are shown in dashed lines. The drop shapes collapse for all Bo at early times (a,b), and are correctly captured by the TFM. As elongation continues, numerical profiles for different Bo increasingly diverge from each other, with emerging curvature inflection along the ligament boundary, which is missed by the TFM which does not account for surface tension effects (c,d).

In figure 24, we validate the TFM by comparing its predictions for the evolving drop radius profile $h(z, t)$ against DNS. The numerical results are obtained using a constant contact angle model of moderate $\theta_c = 40^\circ$, and increasing $3 \leq Bo \leq 7$. Figure 24(a,b) shows that, for small times, drops deform in a universal manner for all Bo , and this is well captured by the TFM theory. As drops extend with higher aspect ratios $L/R \gtrsim O(1)$, the effects of finite Bo increasingly manifest in the simulations. Different ligament profiles

develop for different Bo values and the drop profile develops inflection in curvature (figure 24*c,d*), similar to what we observed experimentally in § 2.4.5. In fact, lacking surface tension, the validity of the TFM asymptotic model deteriorates: it is naturally incapable of recovering these surface-tension-induced features. Note that Bo is varied in DNS by changing α/g while fixing G , and therefore the inertial time units differ between Bo (see (2.10*a-c*)). Therefore, a convergence of DNS results of increasing Bo towards the TFM limit in figure 24(*c,d*) is not expected. Instead, because $t = \sqrt{Bo}\tau$, drop shapes captured by increasing Bo at a fixed t correspond to earlier stages of the evolution in capillary units, retarding curvature inflection.

Appendix C. Dimensional analysis of the foot layer

In this section we give similarity arguments for the size and shape of the conical foot layer modelled in § 3.3. We begin with the key assumption that, after the separation of a foot layer ($0 < z < z_b$) and an extending jet ($z_b < z < L$), as seen experimentally in figure 7 and numerically in figure 24, the foot layer follows a self-similar solution under inertial scaling in the $Bo \rightarrow \infty$ and $Re \rightarrow \infty$ limits. In this regime, the imposed acceleration is expected to dominate surface tension and viscous stress throughout the foot layer, as the latter forces remain small in such developed region. We further hypothesize a critical time of singularity, expressed using dimensional variables as

$$t_c = c\sqrt{\frac{R_0}{\alpha}}, \tag{C1}$$

when a similarity solution collapses. Here, R_0 is the initial contact radius (B7), α is the effective acceleration (2.5) and c is an unknown dimensionless constant. Denoting the shifted time $s = t_c - t$, the contact radius $R = h(0, t)$ therefore must scale as

$$R = R(s) = c_0\alpha s^2, \tag{C2}$$

with constant c_0 . Similarly, the radial profile of the foot layer height $y(r, s)$, defined through $h(y(r, s), t) = r$, scales as

$$y(r, s) = \alpha s^2 \varphi(x), \quad x = \frac{r}{\alpha s^2}, \tag{C3}$$

where $\varphi(x)$ is a dimensionless shape function of similarity variable x . Note that, by definition, $\varphi(R\alpha^{-1}s^{-2}) = 0$. Also using (C2) and (C3), the dynamic contact angle θ immediately follows as

$$-\tan^{-1} \theta = \lim_{r \rightarrow R} \frac{\partial y}{\partial r} = \varphi' \left(\frac{R}{\alpha s^2} \right) = \varphi'(c_0), \tag{C4}$$

suggesting that θ is independent of time. This is consistent with the experimental observation made in figure 6(*b*) where θ locks, taking an approximately constant receding angle value, as foot breaking is approached. In other words, we showed that the condition of inertia dominance leads to (C4). However, whether or not the implication of constant contact angle necessarily depends on such condition remains an open question.

Further, the thickness of the foot layer z_b and the corresponding neck radius h_s in this inertial regime can be scaled respectively as

$$z_b = y(h_s, s) = c_1\alpha s^2, \quad h_s = h(z_b, t) = c_2\alpha s^2, \tag{C5}$$

where c_1 and c_2 are again constants. Based on the free-fall solution for the extending jet immediately above the foot layer (see § 3.3.2), it is possible to estimate the constants using

the dimensional form of (3.8)

$$\partial_t h + \frac{h}{2} \sqrt{\frac{\alpha}{2z}} = 0. \quad (\text{C6})$$

Substituting (C5) into (C6) thus gives $c_1 = 1/32$, and as result of evaluating (C3) at the neck point where the slope of y diverges, the shape function φ must satisfy

$$\varphi(c_2) = c_1, \quad \varphi'(c_2) = \infty. \quad (\text{C7a,b})$$

Together with (C4), $\varphi(x)$ is therefore expected to be a compact and monotonically decreasing function of x . To estimate the overall size of such a roughly conical foot layer, we assume that (C2) and (C5) apply over s that matches capillary time scale, i.e. $s \sim \sqrt{\rho z_b^3 / \sigma}$. This yields

$$R \sim z_b \sim \sqrt{\frac{\sigma}{\rho\alpha}} = \Lambda, \quad (\text{C8})$$

where Λ is the capillary wavelength defined in (2.10a–c). Correspondingly, the dimensionless results, $R/R_0 \sim z_b \sim 1/\sqrt{Bo}$ up to foot breaking, again, agree with the observations made in figure 6, and justify the empirical choice for z_b made for the SJM lollipop model in § 3.3.3.

Appendix D. Velocity profile properties for the lollipop model

In this section we discuss some elements of the axial velocity profile w specified for the lollipop model (3.21a,b). Particularly, the significance of the boundary velocity w_b for conserving volume in (3.22a) and the insignificance of the cone velocity w_c for computing energy in (3.22a) are demonstrated.

D.1. Volume adjusted boundary velocity

To give an example with $\theta_c = 60^\circ$ and $Bo = 7$, figure 25(a) compares the volume adjusted velocity $w_b(\tilde{t})$ given in (3.16) with the steady, free-fall solution (3.6) evaluated $z = z_b = \lambda$, where the foot layer boundary is chosen at one capillary wavelength. As a result, the slender-jet volume, calculated using (3.15) and (3.11) as $V_f = \int_{z \geq \lambda} \pi \tilde{h}_{free-fall}^2 dz$, is shown in figure 25(b) as a function of time \tilde{t} up to tip breaking. For comparison, the corresponding DNS result of constant contact angle is also given. Clearly, the DNS data are overestimated by V_f , generated by the constant mass flux through $z = \lambda$; whereas V_{jet} agrees with the simulation better, except near $\tilde{t} = 0$ where an error is introduced by the base-cone assumption. Therefore, w_b is the preferred choice for mass and momentum calculations at tip breaking in (3.22) to improve the accuracy of the lollipop structure.

D.2. Energy equation simplification

Here, we derive the analytical result given in (3.24), and evaluate its associated error. First, expanding $E(\tilde{t}_{tip})$ in the lollipop energy equation (3.22c) and substituting (3.21a,b) gives

$$E(t_{ip}) = E_c + \frac{4\pi R_{tip}^2}{3} \left(\frac{w_{tip}^2}{2} - (\mathcal{L} - R_{tip}) \right) = I_\phi, \quad (\text{D1})$$

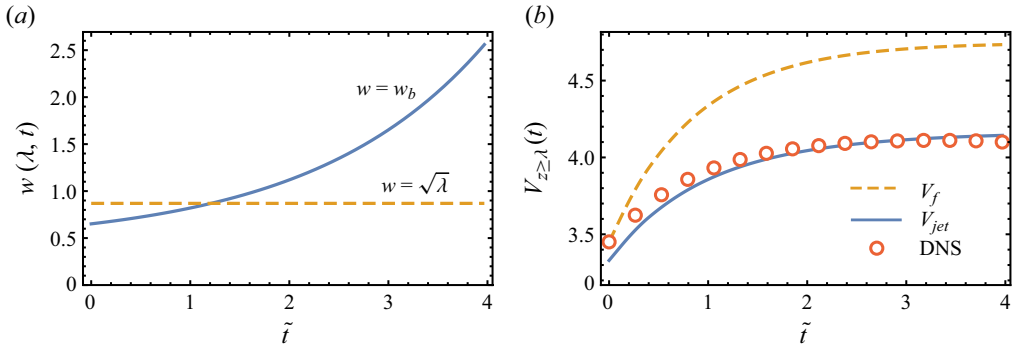


Figure 25. (a) Comparing w_b in (3.16) with $w = \sqrt{\lambda}$ in (3.6) at the critical boundary chosen at $z = z_b = \lambda$ for $\theta_c = 60^\circ$ and $Bo = 7$. (b) Drop volume in the slender-jet domain $V_{z \geq \lambda}$ given by V_f , the free-fall solution in (3.11) (dashed), V_{jet} in (3.15) (solid) and DNS (circles).

where

$$E_c = \pi \int_{z_c}^{\mathcal{L} - 2R_{tip}} \left(\frac{w_c^2}{2} - z \right) h_{cone}^2 dz, \quad I_\phi = \pi \int_0^{\tilde{t}_{tip}} \left[\left(\frac{w_b^2}{2} - z \right) \tilde{h}_b^2 w_b \right] d\tilde{t}, \quad (D2a,b)$$

are the net mechanical energy of the connecting cone and the time-integrated energy flux into the jet ($z \geq z_b$), respectively. It is immediately observed that substituting w_c from (3.20) into E_c leads to divergent kinetic energy of the cone, $\pi/2 \int w_c^2 h_{cone}^2 dz$, if $\delta = 0$ is taken. Clearly, this is an artefact of the steady cone assumption that leads to (3.20), since, although w is observed to increase approaching the tip neck in simulations (see figure 10a,c), the rise is moderate, and because h decreases near the neck region E_c must remain finite. Also, this issue does not exist for the momentum equation (3.22b) because $w_c h_{cone}$ is constant throughout the cone. Nevertheless, extending the steady free-fall velocity profile (3.6) into the cone region ($z_c \leq z \leq \mathcal{L} - 2R_{tip}$) as well as the jet boundary ($z = z_b$), i.e. substituting $w = \sqrt{2z}$ for w_c and w_b in (D2a,b), yields

$$E_c = I_\phi = 0, \quad (D3)$$

and thus (D1) produces the desired result, (3.24). Hence, (D1) implies that the kinetic and potential energies of the breaking tip have the same magnitude but opposite signs, so that its net mechanical energy is zero. We demonstrate next that the error associated with such a simplification, caused by non-zero E_c and I_ϕ , is realistically small.

First, we consider the relative magnitude of I_ϕ , obtained using (3.16), compared with the tip drop's kinetic energy, $E_k = 2\pi R_{tip}^3 w_{tip}^2 / 3$, according to the lollipop model. It follows from the approximation (3.24) that the ratio $I_\phi / E_k \sim O(\tilde{h}_b^2 / \mathcal{L})$ for large \mathcal{L} and small \tilde{h}_b . Therefore, based on the SJM premise, the contribution of this non-zero energy flux to the final solution of \mathcal{L} in the lollipop model must be small. Similarly, for the connecting cone, provided that deviation of w_c from the steady profile (3.6) remains finite, as we observe from the simulations in figure 10, it is expected that $E_c / E_k \sim o(h_{cone} / \mathcal{L})$. Together, (D3) gives a reasonable approximation, not significantly affecting the tip-drop size prediction.

Further, numerical evidence is shown in figure 26, where figure 26(a) compares I_ϕ , obtained using (3.16) with E_k computed from the solution of the lollipop system (3.22), and for $\theta_c = 60^\circ$, with results shown as a function of different t_{tip} estimates and Bo . Across a sufficiently large range of t_{tip} and Bo we find that $I_\phi / E_k \lesssim O(0.01)$, decreasing with

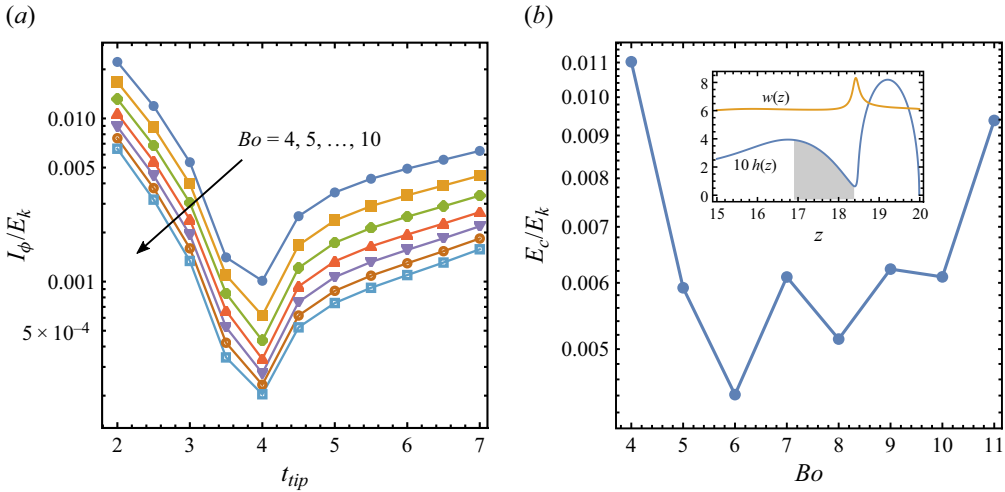


Figure 26. Relative size of (a) the integrated energy flux I_ϕ and (b) the net mechanical energy of a connecting cone E_c (see (D2a,b)), compared with the kinetic energy of the breaking tip drop E_k . In (a), I_ϕ and E_k are calculated using the lollipop system (3.22), where \tilde{h}_0 is taken from the TFM solution and $z_c = \lambda$, as discussed in § 3.4.2. In (b), the DNS results for $w|_{r=0}$ and h are used to evaluate E_c/E_k numerically. The inset gives an example for $Bo = 7$ of the analogous cone domain (shaded) and the w, h profiles, with tenfold amplification for h to visualize locations of the neck and velocity bump. Together, these results demonstrate that the error incurred from the assumption of $I_\phi = E_c = 0$ is small for the purpose of determining \mathcal{L} and R_{ext} using the lollipop model. Thus, (3.24) is an accurate approximation.

Bo and becoming orders smaller near the simulated and experimental $t_{tip} \approx 4$. Similarly, figure 26(b) addresses the potential issue of divergent E_c . The central axial velocity w and drop shape h from DNS using constant $\theta_c = 60^\circ$ are used to evaluate E_c given by (D2a,b) numerically at $t = t_{tip}$ for a range of Bo . An example of the integral domain (shaded), as well as the h, w profiles are given in the figure 26(b) inset for $Bo = 7$. There, the shaded area serves as a proxy for the connecting cone in the lollipop model; E_k of the ejecting tip in this case is obtained by the numerical integral $E_k = \pi/2 \int w^2 h^2 dz$. Again, the resulting energy ratio E_c/E_k is smaller than 1% across all Bo considered, suggesting that the net mechanical energy of the cone is realistically negligible compared with what the lollipop model is designed to estimate, e.g. the magnitude of energy components, kinetic or potential, of the breaking drop. And thus the simplifications of (D3) are justified.

Appendix E. Direct numerical simulation convergence and volume conservation

Numerical convergence for the tip pinch-off time and the volume of the ejected tip droplet is shown in figure 27. We see that second-order convergence is reached for the pinch-off time and first-order convergence is seen for the ejected tip volume. All the axisymmetric results presented throughout the paper are done with a resolution of 409.6 grid points per initial radius, except for the sensitivity analysis shown here in figure 27. It is clear that the numerical scheme conserves volume with high accuracy throughout the evolution of the drop (figure 28).

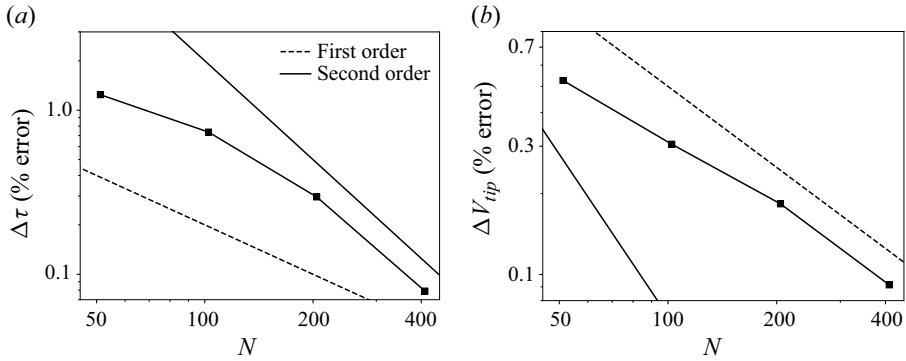


Figure 27. Convergence study of the DNS for the $\theta_c = 60^\circ$ case. The y-axis shows the percentage error $\alpha - \alpha_{ref}/\alpha_{ref} \times 100$ for the (a) tip pinch-off time and the (b) volume of the ejected tip daughter drop. Second-order convergence is reached for (a) while (b) shows first-order convergence. Here, N gives the number of grid points per initial radius. This figure shows results for $Bo = 4.0$ with the reference solution corresponding to 819.2 grid points per initial radius, that is, $R/\Delta = 819.2$.

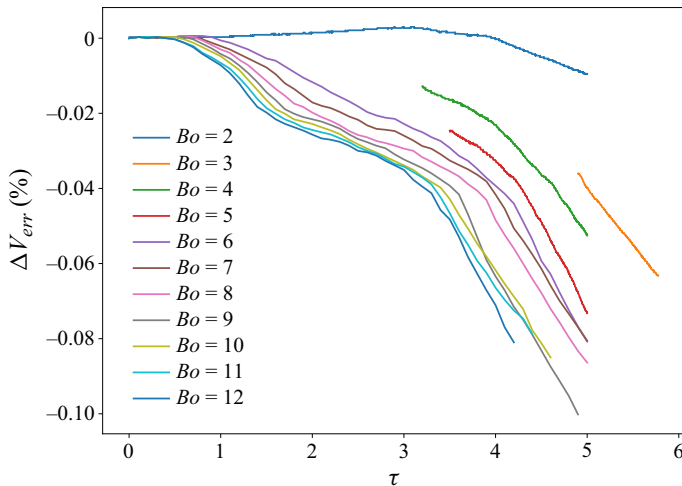


Figure 28. Evolution of the percentage error in volume $\Delta V_{err}(\%) = (V(\tau) - V_0)/V_0 \times 100$ for DNS-CA. Here, $V(\tau)$ represents the total liquid volume at a given time τ , that is, the sum of all the liquid volume including the atomized drop and deformed liquid structure, and V_0 is the initial drop volume. The data in the plot include the time selected to showcase data in figures 19 and 20. This implies that the data of figures 19 and 20 conserve at least 99.9% of the initial volume.

Appendix F. Base-cone error estimation for SJM theory

As discussed in § 3.5, we assess the error of the SJM prediction with respect to the base-cone dynamics. To do so, we focus on the ligament foot region in figure 29(a,b), where close-up views correspond to figure 13(b) in the range $z \in [0, z_b]$ for $\theta_c = 60^\circ, 19^\circ$, respectively, are given at three different instants from $\tilde{t} = 0$ to \tilde{t}_{tip} . In both θ_c cases, two observations are made: (i) the evolution of the slender-jet boundary radius $h|_{z=z_b}$ is approximated by \tilde{h}_b in (3.9) to an acceptable error; (ii) however, this error is amplified if the constant equilibrium contact-angle assumption breaks down over time.

To further demonstrate the change in R_{tip} predictions upon accounting of the change in contact angle, θ_c , figure 29(c) shows R_{tip} solutions to the lollipop system (3.22) when

Fragmentation from inertial detachment of a sessile droplet

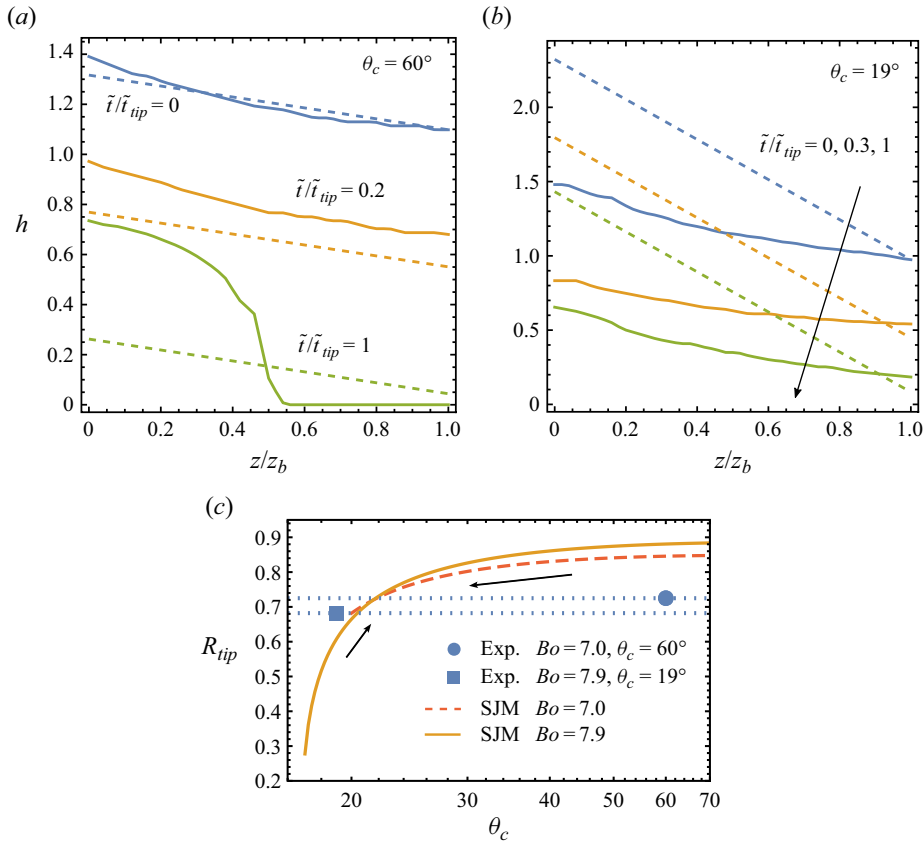


Figure 29. (a) Zoomed-in view of the ligament feet in the range $0 \leq z \leq z_b$ that corresponds to the experiment specified in figure 13(b), where $\theta_c = 60^\circ$. Foot shapes at three different times $\tilde{t}/\tilde{t}_{tip} = 0, 0.2, 1$ are given by the solid lines, while the lollipop base-cone model \tilde{h}_{base} at the same instants is shown by dashed lines. (b) Analogous results for the second experiment given in figure 13(b) where $\theta_c = 19^\circ$. In the first case (a), the foot contact angle appears to be less than 60° for $\tilde{t} > 0$ and therefore V_{exp} is underestimated by V_b . Contrarily, in the second case (b), the angle is measured to be greater than 19° , causing an overestimation of V_{exp} . Note that \tilde{t} defined in (3.7a–c) is the SJM initialization time, therefore it is possible that at $\tilde{t} = 0$ the base-cone assumption is no longer strictly correct. Panel (c) shows the R_{tip} solutions generated by the SJM lollipop system (3.22) with varying θ_c for the base cone (3.14). Two cases are shown using a solid line for $Bo = 7$ and a dashed line for $Bo = 7.9$. The corresponding initial \tilde{h}_0 in (3.7a–c) is taken from measurements at $t_s/t_{tip} = 0.2$ and 0.35 for $Bo = 7$ and $Bo = 7.9$, respectively. Also, $z_c = \lambda$ is used in both cases. The experimental R_{tip} values are labelled with solid markers. The two arrows here show the direction of R_{tip} changing as θ_c in SJM decreases (or increases) from the equilibrium values 60° and 19° , respectively, approaching their experimental values.

taking a range of values of the base-cone angle θ_c in (3.14). Note that this remains a static analysis assessing the change of initial contact angle. With Bo , initial conditions \tilde{h}_0 and cone height z_b taken to be those of figure 13(b) for both substrates, we confirm that decreasing the contact angle from $\theta_c = 60^\circ$, and increasing it from 19° , respectively, improve the match between the R_{tip} prediction and corresponding experimental value (as indicated by the arrows). Note that it is both the R_{tip} and the breaking jet length \mathcal{L} that change as θ_c varies. Thus, we could correct the lollipop estimation with a more accurate geometry of the base cone, with a known evolution of the contact angle $\theta(t)$, for example. Such refinement incorporating a dynamic contact angle at the foot in the theoretical SJM model is left to ongoing work outside the scope of this paper.

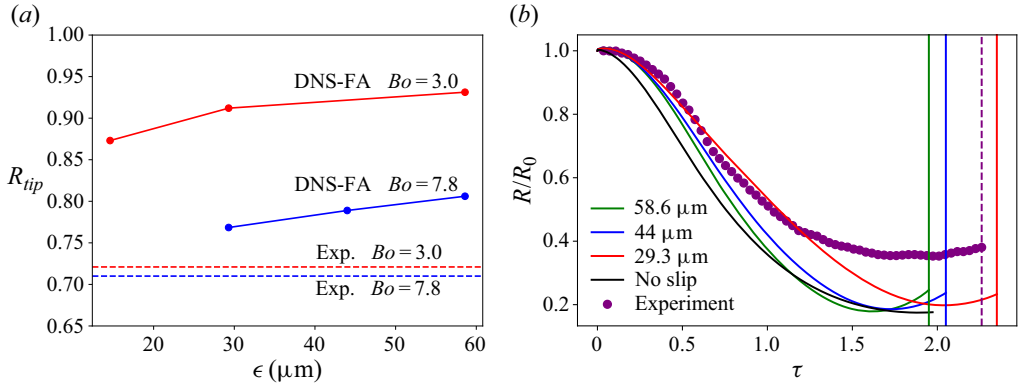


Figure 30. (a) The DNS free-angle model R_{tip} prediction as an increasing function of the implicit slip lengths, $\epsilon = \Delta/2$. We see that, as ϵ decreases, the prediction of R_{tip} is increasingly closer to experiments, for all Bond numbers, e.g. $Bo = 3, 7.8$ shown here. (b) Evolution of the wetting diameter with time. The vertical lines represent the foot pinch-off times. Free-angle simulations are seen to match the experiments better than no slip for the most part: the initial agreement is excellent with the free-angle model. Beyond $\tau = 1.2$, the wetting diameter continues to decrease in the free-angle DNS, thus injecting more volume into the ligament. Here, the experimental data correspond to a contact angle of 60° ($\theta_c = 60^\circ$). Moreover, all simulations were based on an initial spherical cap shape with that same 60° contact angle.

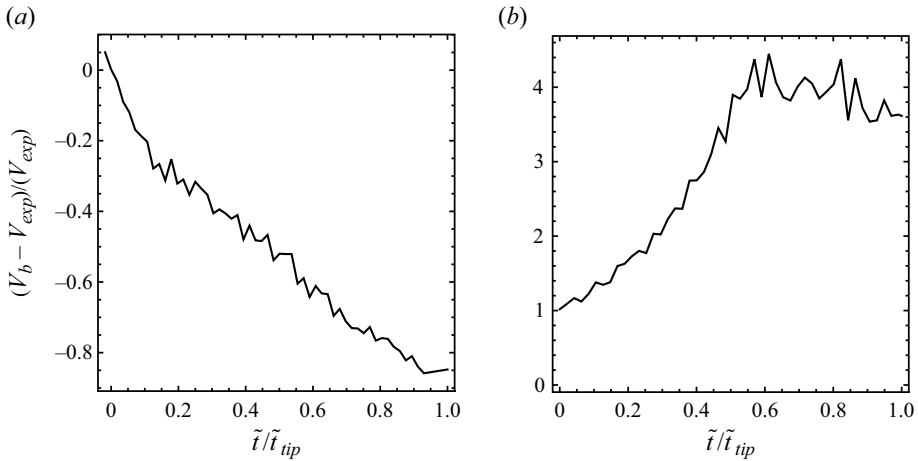


Figure 31. History of the relative volume difference between the base-cone volume $V_b = \int_0^\lambda \pi \tilde{h}_{base}^2 dz$ against its measurement, V_{exp} , during the experiment. This is obtained building on figure 29 showing the zoomed-in view of the ligament feet in the range $0 \leq z \leq z_b$ which corresponds to the experiment specified in figure 13(b), where for panel (a) here, $\theta_c = 60^\circ$. Panel (b) is analogous to the second experiment given in figure 13(b) where $\theta_c = 19^\circ$. In the first case (a), where the foot contact angle appears to be less than 60° for $\tilde{t} > 0$, V_{exp} is underestimated. Contrarily, in the second case (b), for which the angle measured is greater than 19° , V_{exp} is overestimated.

Appendix G. Direct numerical simulation model with free angle and sensitivity of pinch-off and R_{tip} predictions to contact-line slip and dynamics

We here propose a novel free-angle model that allows a time-varying microscopic contact angle determined by the flow field. In the free-angle model we calculate θ_{grid} , that is the grid-scale contact angle based on extrapolation from the flow field in the vicinity of the contact line. As our problem involves dominant inertial forces and a high

Fragmentation from inertial detachment of a sessile droplet

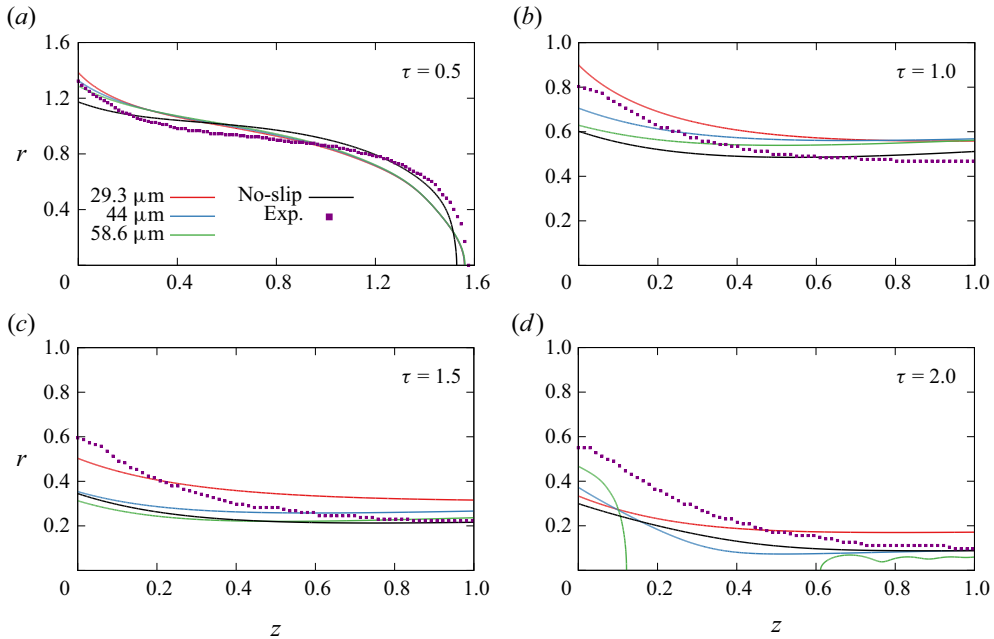


Figure 32. Interface shapes of the deformed droplet at various instants of time τ for $Bo = 7.8$. The purple squares are the experiments. The solid black line is for the no-slip boundary condition with a constant contact angle of 60° with a grid size of $14.6 \mu\text{m}$. The other lines correspond to the free-angle model the same as in [figure 30\(a\)](#). The horizontal axis is the axial axis and the vertical axis is radial. All simulations are axisymmetric and the resolution is $\epsilon/\Delta = 4$. Note that the slip length influences the movement of the contact line at the foot and, in turn, influences the liquid flow from the base cone.

contact-line capillary number, $Ca \equiv \mu u_{CL}/\sigma \sim O(1)$ with u_{CL} being the contact-line velocity, this approach is reasonable in capturing contact-angle oscillations originating from the macro-scale inertial effects, thus remaining consistent with the flow field. Further details of the extrapolated angle can be found in [Fullana \(2022\)](#). Additionally, we impose a slip boundary condition, where the fluid velocity at the fluid–solid surface boundary, $u_{f/s}$, is allowed to slip, i.e. to have a small value, with

$$u_{f/s} = \epsilon \frac{\partial u}{\partial y}, \quad (\text{G1})$$

where ϵ is the slip length. Hence, our free-angle model has two parts: (a) an extrapolated angle consistent with the flow at the grid scale and (b) a slip boundary condition. We proceed with the implicit slip of the VoF formulation, where $\epsilon \sim \Delta/2$, where Δ is the grid size, which is computationally achievable/accessible as opposed to the physical slip length, which is much smaller, below a micron, and not computationally accessible. In other words, the slip length here is a numerical quantity.

[Figure 30\(a\)](#) shows that, as we reduce the slip length, with increasing resolution of the contact-line dynamics, the ejected tip volume prediction improves with respect to experimental measurements. [Figure 30\(b\)](#) shows the relative movement of the contact line as a function of time, comparing numerical results with experimental and comparing the no-slip with the free-slip model outcomes. We find a reasonable agreement between the DNS and experiments for time values where $\tau < 1.2$, with again, the smallest free-slip parameter enabling improved capture of the contact-line dynamics early on.

Beyond $\tau < 1.2$ the plateau in R/R_0 in the experiment shows that the partial pinning of the contact line is not well captured by the DNS. Effects of contact-line hysteresis are well known to be the likely culprit (e.g. Bostwick & Steen 2015; Xia & Steen 2018).

Finally, figure 31 shows how the non-constant angle can introduce error in the measurements or estimation of the foot region volume, which can propagate to the extensional region of the ligament in the SJM model. Indeed, the free-angle model changes the contact-line motion in the early phase of rapid acceleration. As the contact line recedes, the contact angle decreases from its initial value of 60° and its initial wetting diameter (figure 32).

REFERENCES

- AFKHAM, S., ZALESKI, S. & BUSSMANN, M. 2009 A mesh-dependent model for applying dynamic contact angles to VOF simulations. *J. Comput. Phys.* **228** (15), 5370–5389.
- AMBRAVANESWARAN, B., WILKES, E.D. & BASARAN, O.A. 2002 Drop formation from a capillary tube: comparison of one-dimensional and two-dimensional analyses and occurrence of satellite drops. *Phys. Fluids* **14** (8), 2606–2621.
- ARRUFAT, T., CRIALESI-ESPOSITO, M., FUSTER, D., LING, Y., MALAN, L., PAL, S., SCARDOVELLI, R., TRYGGVASON, G. & ZALESKI, S. 2021 A mass-momentum consistent, volume-of-fluid method for incompressible flow on staggered grids. *Comput. Fluids* **215**, 104785.
- BOSTWICK, J.B. & STEEN, P.H. 2015 Stability of constrained capillary surfaces. *Annu. Rev. Fluid Mech.* **47** (1), 539–568.
- BOUCHER, E.A., EVANS, M.J.B. & KENT, H.J. 1976 Capillary phenomena. II. Equilibrium and stability of rotationally symmetric fluid bodies. *Proc. R. Soc. A* **349** (1656), 81–100.
- BOUCHER, E.A. & KENT, H.J. 1978 Capillary phenomena VII. Equilibrium and stability of pendent drops. *J. Colloid Interface Sci.* **67** (1), 10–15.
- BOUROUBA, L. 2021a The fluid dynamics of disease transmission. *Annu. Rev. Fluid Mech.* **53**, 473–508.
- BOUROUBA, L. 2021b Fluid dynamics of respiratory infectious diseases. *Annu. Rev. Biomed. Engng* **23** (1), 547–577.
- BRENNER, M.P., EGGERS, J., JOSEPH, K., NAGEL, S.R. & SHI, X.D. 1997 Breakdown of scaling in droplet fission at high Reynolds number. *Phys. Fluids* **9** (6), 1573–1590.
- CASTREJÓN-PITA, A.A., CASTREJÓN-PITA, J.R. & HUTCHINGS, I.M. 2012 Breakup of liquid filaments. *Phys. Rev. Lett.* **108** (7), 074506.
- CONTÒ, F.P., MARÍN, J.F., ANTKOWIAK, A., CASTREJÓN-PITA, J.R. & GORDILLO, L. 2019 Shape of a recoiling liquid filament. *Sci. Rep.* **9** (1), 1–8.
- DAY, R.F., HINCH, E.J. & LISTER, J.R. 1998 Self-similar capillary pinchoff of an inviscid fluid. *Phys. Rev. Lett.* **80** (4), 704.
- DERBY, B. 2010 Inkjet printing of functional and structural materials: fluid property requirements, feature stability, and resolution. *Annu. Rev. Mater. Res.* **40** (1), 395–414.
- DUSSAN V., E.B. & DAVIS, S.H. 1974 On the motion of a fluid–fluid interface along a solid surface. *J. Fluid Mech.* **65** (1), 71–95.
- EGGERS, J. 1993 Universal pinching of 3D axisymmetric free-surface flow. *Phys. Rev. Lett.* **71** (21), 3458–3460.
- EGGERS, J. 1995 Theory of drop formation. *Phys. Fluids* **7** (5), 941–953.
- EGGERS, J. & DUPONT, T.F. 1994 Drop formation in a one-dimensional approximation of the Navier–Stokes equation. *J. Fluid Mech.* **262**, 205–221.
- EGGERS, J. & VILLERMAUX, E. 2008 Physics of liquid jets. *Rep. Prog. Phys.* **71** (3), 036601.
- FAULWETTER, R.C. 1917 Dissemination of the angular leaf spot of cotton. *J. Agric. Res.* **8**, 457–475.
- FITT, B.D.L., MCCARTNEY, H.A. & WALKLATE, P.J. 1989 The role of rain in dispersal of pathogen inoculum. *Annu. Rev. Phytopathol.* **27**, 241–270.
- FRANKEL, I. & WEIHS, D. 1985 Stability of a capillary jet with linearly increasing axial velocity (with application to shaped charges). *J. Fluid Mech.* **155**, 289–307.
- FULLANA, T. 2022 Simulation and optimization of complex phenomena in multiphase flows. PhD thesis, Sorbonne University.
- GAUDET, S., MCKINLEY, G.H. & STONE, H.A. 1996 Extensional deformation of Newtonian liquid bridges. *Phys. Fluids* **8** (10), 2568–2579.

Fragmentation from inertial detachment of a sessile droplet

- GILET, T. & BOUROUIBA, L. 2014 Rain-induced ejection of pathogens from leaves: revisiting the hypothesis of splash-on-film using high-speed visualization. *Integr. Comp. Biol.* **54**, 974–984.
- GILET, T. & BOUROUIBA, L. 2015 Fluid fragmentation shapes rain-induced foliar disease transmission. *J. R. Soc. Interface* **12**, 20141092.
- GILET, T. & BOUROUIBA, L. 2017 La physique de la pluie conditionne la propagation des maladies en agriculture. *Reflète Phys.* **54**, 4–9.
- GOPINATHAN, J. & NOH, I. 2018 Recent trends in bioinks for 3D printing. *Biomater. Res.* **22**, 1–15.
- GREGORY, P.H. 1973 *Microbiology of the Atmosphere*. Leonhard Hill.
- GREGORY, P.H., GUTHRIE, E.J. & BUNCE, M.E. 1959 Experiments on splash dispersal of fungus spores. *Microbiology* **20**, 328–354.
- HENDERSON, D., SEGUR, H., SMOLKA, L.B. & WADATI, M. 2000 The motion of a falling liquid filament. *Phys. Fluids* **12** (3), 550–565.
- HUH, C. & SCRIVEN, L.E. 1971 Hydrodynamic model of steady movement of a solid/liquid/fluid contact line. *J. Colloid Interface Sci.* **35** (1), 85–101.
- LEJEUNE, S., GILET, T. & BOUROUIBA, L. 2018 Edge effect: liquid sheet and droplets formed by drop impact close to an edge. *Phys. Rev. Fluids* **3**, 083601.
- LEPPINEN, D. & LISTER, J.R. 2003 Capillary pinch-off in inviscid fluids. *Phys. Fluids* **15** (2), 568–578.
- LISTER, J.R. & STONE, H.A. 1998 Capillary breakup of a viscous thread surrounded by another viscous fluid. *Phys. Fluids* **10** (11), 2758–2764.
- LUBARDA, V.A. & TALKE, K.A. 2011 Analysis of the equilibrium droplet shape based on an ellipsoidal droplet model. *Langmuir* **27** (17), 10705–10713.
- MARMOTTANT, P. & VILLERMAUX, E. 2004 Fragmentation of stretched liquid ligaments. *Phys. Fluids* **16** (8), 2732–2741.
- NOTZ, P.K. & BASARAN, O.A. 2004 Dynamics and breakup of a contracting liquid filament. *J. Fluid Mech.* **512**, 223–256.
- PADDAY, J.F., PITT, A.R. & TABOR, D. 1973 The stability of axisymmetric menisci. *Phil. Trans. R. Soc. Lond. A* **275** (1253), 489–528.
- PAPAGEORGIOU, D.T. & ORELLANA, O. 1998 Study of cylindrical jet breakup using one-dimensional approximations of the Euler equations. *SIAM J. Appl. Maths* **59** (1), 286–317.
- PAUL, P.A., EL-ALLAF, S.M., LIPPS, P.E. & MADDEN, L.V. 2004 Rain splash dispersal of *Gibberella zeae* within wheat canopies in Ohio. *Phytopathology* **94**, 1342–1349.
- PEREGRINE, D.H., SHOKER, G. & SYMON, A. 1990 The bifurcation of liquid bridges. *J. Fluid Mech.* **212**, 25–39.
- PIERSON, J.L., MAGNAUDET, J., SOARES, E.J. & POPINET, S. 2020 Revisiting the Taylor–Culick approximation: retraction of an axisymmetric filament. *Phys. Rev. Fluids* **5** (7), 073602.
- PLATEAU, J.A.F. 1873 *Statique expérimentale et théorique des liquides soumis aux seules forces moléculaires*, vol. 2. Gauthier-Villars.
- POPINET, S. 2009 An accurate adaptive solver for surface-tension-driven interfacial flows. *J. Comput. Phys.* **228** (16), 5838–5866.
- POPINET, S. 2015 A quadtree-adaptive multigrid solver for the Serre–Green–Naghdi equations. *J. Comput. Phys.* **302**, 336–358.
- POPINET, S. 2018 Numerical models of surface tension. *Annu. Rev. Fluid Mech.* **50** (1), 49–75.
- POULAIN, S. & BOUROUIBA, L. 2018 Biosurfactants change the thinning of contaminated bubbles at bacteria-laden water interfaces. *Phys. Rev. Lett.* **121**, 204502.
- POULAIN, S. & BOUROUIBA, L. 2019 Disease transmission via drops and bubbles. *Phys. Today* **72**, 70–71.
- QIAN, J. & LAW, C.K. 1997 Regimes of coalescence and separation in droplet collision. *J. Fluid Mech.* **331**, 59–80.
- RAYLEIGH, LORD 1878 On the instability of jets. *Proc. Lond. Math. Soc.* **s1-10** (1), 4–13.
- SAROBOL, P., COOK, A., CLEM, P.G., KEICHER, D., HIRSCHFELD, D., HALL, A.C. & BELL, N.S. 2016 Additive manufacturing of hybrid circuits. *Annu. Rev. Mater. Res.* **46** (1), 41–62.
- SCHULKES, R.M.S.M. 1994 The evolution and bifurcation of a pendant drop. *J. Fluid Mech.* **278**, 83–100.
- SCHULKES, R.M.S.M. 1996 The contraction of liquid filaments. *J. Fluid Mech.* **309**, 277–300.
- SLOBOZHANIN, L.A. & PERALES, J.M. 1993 Stability of liquid bridges between equal disks in an axial gravity field. *Phys. Fluids A* **5** (6), 1305–1314.
- STONE, H.A. 1994 Dynamics of drop deformation and breakup in viscous fluids. *Annu. Rev. Fluid Mech.* **26** (1), 65–102.
- STONE, H.A., BENTLEY, B.J. & LEAL, L.G. 1986 An experimental study of transient effects in the breakup of viscous drops. *J. Fluid Mech.* **173**, 131–158.

- STONE, H.A. & LEAL, L.G. 1989 Relaxation and breakup of an initially extended drop in an otherwise quiescent fluid. *J. Fluid Mech.* **198**, 399–427.
- VILLERMAUX, E. 2007 Fragmentation. *Annu. Rev. Fluid Mech.* **39** (1), 419–446.
- VILLERMAUX, E. 2012 The formation of filamentary structures from molten silicates: pele’s hair, angel hair, and blown clinker. *C. R. Méc.* **340** (8), 555–564.
- VILLERMAUX, E. & BOSSA, B. 2011 Drop fragmentation on impact. *J. Fluid Mech.* **668**, 412–435.
- VINCENT, L., DUCHEMIN, L. & VILLERMAUX, E. 2014 Remnants from fast liquid withdrawal. *Phys. Fluids* **26** (3), 031701.
- WANG, Y. & BOUROUBA, L. 2018 Unsteady sheet fragmentation: droplet sizes and speeds. *J. Fluid Mech.* **848**, 946–967.
- WANG, Y. & BOUROUBA, L. 2021 Growth and breakup of ligaments in unsteady fragmentation. *J. Fluid Mech.* **910**, A39.
- WILKES, E.D., PHILLIPS, S.D. & BASARAN, O.A. 1999 Computational and experimental analysis of dynamics of drop formation. *Phys. Fluids* **11** (12), 3577–3598.
- XIA, Y. & STEEN, P.H. 2018 Moving contact-line mobility measured. *J. Fluid Mech.* **841**, 767–783.
- YARIN, A.L. 2006 Drop impact dynamics: splashing, spreading, receding, bouncing. . . . *Annu. Rev. Fluid Mech.* **38** (1), 159–192.